

THE UNIVERSITY OF CHICAGO

MEASURING THE TEMPERATURE ANISOTROPY AND GRAVITATIONAL
LENSING OF THE COSMIC MICROWAVE BACKGROUND WITH THE SOUTH
POLE TELESCOPE

A DISSERTATION SUBMITTED TO
THE FACULTY OF THE DIVISION OF THE PHYSICAL SCIENCES
IN CANDIDACY FOR THE DEGREE OF
DOCTOR OF PHILOSOPHY

DEPARTMENT OF PHYSICS

BY
KYLE TYLER STORY

CHICAGO, ILLINOIS

MARCH 2015

Copyright © 2015 by Kyle Tyler Story
All Rights Reserved

This thesis is dedicated to the strong women in my life: my grandmother Maola Blean, my mother Catherine Blean Story, and my wife Veena Krishnamoorthy. Grandma and Mom: your teaching, support, and encouragement have brought me to where I am today; I wish you were alive today to see the completion of my thesis. Veena: your love support in work and life is invaluable; you make life beautiful.

Twas built a telescope on deep south ice
that viewed the southern skies not once but twice.

First it mapped intensity;

Q and U followed quickly.

The view fit Lambda-C-D-M quite nice.

TABLE OF CONTENTS

LIST OF FIGURES	vii
LIST OF TABLES	xii
ACKNOWLEDGMENTS	xiii
ABSTRACT	xiv
1 INTRODUCTION	1
1.0.1 The Cosmic Microwave Background	1
1.0.2 Λ CDM: The Standard Model of Cosmology	4
1.0.3 CMB temperature power spectrum	5
1.0.4 Gravitational lensing of the CMB	7
1.0.5 The South Pole Telescope	8
1.0.6 SPTpol	8
2 CMB TEMPERATURE POWER SPECTRUM	11
2.1 Observations and Data Reduction	13
2.1.1 Observing Strategy and Fields	14
2.1.2 Map-making: Time Ordered Data to Maps	15
2.1.3 Beam Functions	19
2.1.4 Calibration	20
2.2 Power Spectrum	20
2.2.1 Maps	21
2.2.2 Window	21
2.2.3 Cross-Spectra	22
2.2.4 Unbiased Spectra	23
2.2.5 Simulations and the Transfer Function	24
2.2.6 Bandpower Covariance Matrix	25
2.2.7 Combining Fields	26
2.2.8 Bandpower Window Functions	27
2.3 Tests for Systematic Errors	28
2.3.1 Null Tests	28
2.3.2 Pipeline Tests	30
2.4 Bandpowers	31
2.5 Cosmological Constraints	31
2.5.1 Foreground treatment	35
2.5.2 Estimating Cosmological Parameters	36
2.5.3 Goodness of fit to the Λ CDM Model	37
2.5.4 External Datasets	37
2.5.5 SPT-only Λ CDM constraints	38
2.5.6 Combined Λ CDM constraints	41
2.5.7 Consistency of Λ CDM constraints	42

2.5.8	Physical origin of SPT constraints on Λ CDM	42
2.5.9	Dependence of SPT constraints on multipole range	45
2.5.10	Gravitational Lensing	46
2.5.11	Mean Curvature of the Observable universe	49
2.5.12	Inflation	52
2.6	Discussion	63
3	CMB GRAVITATIONAL LENSING POTENTIAL POWER SPECTRUM	67
3.1	Sptpol Observations and Data-Processing	70
3.1.1	Calibration	74
3.1.2	Noise estimation	77
3.2	CMB Lensing Analysis	78
3.2.1	Map Filtering	79
3.2.2	Quadratic Estimator of ϕ	84
3.2.3	Evaluating the ϕ -estimator	88
3.2.4	The Power Spectrum of ϕ	92
3.3	Simulations	98
3.4	Uncertainty budget	100
3.4.1	Beam and Absolute Calibration	102
3.4.2	Polarization Calibration	102
3.4.3	Temperature-to-Polarization Leakage	103
3.4.4	Electrical crosstalk between detectors	103
3.4.5	Foregrounds	103
3.4.6	Normalization Calculation	105
3.4.7	Total Uncertainty	105
3.5	Results	106
3.5.1	Lensing Potential Map	106
3.5.2	Lensing Potential Power Spectrum	106
3.6	Systematic Error Checks	114
3.7	Discussion	117
4	CONCLUSION	120
	REFERENCES	122

LIST OF FIGURES

1.1	The SPT and SPTpol survey regions are shown here, overlaid on an orthographic projection of the IRAs 100 μm dust map from [112]. The 2500 deg^2 SPT-SZ survey is outlined in yellow . The 100 deg^2 SPTpol “deep field” is outlined in red . The ongoing 500 deg^2 SPTpol “survey field” is outlined in blue . Results presented in chapter 2 use data from the SPT-SZ survey, while results presented in chapter 3 use data from the SPTpol deep field.	10
2.1	The 2500 deg^2 SPT-SZ survey. We show the full survey region with lightly filtered 95 GHz data from the SPT, using the data and filters which best capture the degree-scale anisotropy of the CMB visible in this figure. The power spectrum measurement reported in this chapter is calculated from 2540 deg^2 of sky and analyzes 150 GHz data with a different high-pass filter, as described in § 2.1.2.	13
2.2	The SPT was used to observe 2500 deg^2 over 19 individual fields, which are overlaid here on an orthographic projection of the IRAS 100 μm dust map from [112]. These observation fields were chosen to lie in regions of low dust emission (dark red).	16
2.3	Left panel: The SPT power spectrum. The leftmost peak at $\ell \sim 800$ is the third acoustic peak. Right panel: A comparison of the new SPT bandpowers with other recent measurements of the CMB damping tail from ACBAR [105], ACT [32], and SPT (K11). Note that the point source masking threshold differs between these experiments which can affect the power at the highest multipoles. In order to highlight the acoustic peak structure of the damping tail, we plot the bandpowers in the right panel as $\ell^4 C_\ell / (2\pi)$, as opposed to $D_\ell = \ell(\ell + 1) C_\ell / (2\pi)$ in the left panel. The solid line shows the theory spectrum for the ΛCDM model + foregrounds that provides the best fit to the SPT+ <i>WMAP</i> 7 data. The bandpower errors shown in these plots contain sample and noise variance terms only; they do not include beam or calibration uncertainties.	32
2.4	The SPT bandpowers (blue), <i>WMAP</i> 7 bandpowers (orange), and the lensed ΛCDM +foregrounds theory spectrum that provides the best fit to the SPT+ <i>WMAP</i> 7 data shown for the CMB-only component (dashed line), and the CMB+foregrounds spectrum (solid line). As in Figure 2.3, the bandpower errors shown in this plot do not include beam or calibration uncertainties.	33
2.5	The one-dimensional marginalized likelihoods of the six parameters of the ΛCDM model, plus two derived parameters: the dark energy density Ω_Λ and the Hubble constant H_0 . The constraints are shown for the SPT-only (blue dot-dashed lines), <i>WMAP</i> 7-only (red dashed lines), and SPT+ <i>WMAP</i> 7 (black solid lines) datasets. With the exception of τ , the SPT bandpowers constrain the parameters approximately as well as <i>WMAP</i> 7 alone. In particular, the SPT bandpowers measure the angular sound horizon θ_s extremely well because they measure seven acoustic peaks. In the SPT-only constraints, the <i>WMAP</i> 7 measurement of τ has been applied as a prior; because of this we do not plot an SPT-only line on the τ plot.	39

- 2.6 Same Λ CDM-model parameters as Figure 2.5, except showing the effect of including the SPT bandpowers over sub-sets of the ℓ -range. The constraints for *WMAP7*-only are shown (**red dashed lines**). Using the SPT+*WMAP7* dataset, the constraints are shown from the full ℓ -range of SPT data (**black solid lines**), from the high- ℓ range $1500 < \ell_{SPT} < 3000$ (**purple dot-dot-dashed lines**), and from the low- ℓ range $650 < \ell_{SPT} < 1500$ (**green dot-dashed lines**). . . . 46
- 2.7 The SPT bandpowers allow a significant detection of gravitational lensing through the effective smoothing of the acoustic peaks. Here, we show the one-dimensional likelihood function for A_L , a rescaling parameter for the gravitational lensing potential power spectrum ($C_\ell^{\phi\phi} \rightarrow A_L C_\ell^{\phi\phi}$). The SPT+*WMAP7* data lead to a 8.1σ detection of CMB lensing (this was the most significant detection at the time of publication in [129]). 47
- 2.8 The low-redshift information imprinted on the CMB by gravitational lensing, along with the other information in the CMB anisotropy power spectrum, enables the placement of tight constraints on the mean curvature of the observable Universe. The addition of low-redshift probes further tighten CMB-only constraints on the mean curvature. **Left panel:** The one-dimensional marginalized constraints on Ω_k from SPT+*WMAP7* (**black solid line**), SPT+*WMAP7*+ H_0 (**orange dashed line**), SPT+*WMAP7*+BAO (**black dotted line**), and SPT+*WMAP7*+BAO+ H_0 (**blue dot-dashed line**). The SPT+*WMAP7* datasets measure the mean curvature of the observable universe to a precision of $\sim 1.5\%$, while combining SPT, *WMAP7*, and either H_0 or BAO data reduces the uncertainty by a factor of ~ 3 . **Right panel:** The two-dimensional constraints on Ω_M and Ω_Λ from the SPT+*WMAP7* data alone. The SPT+*WMAP7* data rule out $\Omega_\Lambda = 0$ at 5.4σ 50
- 2.9 The data strongly prefer departures from a scale invariant primordial power spectrum ($n_s < 1$), as predicted by inflation. **Left panel:** The marginalized one-dimensional constraints on n_s for the standard Λ CDM model (with $r = 0$) using several datasets. SPT data tightens the constraint on n_s relative to *WMAP7* alone. Adding BAO data further tightens this constraint and leads to a preference for lower values of n_s , while adding H_0 has little effect. **Right panel:** The one-dimensional marginalized constraints on n_s from the SPT+*WMAP7*+ H_0 +BAO dataset given three different models. Plotted are Λ CDM (**black solid line**), Λ CDM + Σm_ν (**purple dashed line**) as a typical case for extensions affecting the late-time universe, and Λ CDM + N_{eff} (**green dot-dashed line**) as a typical case for extensions affecting the Silk damping scale. Of the extensions considered here, only those that affect the damping tail – in this case by varying neutrino species – causes noticeable movement towards $n_s = 1$. We note that in all cases the data robustly prefer a scale-dependent spectrum with $n_s < 1$ 54

- 2.10 This figure highlights the contributions of the SPT data to constraints on the tensor-to-scalar ratio, r . We show four datasets: *WMAP7* (**red dashed line**), *WMAP7*+BAO (**orange dot-dashed line**), SPT+*WMAP7* (**black solid line**), and SPT+*WMAP7*+BAO (**black dotted line**). Note that the *WMAP7*+BAO and SPT+*WMAP7* likelihood functions are nearly identical. SPT data tightens the r constraint significantly, regardless of whether BAO data are included. While adding low-redshift H_0 measurements has minimal effect on the constraints on r (not shown), adding low-redshift information from BAO tightens constraints on r considerably. SPT+*WMAP7* constrains $r < 0.18$ (95% C.L.), while adding low-redshift BAO measurements tightens the constraint to $r < 0.11$ (95% C.L.). 57
- 2.11 We compare the constraints on the Λ CDM+ r model with predictions from models of inflation in the $n_s - r$ plane. We show the two-dimensional constraints on r and n_s as colored contours at the 68% and 95% confidence levels for three datasets: *WMAP7* (**grey contours**), CMB (**red contours**), and CMB+ H_0 +BAO (**blue contours**). Adding the SPT bandpowers partially breaks the degeneracy between n_s and r in the *WMAP7* constraint, which can be seen clearly moving between the grey and red contours. Plotted over the constraint contours are predictions for several models of inflation. We restrict our comparison with model predictions to the simplest cases of slow-roll inflation due to a single scalar field as reviewed in [8].

Solid black line: The predictions of exponential inflation ($V(\phi) \propto \exp \left[\sqrt{16\pi\phi^2/(p M_{\text{Pl}}^2)} \right]$) lie on this line. In exponential inflation, increasing p moves the prediction towards the Harrison-Zel'dovich-Peebles point $n_s = 1$, $r = 0$.

Black lines with colored circles: The predictions of power-law potential inflation models ($V(\phi) \propto (\phi/\mu)^p$, $p > 0$) for five different values of p lie on the corresponding line. The predictions in the $r - n_s$ plane are a function of N , where N is expected to be in the range $N \in [50, 60]$.

Purple region: This region represents the upper limit on r from large-field hill-top inflation models. The width of the curve represents the uncertainty due to varying $N \in [50, 60]$, but does not take into account effects of higher order terms in the potential which may become important at the end of inflation. . . 60

3.1	Noise-bias levels for this ϕ reconstruction. The theoretical Λ CDM lensing potential power spectrum is shown in black , and the individual bias terms defined in Equation 3.69 are shown individually. The realization-dependent N0 (RDN0) term (dashed orange line) is used to correct the data for the Gaussian noise bias (see Equation 3.71). The N1 bias (dashed purple line) arises from connected contributions to the CMB trispectrum (see Equation 3.72). The sum of these two terms is the total bias (solid green line) that we subtract. The residual Monte-Carlo (MC) bias term (dashed cyan line) from Equation 3.69 is calculated as the difference between the mean of de-biased lensed simulation spectra and the input spectrum to the simulations. The total bias shows the reconstruction-noise power in the reconstructed ϕ maps; thus this reconstruction measures ϕ modes with a signal-to-noise ratio greater than 1 (alternatively, the measurement is ϕ -sample-variance limited) for $100 < L \lesssim 250$	96
3.2	Lensing κ maps reconstructed from the SPTpol 100 deg ² deep-field data, smoothed with a 1-degree Gaussian beam. The colorbar on the far right shows the color scale, which has been fixed for all κ maps in Figures 3.2 and 3.3. Left: The κ -map for our MV lensing estimator, which combines all temperature and polarization information. Right: Individual κ estimates from the TT, EB, TE, and EE estimators, with the same color scale.	100
3.3	Example simulated κ -maps, plotted with the same color scale as Figure 3.2. Left: a simulated input κ -map. Middle: the reconstructed κ -map estimated from a noisy simulation that has been lensed using the potential shown in the left panel. Right: the reconstructed κ -map estimated from an unlensed simulation. Comparing the reconstructed lensed κ -map to the input map gives a visual sense of the fidelity of this reconstruction, and comparing to the unlensed κ -map gives a sense of the signal-to-noise in the MV κ -map.	101
3.4	The $\hat{C}_{L_b}^{\phi\phi}$ power spectra for all estimators we consider in this chapter. “MV \times MV” is the spectrum from the minimum-variance estimator. The amplitudes of each spectrum relative to the fiducial PLANCK+LENS+WP+HIGHL model are calculated with Equation 3.77 and shown in each panel.	107
3.5	Lensing potential power spectrum bandpowers estimated from SPTpol. The MV and POL spectra are shown with red circles and black squares, respectively. The black solid line shows the PLANCK+LENS+WP+HIGHL best-fit Λ CDM model. Note the POL points have been shifted by 1/4 of a bin in L for plotting purposes.	108
3.6	Lensing potential power spectrum bandpowers estimated from SPTpol, as well as those previously reported for temperature by SPT-SZ [131], ACT [30], <i>Planck</i> [101], and for polarization by POLARBEAR ([104]). The black solid line shows the PLANCK+LENS+WP+HIGHL best-fit Λ CDM model.	109

3.7	The distribution of reconstructed MV lensing amplitudes from simulations are shown here for lensed (green) and unlensed (red) simulations. The amplitude of the MV estimate for the data is shown as a blue line. The statistical uncertainty of the MV lensing construction is given by the standard deviation of the lensed simulations ($\Delta A_{\text{MV}} = 0.14$). The significance with which we rule out the no-lensing hypothesis is calculated from the standard deviation of the unlensed simulations (0.065).	111
3.8	Power spectrum consistency tests. The upper panel shows the spectrum of each consistency test. The lower panels show the same set of consistency tests, plotted as the difference between each consistency test relative to the fiducial spectrum, divided by the 1σ statistical error bar of the MV spectrum. Note that the statistical uncertainty on these difference-spectra will be a function of the analysis and not necessarily the same as for the baseline MV spectrum. The grey band in each of the lower panels shows the 1σ statistical uncertainty region. The error bars shown in the lower panels are calculated from the variance in simulations of each consistency test.	113

LIST OF TABLES

2.1	SPT Fields	17
2.2	The locations and sizes of the fields observed by the SPT between 2008 and 2011. For each field we give the center of the field in Right Ascension (R.A.) and declination (decl.), the nominal extent of the field in Right Ascension and declination, and the effective field area as defined by the window (see Section 2.2.2).	17
2.3	SPT Bandpowers and Bandpower Errors	34
2.4	The ℓ -band range, weighted multipole value ℓ_{eff} , bandpower D_ℓ , and associated bandpower uncertainty σ of the SPT power spectrum. The errors are the square-root of the diagonal elements of the covariance matrix, and do not include beam or calibration uncertainties.	34
2.5	Λ CDM Parameter Constraints from the CMB and external datasets	40
2.6	Constraints on n_s and r from CMB and external datasets	52
3.1	Terms in the evaluation of $\bar{\phi}^{TT}$	91
3.2	Systematic Uncertainties	101
3.3	The contributions to the systematic uncertainty budget. The quadrature sum of the systematic uncertainty terms gives the total systematic uncertainty, ΔA_{tot} .	101
3.4	MV lensing bandpowers	112
3.5	The bandpowers for the MV spectrum are presented here as defined in Equation 3.79 and shown in Figures 3.5 and 3.6. Bins are evenly spaced in $\log(L)$, and bandpowers are reported at the center of each bin.	112
3.6	MV Systematic Error and Null tests	112
3.7	Results of systematics tests. For each test, the χ^2 and PTE of the $C_L^{\phi\phi}$ spectrum are shown in the second column. The change in amplitude and associated PTE are shown in the third column. See Equation 3.80 for more detail. The $l_{\text{xmin}} = 400$ test fails, which is why we place the cut higher, at $l_{\text{xmin}} = 450$ in the analysis. .	112

ACKNOWLEDGMENTS

I owe a debt of gratitude to the many people who have supported me in the pursuit of my physics research. After I discovered the excitement of physics in high school, Hugo Schmidt took me into his lab at Montana State University and gave me a first taste of physics research, guiding me through a project to design and build a small oven for materials experiments.

As an undergraduate, I typed my first tentative key-strokes into a Linux terminal under the guidance of James Cordes, where we studied the variable timing of pulsars. During two summer breaks, I had a wonderful experience working with Francois Menard in Grenoble, France. We studied proto-planetary accretion disks during the week, and I roamed the Alps on the weekends. Jim Alexander at Cornell University was an important professional role model, teaching me about particle physics, programming, and most importantly, to approach physics with curiosity and joy. Tom Caswell has been my study partner and close friend since we met in our first physics class at Cornell over a dozen years ago.

It has been wonderful working with the South Pole Telescope team at the University of Chicago and collaborating institutions. Early on, my adviser John Carlstrom proffered some sage advice; “focus on the research you find interesting. You will work harder, be more successful, and enjoy yourself in the process.” Thank you John for your steady support and for giving me the freedom to follow that advice. At Chicago, I have benefited from excellent professional mentorship, in particular from Steve Meyer, Brad Benson, and Tom Crawford. Thank you to those who directly advised my projects: Christian Reichardt, Ryan Keisler, Lloyd Knox, Duncan Hanson, and Gil Holder. It has been a pleasure working with the other graduate students in LASR and the SPT group; in particular, thanks to Tyler Natoli, who has worked closely with me since we started graduate school together.

Finally, my family has been supportive beyond words: my father Mark, mother Catherine, brother Brian, uncle Bob, wife Veena, and many others. I would not be here today without all of you.

ABSTRACT

Over the past two decades, measurements of the cosmic microwave background (CMB) have provided profound insight into the nature of the universe. Detailed information about the composition and evolution of the universe is encoded in the temperature and polarization anisotropy of the CMB, the measurements of which have enabled powerful tests of cosmological theory. In this thesis we present two studies of the CMB using data from the South Pole Telescope (SPT).

We first present a measurement of the temperature power spectrum of CMB from the 2500 deg² SPT-SZ survey using data from the first camera mounted on the SPT. This measurement and the cosmological interpretation was published in a pair of papers [128, 57]. Relative to all previous experiments at the time of publication, this analysis improved the precision of the power spectrum measurement over the entire range of angular multipoles reported ($650 < \ell < 3000$). In combination with large angular scale measurements from *WMAP7*, these data provided several important constraints: the most significant detection of gravitational lensing of the CMB at the time (8.1σ), the first $> 5\sigma$ detection of dark energy from CMB data alone, the first $> 5\sigma$ detection of a scalar spectra index below unity (in combination with external data sets), the tightest constraints on tensor modes at the time ($r < 0.11$ at 95% C.L., in combination with external data sets), and interesting constraints on neutrino physics and other extensions to the Λ CDM cosmological model.

Second, we measure the CMB gravitational lensing potential and its power spectrum using data from the polarization-sensitive camera SPTpol, the second camera installed on SPT. We use a quadratic estimator technique, which takes advantage of the statistical anisotropy induced by lensing in the CMB temperature and polarization fields to reconstruct the lensing potential. We measure the power spectrum of the lensing potential, and find that it is well fit by a fiducial Λ CDM model. This measurement rejects the no-lensing hypothesis at 14σ . Restricting ourselves to polarization data only, we reject the no-lensing hypothesis at 5.9σ . This is the highest signal-to-noise map of the CMB lensing potential to date. The quadratic

estimator analysis developed here sets the path for future analyses from SPTpol and the third generation experiment SPT-3G.

CHAPTER 1

INTRODUCTION

The cosmic microwave background (CMB) has proven to be an invaluable source of information about the nature of the universe. The temperature and polarization anisotropies of the CMB contain a wealth of information about the composition and evolution of the universe. Additionally, gravitational interactions with large-scale structure imprint subtle signatures on the CMB, providing insight into the growth of structure at late times. In this thesis, we describe two measurements using CMB data collected with the South Pole Telescope (SPT). In chapter 2, we describe a measurement of the CMB temperature anisotropy power spectrum which was published in [129]. In chapter 3, we describe a measurement of the CMB lensing potential power spectrum using both temperature and polarization information which has been submitted for publication [128].

1.0.1 The Cosmic Microwave Background

In the standard model of cosmology, the infant universe underwent a short period of exponential expansion during its first moments, a period known as cosmic inflation¹ (for a review, see [8]). In the simplest models of inflation, this expansion is driven by the potential energy of a scalar field (the inflaton) with a symmetric potential. The potential energy of the inflaton field evolves with time, and inflation ends when the inflaton reaches the minimum of its potential; at this time the inflaton field decays, populating the universe with the particles and fields observed today. Quantum-mechanical fluctuations in the inflaton potential produce a nearly scale-invariant Gaussian spectrum of curvature fluctuations in the gravitational potential of the infant universe. These initial fluctuations seed initial perturbations in the density field, evolving and growing into the structure observed in the universe today.

1. We do not know how the universe started. Here, we wrap this lack of understanding in the misleading term “the big bang,” which delineates the transition between the unknown initial conditions and the subsequent development of the universe under laws of physics which have been studied and understood.

The evolution of these density fluctuations depends sensitively on the expansion history of the universe. This expansion history is described by a scale factor $a(t)$ which is set to unity today and related to redshift by $a(t) = 1/[1 + z(t)]$ and by the present-day expansion rate, the Hubble constant, which is parametrized by the dimensionless parameter h such that $H_0 \equiv 100h \text{ km sec}^{-1} \text{ Mpc}^{-1}$. Radiation initially dominated the energy density of the universe, however, the energy density of radiation ρ_γ decreases as a^{-4} (ρ_γ decreases as the volume plus an additional factor of a^{-1} due to a cosmological redshift) while the energy density of matter ρ_m is proportional to a^{-3} and the energy density of dark energy ρ_Λ is proportional to a^0 (under the assumption that dark energy is a cosmological constant, an assumption that is consistent with constraints from current data). Thus the dominant energy component in the universe evolves, beginning with a radiation-dominated era, transitioning to a matter-dominated era shortly before the CMB is formed, and entering a dark energy-dominated era in the late-time universe.

The initial curvature fluctuations from inflation produce a pattern of density fluctuations with over and under-dense regions. The universe at this time is filled with a photon-baryon plasma that is coupled to the density fluctuations; the pull of gravity into over dense regions and the push of photon-pressure creates sound waves, or “baryon-acoustic oscillations” in the photon-baryon plasma. This oscillating plasma cools with cosmic expansion, and approximately 400,000 years after inflation, photons no longer have enough energy to ionize hydrogen; at this “epoch of recombination” the radiation and matter fields decouple, allowing photons to stream unimpeded through the universe. From Earth we see CMB photons which scattered off electrons in a photosphere called the “last scattering surface,” a spherical shell centered on Earth with a radius equal to the distance light has traveled since the epoch of recombination.

The CMB observed today forms a nearly isotropic background with a spectrum of a near-perfect blackbody. On top of the monopole, however, the anisotropies in the matter density at the last-scattering surface imprint anisotropies in the temperature and polarization of

the CMB. The CMB anisotropies are typically described as spatial variations in the black-body temperature of the CMB, $\Delta T(\hat{n})$, where \hat{n} denotes the line-of-sight direction². The baryon-acoustic oscillations appear as a nearly-harmonic series of peaks in the anisotropy power spectrum which corresponds to the scale of the sound waves in the primordial plasma at recombination. The peak structure arises from density modes that have reached extrema in their oscillations (maximal compression or rarefaction into potential wells) at the epoch of recombination. CMB anisotropies at fine angular scales are exponentially suppressed by photon diffusion during recombination (“Silk damping”, [120]).

The CMB is also partially polarized. CMB polarization is primarily sourced by Thompson scattering off of electrons in the presence of a local quadrupole; the light scattered from an electron is polarized along the cold axis of the electron’s local quadrupole. Quadrupoles at recombination are generated from gradients in the fluid velocity and gravitational redshifts associated with gravitational waves, leading to a net linear polarization of the CMB. The CMB polarization field is commonly decomposed into even-parity “*E*-mode” and odd-parity “*B*-mode” components [e.g., 62]. Gradients in the fluid velocity generate pure *E*-modes, while gravitational waves generate both *E* and *B*-modes [114, 66].

As CMB photons travel through the universe, they interact with intervening matter in processes which imprint “secondary” anisotropies on the CMB. One important type of interaction is gravitational lensing, the process in which the travel paths of CMB photons are deflected by gravitational interactions with large-scale structure. CMB lensing will be discussed at length in sections 1.0.4, 2.5.10, and chapter 3. CMB photons can also be re-scattered by hot intra-cluster gas resulting in the thermal and kinetic Sunyaev-Zel’dovich (SZ) effect. Additionally, the first stars turn on and reionize the universe during the “epoch of reionization.” A fraction of CMB photons will be re-scattered by ionized gas after this epoch.

2. Throughout this work, the unit K refers to equivalent fluctuations in the CMB temperature, i.e., the temperature fluctuation of a 2.73 K blackbody that would be required to produce the same power fluctuation. The conversion factor is given by the derivative of the blackbody spectrum $\frac{dB_\nu}{dT}$, evaluated at 2.73 K.

Information about all of these processes can be obtained by measuring the temperature and polarization anisotropies of the CMB.

1.0.2 Λ CDM: The Standard Model of Cosmology

This picture of the universe is well described by the “Lambda Cold Dark Matter” (Λ CDM) model which has become the standard model of cosmology. This model encapsulates an incredible breadth of physics into a highly predictive framework and has been extremely successful at matching observations from the CMB and other cosmological probes. We parametrize the Λ CDM model with six parameters: the baryon density $\Omega_b h^2$, the density of cold dark matter $\Omega_c h^2$, the amplitude of the primordial scalar fluctuations Δ_R^2 , the spectral index of the scalar fluctuations n_s , the angular scale of the sound horizon at last scattering θ_s , and the optical depth to reionization τ . The present-day energy density is comprised of three components: Ω_b , Ω_c , and the dark energy density Ω_Λ (the energy density of radiation today is negligibly small). We express the energy densities as $\Omega_i h^2$ since these quantities are proportional to the physical density of the species today. The Λ CDM model assumes the universe is flat such that $\Omega_b + \Omega_c + \Omega_\Lambda = 1$. The spectrum of primordial scalar perturbations at the end of inflation is modeled as a simple power law in wavenumber k ,

$$\Delta_R^2(k) = \Delta_R^2(k_0) \left(\frac{k}{k_0} \right)^{n_s-1}, \quad (1.1)$$

where the amplitude $\Delta_R^2(k_0)$ is specified at a pivot scale $k = k_0$. The scalar spectral index n_s governs how this spectrum depends on scale, with $n_s = 1$ corresponding to a scale-invariant spectrum. The sound horizon is the distance sound waves have travelled through the primordial plasma by the epoch of recombination. The sound horizon subtends an angle on the sky denoted as θ_s . Finally, the universe becomes partially opaque after reionization. The extinction of CMB photons after reionization is parametrized by the optical depth τ .

1.0.3 CMB temperature power spectrum

Measurements of the power spectrum of CMB anisotropies provide extremely powerful constraints on models of cosmology. The relationship between the shape of the CMB power spectrum and the parameters of the Λ CDM model has been studied in great detail; for a review see [59] or [60]. Here we give a brief and intuitive description of how the Λ CDM parameters are constrained by the CMB temperature power spectrum. We describe the physical origin of the parameter constraints from SPT measurements in particular in section 2.5.8.

The CMB power spectrum is measured as a function of angular multipoles ℓ where smaller angular scales correspond to larger values of ℓ . Primary CMB anisotropies imprinted at the last scattering surface dominate the power spectrum on large-scales, to roughly $\ell \sim 3000$ in temperature, while secondary anisotropies from subsequent interactions dominate at smaller scales, though they have important effects over all scales. The baryon acoustic oscillations described in section 1.0.1 create a harmonic series of peaks in the power spectrum, which are clearly visible in figure 2.4. Photon diffusion exponentially suppresses power at larger ℓ , creating the “damping tail” between $1000 \lesssim \ell \lesssim 3000$.

The initial scalar density perturbations are described by a power law in k , as in equation 1.1. The amplitude $\Delta_R^2(k_0)$ sets the total scale of the density perturbations, and thus the overall amplitude of the CMB power spectrum. The scalar spectral index n_s is determined from the slope of the power spectrum. Smaller values of n_s correspond to a steeper initial spectrum with less power at high- ℓ in the CMB power spectrum.

The angular scale of the sound horizon at last scattering θ_s is determined by the location of the acoustic peaks³. The CMB provides information about angular scales. CMB measurements constrain the angular size of the sound horizon θ_s extremely precisely: $\Delta\theta_s/\theta_s = 9.6 \times 10^{-4}$, see CMB column of table 2.5. The angular scale θ_s can be related to a physical

3. Note, the location of the first peak does not correspond exactly to the size of the sound horizon, primarily due to the decay of the gravitational potential after recombination (the integrated Sachs-Wolfe effect, [61]).

scale only if the distance to the last scattering surface is determined.

The scale of photon diffusion is determined by the slope of the damping tail of the CMB. The angular scale of the sound horizon θ_s and the diffusion scale θ_d depend differently on the expansion rate of the universe at the epoch of recombination; because both of these scales are measured in the power spectrum, the power spectrum is sensitive to the expansion rate at the epoch of recombination.

The total matter density is determined largely from differences in the acoustic oscillations during the radiation-dominated and matter-dominated eras. Gravitational potential modes smaller than the horizon decay during the radiation-dominated era, and stay roughly constant after the transition to matter domination at $z_{\text{eq}} \sim 3000$ (see table 2.5). The difference in oscillation amplitudes allows us to separate oscillation modes which entered the horizon during radiation domination from those that entered during matter domination. Modes with $\ell \gtrsim 430$ entered the horizon during the radiation-dominated era, while larger scales entered during matter domination [57]. The radiation density is completely specified in Λ CDM by the temperature of the CMB, thus if we know z_{eq} , we know the total matter density.

The baryon density is determined by the relative heights of the even and odd-numbered acoustic peaks. Gravity compresses matter into potential wells (odd peaks), while radiation pressure pushes out into potential hills (even peaks). Thus increasing the baryon density increases the amplitudes of the odd peaks. The dark matter density is the component of the total matter density which is not comprised of baryons.

Finally, the re-scattering of CMB phonons by free electrons after reionization uniformly suppresses the CMB temperature anisotropy by a factor of $e^{-\tau}$; this effect is almost completely degenerate with $\Delta_R^2(k_0)$ in the temperature power spectrum. This scattering process introduces polarization due to quadrupolar anisotropies, and the CMB polarization signal peaks at scales larger than the horizon at the epoch of reionization. As a result, the power at large angular scales in the even-parity E -mode CMB power spectrum increases as τ increases. Consequently, the best constraints on τ come from large-scale E -mode measurements (e.g.,

those made by *WMAP7* and *Planck*).

1.0.4 Gravitational lensing of the CMB

As CMB photons travel through the universe, their travel paths are bent by gravitational interactions with large-scale structure in a process known as gravitational lensing. Lensing distorts the CMB anisotropies; this smooths the acoustic peaks in the temperature and *E*-mode power spectra and converts some *E*-mode power into odd-parity *B*-mode power at scales of $\ell \gtrsim 100$. Gravitational lensing additionally couples harmonic modes which were originally independent; this produces a non-Gaussian signal that can be used to reconstruct the CMB lensing potential. The effects of gravitational lensing on the CMB are described in more detail in chapter 3 and the references therein.

Gravitational lensing probes large-scale structure over a wide range of redshifts typically in the range $0.1 < z < 5$ [81]. The amplitude and shape of the lensing potential are sensitive to a combination of the amount of matter in the universe and the growth rate of structure (for a concise description, see Appendix E of [98]). This information is highly complementary to that of the CMB power spectrum described above. In combination with CMB power spectrum measurements, CMB lensing adds a second measurement of both the total matter density as well as the expansion rate (via the growth rate) at these typical redshifts. Gravitational lensing measurements including CMB polarization information promise to provide powerful observational constraints in the near future [34, 9].

In this thesis we present two measurements of gravitational lensing. We significantly detect gravitational lensing in the CMB temperature power spectrum in section 2.5.10. In chapter 3, we present a measurement of the CMB lensing potential and its power spectrum which was published in [128].

1.0.5 The South Pole Telescope

The SPT is a 10-meter diameter telescope located at the Amundsen-Scott South Pole station in Antarctica [22]. The SPT has an off-axis Gregorian design with a one-square-degree field of view and arcminute resolution [93]. With this resolution, the SPT can be used to measure the millimeter-wave sky from degree to arcminute scales.

The first receiver used with the SPT was the “SPT-SZ” camera which was installed in 2007. The SPT-SZ camera is comprised of ~ 960 transition-edge sensor (TES) bolometers, each of which are sensitive to one of three observing bands at approximately 90, 150, and 220 GHz. The receiver focal plane is read out using analog frequency multiplexed Superconducting QUantum Interference Devices (SQUID’s) amplifiers [36].

Between March 2008 and November 2011, the SPT was used to survey a $\sim 2500 \text{ deg}^2$ region of sky between declinations of -40° and -65° and right ascensions of 20h and 7h; these observations are referred to as the “SPT-SZ” survey. The survey footprint is shown in figure 1.1. In chapter 2 we present the CMB power spectrum measured from the 150 GHz data taken during this survey, which was published in [128]. The SPT has also been used to study a host of scientific topics including but not limited to primary [69] and secondary CMB anisotropies [86, 119, 48], galaxy clusters with the Sunyaev-Zel’dovich (SZ) effect (e.g., [124, 133, 137, 126, 14]), and synchrotron and radio galaxies [134, 88].

1.0.6 SPTpol

The second camera used with the SPT is SPTpol, a polarization-sensitive receiver installed in early 2012. SPTpol was built to study the polarization of the CMB, which contains additional information beyond the CMB temperature anisotropies. The SPTpol receiver consists of 1536 polarization-sensitive bolometers with 1176 detectors sensitive to 150 GHz and 360 detectors sensitive to 95 GHz. These detectors are read out with digital frequency multiplexed SQUID’s, allowing up to 12 detectors to be read out with a single wire. The signal is then demodulated in warm readout electronics [33]. The instrument design, characterization,

and operation are described in [47, 6, 127].

From the beginning of 2012 until the end of April 2013, SPTpol was used to observe the 100 deg^2 “SPTpol deep field,” a roughly-square patch of sky spanning right ascensions of 23h to 24h and declinations of -50 to -60 degrees. The SPTpol is currently starting the third year of observations over the $\sim 500 \text{ deg}^2$ “SPTpol survey field,” which covers the sky patch between right ascensions of 22h to 2h and declinations of -50 to -65 degrees. These fields are shown relative to the SPT-SZ 2500 deg^2 survey in figure 1.1.

In chapter 3, we present a measurement of the gravitational lensing potential using temperature and polarization data from the SPTpol deep field. SPTpol has also been used to make the first detection of B -mode power in the CMB [52], the most precise measurement of the high- ℓ E -mode power spectrum and temperature- E -mode cross-spectrum to date [29], and a measurement of the B -mode power spectrum [68].

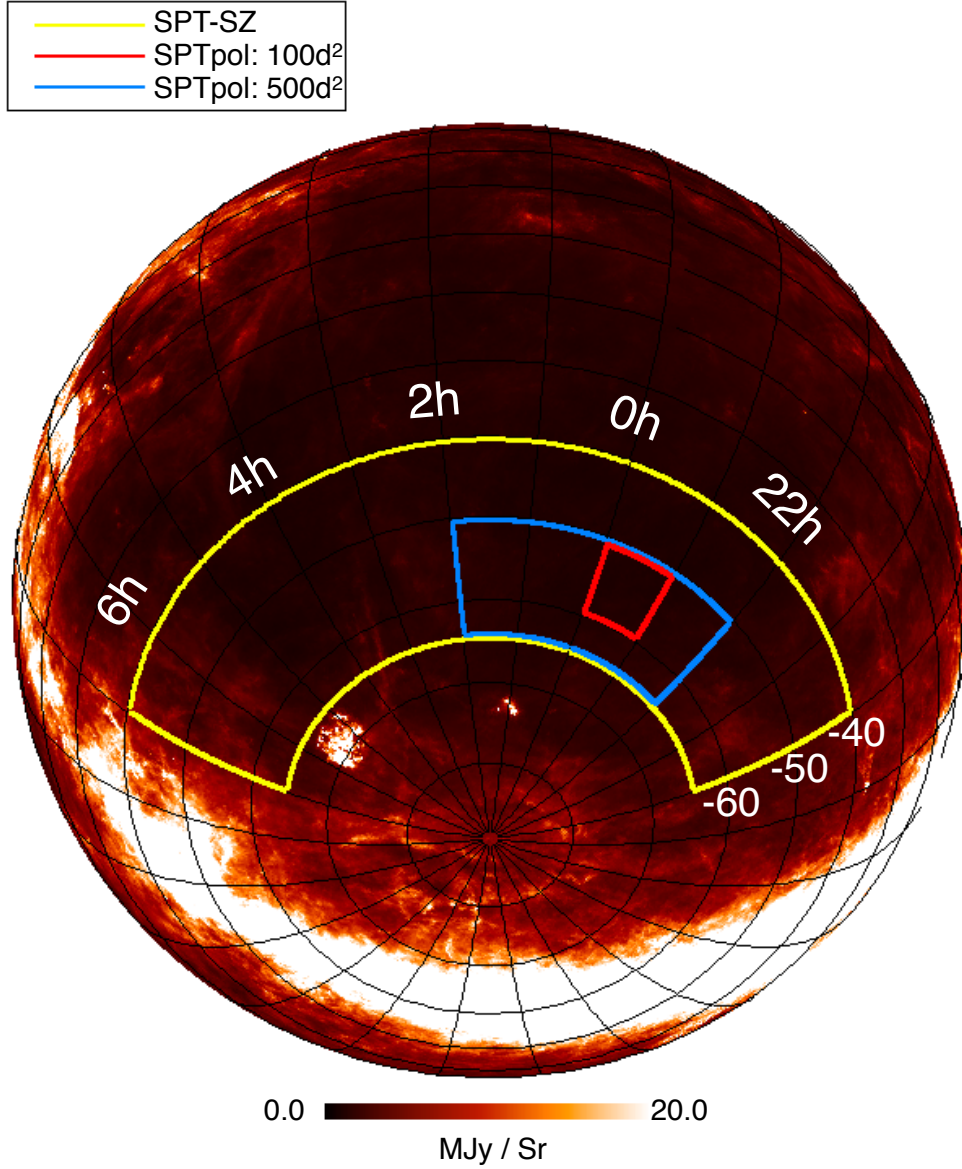


Figure 1.1: The SPT and SPTpol survey regions are shown here, overlaid on an orthographic projection of the IRAs 100 μm dust map from [112]. The 2500 deg^2 SPT-SZ survey is outlined in **yellow**. The 100 deg^2 SPTpol “deep field” is outlined in **red**. The ongoing 500 deg^2 SPTpol “survey field” is outlined in **blue**. Results presented in chapter 2 use data from the SPT-SZ survey, while results presented in chapter 3 use data from the SPTpol deep field.

CHAPTER 2

CMB TEMPERATURE POWER SPECTRUM

Measurements of the anisotropy of the CMB have shaped our understanding of cosmology. These measurements have improved dramatically since the first measurements of CMB anisotropy by the *COBE* satellite [122]. On degree scales, CMB anisotropy is primarily generated by the acoustic oscillations of the primordial plasma in the early universe (see section 1.0.1). The Wilkinson Microwave Anisotropy Probe (*WMAP*) satellite has been used to measure these acoustic oscillations with cosmic variance-limited precision on angular scales corresponding to $\ell \lesssim 500$ ¹ [76, hereafter *WMAP7*]. On much smaller angular scales, primary CMB anisotropy becomes dominated by effects imprinted on the CMB at low redshift (so-called secondary anisotropy) and foregrounds; at millimeter wavelengths, this transition occurs at $\ell \sim 3000$. This small-angular scale millimeter-wavelength anisotropy has been measured by the SPT [86, 119, 106] and the Atacama Cosmology Telescope [ACT, 44, 31].

The anisotropy in the CMB at intermediate angular scales, $1000 \lesssim \ell \lesssim 3000$, is often referred to as the “damping tail” since the anisotropy power on these angular scales is damped by photon diffusion during recombination [120]. Adding measurements of the damping tail to large-scale CMB measurements considerably tightens the resulting cosmological constraints. Therefore measurements on smaller angular scales are sensitive to the photon diffusion scale during recombination. The wider range of angular scales also enables better constraints on the sound horizon at recombination (by measuring more acoustic peaks) and the slope of the primordial power spectrum. Finally, although tensor perturbations from cosmic inflation add CMB power only at very large angular scales, the effect of these tensor perturbations is degenerate with changes in n_s in large-scale measurements. Damping tail measurements help break this degeneracy, thus tightening constraints on the level of tensor perturbations.

1. These results use measurements of the CMB anisotropy at large angular scales from *WMAP7*, which were the most precise at the time of submission (October 2012). Subsequently, *Planck* has published measurements of the CMB temperature and polarization anisotropy [99, 100, 97, 98].

In the past decade, there have been several increasingly precise measurements of the CMB damping tail, including the Arcminute Cosmology Bolometer Array Receiver [ACBAR, 105], QUaD [17, 45], ACT [32], and SPT [69, hereafter K11]. The most precise published measurement of the CMB damping tail prior to this work comes from the first 790 deg² of the South Pole Telescope Sunyaev-Zel’dovich (SPT-SZ) survey (K11).

In this chapter, we present a measurement of the power spectrum from the third acoustic peak through the CMB damping tail, covering the range of angular scales corresponding to multipoles $650 < \ell < 3000$. This power spectrum is calculated from the complete SPT-SZ survey covering 2540 deg² of sky, and improves upon the results presented in K11 by expanding the sky coverage by a factor of three. This chapter contains the results from [129].

We present constraints from this measurement on the standard Λ CDM model of cosmology, then extend the model to quantify the amplitude of gravitational lensing of the CMB. We use this sensitivity to gravitational lensing by large-scale structure at low redshifts to measure the mean curvature of the observable universe from CMB data alone. We also consider models including tensor perturbations, and explore implications of the resulting parameter constraints for simple models of inflation. Adding low-redshift measurements of the Hubble constant (H_0) and the baryon acoustic oscillation (BAO) feature to the CMB data further tightens parameter constraints, and we present combined parameter constraints for each of the above model extensions. The implications of the SPT power spectrum for a larger range of extensions to the standard cosmological model are explored more fully in [57, hereafter H14].

This chapter is organized as follows. We describe the SPT observations and data reduction in §2.1. We present the power spectrum calculation in §2.2. We discuss tests for systematic errors in §2.3.1. We present the power spectrum measurement in §2.4. In §2.5, we outline our cosmological parameter fitting framework and present the resulting parameter constraints, then use these constraints to explore the implications for simple models of

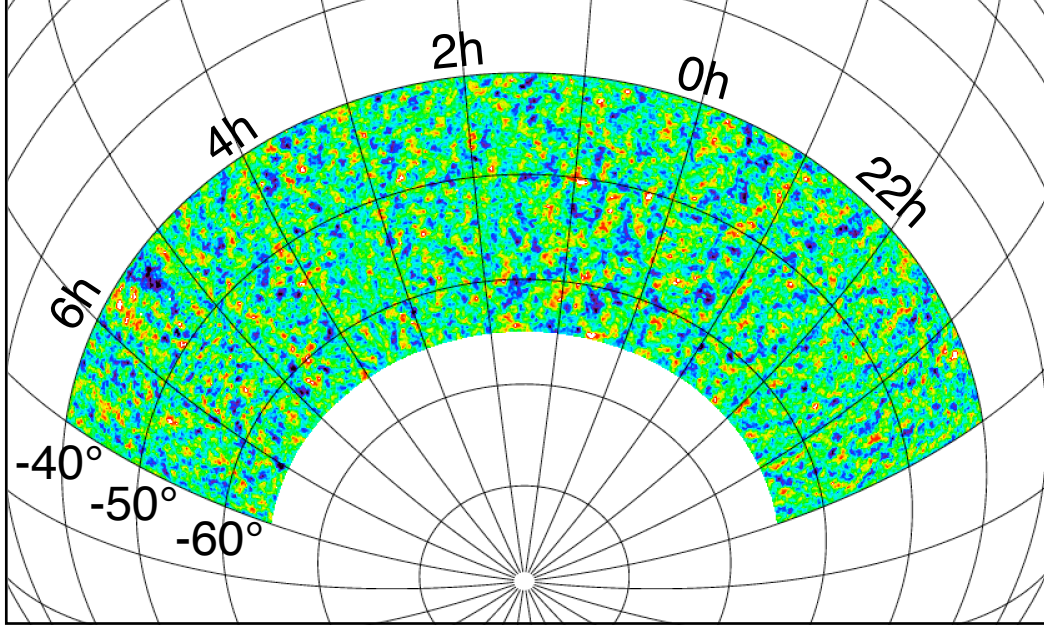


Figure 2.1: The 2500 deg² SPT-SZ survey. We show the full survey region with lightly filtered 95 GHz data from the SPT, using the data and filters which best capture the degree-scale anisotropy of the CMB visible in this figure. The power spectrum measurement reported in this chapter is calculated from 2540 deg² of sky and analyzes 150 GHz data with a different high-pass filter, as described in § 2.1.2.

inflation. Finally, we conclude in §2.6.

2.1 Observations and Data Reduction

This work uses ~ 2500 deg² of data taken with the SPT during the SPT-SZ survey (see section 1.0.5). The observations and data reduction methods used here are very similar to those described in K11. In this section, we give an overview of the observations and data reduction, highlighting the differences with the treatment in K11; we refer the reader to K11 for a detailed treatment of the analysis methods.

2.1.1 Observing Strategy and Fields

From 2008 - 2011, the SPT was used to observe a contiguous $\sim 2500 \text{ deg}^2$ patch of sky to a noise level of approximately $18 \mu\text{K-arcmin}$ at 150 GHz .² This area of sky was observed in 19 contiguous sub-regions which we refer to as observation “fields”. In the basic survey strategy, the SPT was used to observe a single field until the desired noise level was reached before moving on to the next field. Two fields were observed in 2008, three in 2009, five in 2010, and nine in 2011. All nine fields from 2011 were observed to partial depth in 2010 to search for massive galaxy clusters, then re-observed in 2011 to achieve nominal noise levels. The results of that bright cluster search were published in [137]. In terms of sky area, this equates to observing 167 deg^2 in 2008, 574 deg^2 in 2009, 732 deg^2 in 2010, and 1067 deg^2 in 2011. The fields are shown in Figure 2.2, and the field locations and sizes are presented in Table 2.1.

Both fields from 2008 (RA5H30DEC-55 and RA23H30DEC-55) were re-observed in later years to achieve lower than normal noise levels. In this analysis, we use data from only one year for each field because the beam and noise properties vary slightly between years. This choice simplifies the analysis without affecting the results as the bandpower uncertainties remain sample variance dominated (see Section 2.2.6).

The SPT is used to observe each field in the following manner. The telescope starts in one corner of the observation field, slews back and forth across the azimuth range of the field, and then executes a step in elevation, repeating this pattern until the entire field has been covered. This constitutes a single observation of the field, and takes from 30 minutes to a few hours, depending on the specific field being observed. Azimuthal scan speeds vary between fields, ranging from 0.25 to 0.42 degrees per second on the sky. The starting elevation positions of the telescope are dithered by between $0.3'$ and $1.08'$ to ensure uniform coverage of the region in the final coadded map.

2. The SPT-SZ survey also includes data at 95 and 220 GHz. However, this work uses only 150 GHz data since this observing band is the most sensitive for the SPT and the data from one observing band are sufficient to make high signal-to-noise maps of the CMB anisotropy.

In four of the 2008 and 2009 fields, RA23H30DEC-55, RA21HDEC-60, RA3H30DEC-60, and RA21HDEC-50, observations were conducted with a “lead-trail” strategy. In this observation strategy, the field is divided into two halves in right ascension. The “lead” half is observed first, immediately followed by the “trail” half in a manner such that both halves are observed over the same azimuthal range. If necessary, the lead-trail data could be analyzed in a way that cancels ground pickup. In this analysis, we combine lead-trail pairs into single maps, and verify that contamination from ground pickup is negligible – see below and Section 2.3.1 for details.

We apply several (often redundant) data quality cuts on individual observations using the following criteria: map noise, noise-based bolometer weight, the product of median bolometer weight with map noise, and the sum of bolometer weights over the full map. For these cuts, we remove outliers both above and below the median value for each field. We do not use observations that are flagged by one or more of these cuts. We also flag observations with only partial field coverage. Finally, we cut maps that were made from observations in azimuth ranges that could be more susceptible to ground pickup over the angular scales of interest. We use “ground-centered” maps to measure ground pickup on large ($\ell \sim 50$) scales, and cut observations that were made at the azimuths with the worst 5% ground pickup to minimize potential ground-pickup on smaller angular scales. Although this cut does have an impact on our null tests (see Section 2.3.1), we emphasize that it does not significantly change the power spectrum, the precision of which is limited by sample variance.

2.1.2 Map-making: Time Ordered Data to Maps

As the SPT scans across the sky, the response of each detector is recorded as time-ordered data (TOD). These TOD are recorded at 100 Hz and have a Nyquist frequency of 50 Hz, which corresponds to a multipole number parallel to the scan direction (ℓ_x) between 72,000 and 43,000 at the SPT scan speeds. Since we report the power spectrum only up to $\ell = 3000$, we can benefit computationally by reducing the sampling rate. We choose a low-

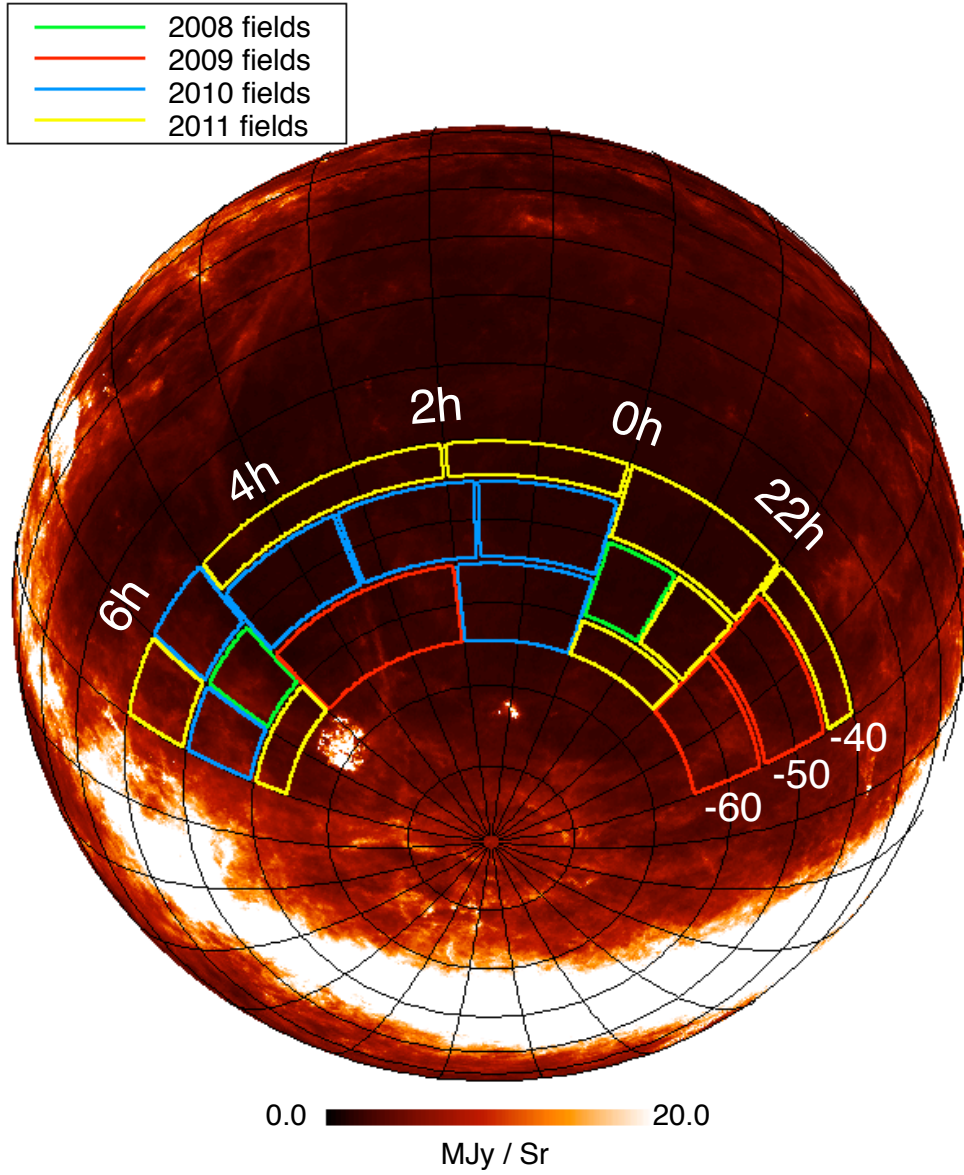


Figure 2.2: The SPT was used to observe 2500 deg^2 over 19 individual fields, which are overlaid here on an orthographic projection of the IRAS $100 \mu\text{m}$ dust map from [112]. These observation fields were chosen to lie in regions of low dust emission (dark red).

Table 2.1: The fields observed with the SPT between 2008 and 2011

Name	R.A. (°)	Decl. (°)	Δ R.A. (°)	Δ Decl. (°)	Effective Area (deg ²)
RA5H30DEC-55	82.7	-55.0	15	10	84
RA23H30DEC-55	352.5	-55.0	15	10	83
RA21HDEC-60	315.0	-60.0	30	10	155
RA3H30DEC-60	52.5	-60.0	45	10	227
RA21HDEC-50	315.0	-50.0	30	10	192
RA4H10DEC-50	62.5	-50.0	25	10	156
RA0H50DEC-50	12.5	-50.0	25	10	157
RA2H30DEC-50	37.5	-50.0	25	10	157
RA1HDEC-60	15.0	-60.0	30	10	152
RA5H30DEC-45	82.5	-45.0	15	10	109
RA6H30DEC-55	97.5	-55.0	15	10	85
RA23HDEC-62.5	345.0	-62.5	30	5	75
RA21HDEC-42.5	315.0	-42.5	30	5	121
RA22H30DEC-55	337.5	-55.0	15	10	84
RA23HDEC-45	345.0	-45.0	30	10	217
RA6HDEC-62.5	90.0	-62.5	30	5	75
RA3H30DEC-42.5	52.5	-42.5	45	5	179
RA1HDEC-42.5	15.0	-42.5	30	5	119
RA6H30DEC-45	97.5	-45.0	15	10	111
Total					2540

Table 2.2: The locations and sizes of the fields observed by the SPT between 2008 and 2011. For each field we give the center of the field in Right Ascension (R.A.) and declination (decl.), the nominal extent of the field in Right Ascension and declination, and the effective field area as defined by the window (see Section 2.2.2).

pass filter and down-sampling factor based on each field’s scan speed such that they affect approximately the same angular scales. We use a down-sampling factor of 6 for 2008 and 2009, and 4 for 2010 and 2011 with associated low-pass filter frequencies of 7.5 and 11.4 Hz respectively. These filtering choices remove a negligible amount of power in the signal band.

Next, the down-sampled TOD are bandpass filtered between $\ell_x = 270$ and 6600. The low-pass filter is necessary to avoid aliasing high-frequency noise to lower frequencies during map-making. The high-pass filter reduces low-frequency noise from the atmosphere and instrumental readout. The high-pass filter is implemented by fitting each bolometer’s TOD (from a single azimuthal scan across the field) to a model consisting of low-frequency sines and cosines and a fifth-order polynomial. The best-fit model is then subtracted from the TOD. During the filtering, we mask regions of sky within 5 arcminutes of point sources with fluxes of $S_{150\text{GHz}} > 50$ mJy. These regions are also masked in the power spectrum analysis, see Section 2.2.2.

At this stage, the TOD retain signal from the atmosphere that is correlated between detectors. We remove the correlated signal by subtracting the mean signal across each detector module for every time sample.³ This process acts as an approximately isotropic high-pass filter.

The filtered TOD are made into maps using the process described by K11. The data from each detector receive a weight based on the power spectral density of that detector’s calibrated TOD in the 1-3 Hz band. This band corresponds approximately to the signal band of this analysis. We have calculated the level of bias introduced by using the full (signal + noise) power to calculate the detector weights, as opposed to using the noise power only [40], and we find that the level of bias is completely negligible ($\leq 0.01\%$ in power). The detector data are binned into maps with $1'$ pixels based on the telescope pointing information. In the power spectrum analysis presented in Section 2.2, we adopt the flat-sky approximation, where

3. The SPT-SZ focal plane has a hexagonal geometry with six triangular bolometer modules, each with ~ 160 detectors. Each module is configured with a set of filters that determines its observing frequency of 95, 150, or 220 GHz.

the wavenumber k is equivalent to multipole moment ℓ and spherical harmonic transforms are replaced by Fourier transforms. We project from the curved celestial sky to flat-sky maps with the oblique Lambert equal-area azimuthal projection [123].

2.1.3 Beam Functions

A precise measurement of the SPT beam — the optical response as a function of angle — is needed to calibrate the angular power spectrum as a function of multipole. We summarize the method used to measure the SPT beams and refer the reader to K11 or [111] for a more detailed description.

The average 150 GHz beam is measured for each year using a combination of maps from Jupiter, Venus, and the 18 brightest point sources in the CMB fields. The maps of Jupiter are used to measure the beam outside a radius of $4'$, while the maps of the bright point sources are used to measure the beam inside that radius. Maps of Venus are used to join the inner and outer beam maps into a composite beam map. The maps of the planets are not used to estimate the very inner beam due to a non-linear detector response when directly viewing bright sources and the non-negligible angular size of the planets compared to the beam. We use the composite beam map to measure the beam function B_ℓ , defined as the azimuthally averaged Fourier transform of the beam map. We consider uncertainties in the measurement of B_ℓ arising from several statistical and systematic effects, such as residual atmospheric noise in the maps of Venus and Jupiter, and account for known inter-year correlations of some of these sources of uncertainty. The parameter constraints quoted in this work are not sensitive to the calculated beam uncertainties; we have tested increasing our beam uncertainties by a factor of two and have seen no significant impact on the resulting cosmological parameter fits.

A nearly identical beam treatment was used by K11. The main difference is that the beam function was normalized to unity at $\ell = 350$ in K11 rather than $\ell = 750$ in this work. The average multipole of our calibration region is close to $\ell = 750$, and this choice of

normalization scale better decouples the beam and calibration uncertainties.

2.1.4 Calibration

The observation-to-observation relative calibration of the TOD is determined from repeated measurements of a galactic HII region, RCW38. As in K11 and [106], the absolute calibration is determined by comparing the SPT and *WMAP7* power in several ℓ -bins over the multipole range $\ell \in [650, 1000]$. We use the same ℓ -bins for both experiments: seven bins with $\delta\ell = 50$. This calibration method is model-independent, requiring only that the CMB power in the SPT fields is statistically representative of the all-sky power. We estimate the uncertainty in the SPT power calibration to be 2.6%. The calibration uncertainty is included in the covariance matrix; this treatment is equivalent to including an additional calibration parameter with a 2.6% Gaussian uncertainty in the cosmological parameter fits. We have also cross-checked this method against a map-based calibration method, in which we calculate the cross-spectrum between identically filtered SPT and WMAP maps over 1250 deg² of sky, and find that the calibrations between these two methods are consistent, though the map-based calibration uncertainties are larger. We do not find the parameter constraints quoted in this work to be sensitive to the calibration uncertainty; changing the calibration uncertainty by a factor of two in either direction has no significant impact on the resulting cosmological parameter fits.

2.2 Power Spectrum

In this section, we describe the power spectrum calculation. This analysis closely follows the analysis developed by [86] and used by K11; we refer the reader to those papers for a more detailed description. We refer to the average power over a given range of ℓ values as a *bandpower*. We use a pseudo- C_ℓ method under the flat-sky approximation as described in Section 2.1.2. The power spectra are calculated independently in each of the 19 fields, then

combined into the final result. We report bandpowers in terms of D_ℓ , which is defined as

$$D_\ell = \frac{\ell(\ell+1)}{2\pi} C_\ell. \quad (2.1)$$

To calculate D_ℓ , we use a cross-spectrum bandpower estimator as described in Section 2.2.3, which has the advantage of being free of noise bias; see [86] for a more detailed description.

2.2.1 Maps

The basic input to the cross-spectrum estimator is a set of maps for a given field, each with independent noise. For most fields, this input set is comprised of maps from single observations. Each observation has statistically independent noise because observations are temporally separated by at least an hour and the TOD have been high-pass filtered at ~ 0.2 Hz. As in K11, for the four fields observed with a lead-trail strategy, we construct the input map set by combining lead-trail pairs into single maps. The RA23H30DEC-55 field was observed using comparatively large elevation steps and hence has less uniform coverage. For this field, the single maps that serve as the basic input to the cross-spectrum estimator are formed by combining two pairs of lead-trail observations. Each pair is chosen to have different elevation dithers, leading to a more homogeneous field coverage.

2.2.2 Window

For a given field, each of the maps is multiplied by the same window \mathbf{W} in order to avoid sharp edges at map boundaries, control overlap between adjacent fields, and remove bright point sources. Each window is the product of an apodization mask with a point source mask. The apodization masks are calculated by applying a 1° taper using a Hann function to the edges of the uniform coverage region of each field. The observations were designed such that the uniform coverage region overlaps between neighboring fields. We define our apodization windows such that the overlap region between adjacent fields contains a combined weight

that approaches but never exceeds unity (the weight at the center of the field). This process results in apodization windows that include marginally smaller regions of sky and fall off more slowly than the windows used in K11, which did not need to account for field overlap.

As was done in K11, we identify all point sources with 150 GHz flux > 50 mJy. Each of these point sources is masked with a $5'$ -radius disk that is tapered outside the disk using a Gaussian taper with a width of $\sigma_{\text{taper}} = 5'$. Point source masks remove 1.4% of the total sky area. Using previous measurements of the mm-wave point source population [134, 119], we estimate that the power from residual point sources below this flux cut is $C_\ell \sim 1.3 \times 10^{-5} \mu\text{K}^2$, or $D_\ell \sim 18 \mu\text{K}^2 \left(\frac{\ell}{3000}\right)^2$. This power is approximately half the CMB anisotropy power at $\ell = 3000$, the upper edge of the multipole range reported in this analysis. Further discussion of the point source model is reserved for Section 2.5.1.

2.2.3 Cross-Spectra

The next step in calculating the power spectrum is to cross-correlate single maps from different observations of the same field. We use this cross-spectrum analysis - as opposed to calculating the auto-spectrum of coadded observations - because it is free of noise bias. Each map is multiplied by the window for its field, zero-padded to the same size for all fields, then the Fourier transform of the map \tilde{m}^A is calculated, where A is the observation index. The resulting Fourier-space maps have pixels of size $\delta_\ell = 5$ on a side. We calculate the average cross spectrum between the maps of two observations A and B within an ℓ -bin b :

$$\hat{D}_b^{AB} \equiv \left\langle \frac{\ell(\ell+1)}{2\pi} H_\ell \text{Re}[\tilde{m}_\ell^A \tilde{m}_\ell^{B*}] \right\rangle_{\ell \in b}, \quad (2.2)$$

where H_ℓ is a two-dimensional weight array described below, and ℓ is a vector in two-dimensional ℓ -space. Each field typically has about 200 single maps in the input set (see Section 2.2.1), resulting in $\sim 20,000$ cross-spectra. We average all cross-spectra \hat{D}_b^{AB} for $A \neq B$ to calculate a binned power spectrum \hat{D}_b for each field.

Due to our observation strategy, the maps have statistically anisotropic noise; at fixed ℓ , modes that oscillate perpendicular to the scan direction ($\ell_x = 0$) are noisier than modes that oscillate parallel to the scan direction. This anisotropic noise – and the filtering we apply to reduce the noise (see Section 2.1.2) – causes different modes in a given ℓ bin to have different noise properties. As in K11, we use a two-dimensional weight $H_{\boldsymbol{\ell}}$ which accounts for the anisotropic noise in the maps. We define the weight array according to

$$H_{\boldsymbol{\ell}} \propto (C_{\ell}^{\text{th}} + N_{\boldsymbol{\ell}})^{-2}, \quad (2.3)$$

where C_{ℓ}^{th} is the theoretical power spectrum used in simulations described in Section 2.2.5, and $N_{\boldsymbol{\ell}}$ is the two-dimensional calibrated, beam-deconvolved noise power, which is calculated from difference maps in which the right-going scans are subtracted from the left-going scans. The weight array is then smoothed with a Gaussian kernel of width $\sigma_{\ell} = 450$ to reduce the scatter in the noise power estimate, and normalized to the maximum value in each annulus. $H_{\boldsymbol{\ell}}$ is calculated independently for each observation field.

2.2.4 Unbiased Spectra

The power \hat{D}_b is a biased estimate of the true sky power, D_b , due to effects such as TOD filtering, projection effects, and mode mixing from the window. The biased and unbiased estimates are related by

$$\hat{D}_{b'} \equiv K_{b'b} D_b, \quad (2.4)$$

where the K matrix accounts for the effects of the beams, TOD filtering, pixelization, windowing, and band-averaging. K can be expanded as

$$K_{bb'} = P_{b\ell} \left(M_{\ell\ell'}[\mathbf{W}] F_{\ell'} B_{\ell'}^2 \right) Q_{\ell'b'}. \quad (2.5)$$

$Q_{\ell\ell'}$ is the binning operator and $P_{b\ell}$ is its reciprocal [56]. The “mode-coupling matrix” $M_{\ell\ell'}[\mathbf{W}]$ accounts for mixing modes between multipole moments which arises from observing a finite portion of the sky. We calculate $M_{\ell\ell'}[\mathbf{W}]$ analytically from the window function \mathbf{W} following the prescription described by [86]. Over the range of multipoles reported in this analysis, the elements of the mode-coupling matrix depend only on the distance from the diagonal. F_ℓ is the transfer function due to TOD filtering and map pixelization, which is described in Section 2.2.5. B_ℓ^2 is the beam function described in Section 2.1.3. For sufficiently large ℓ -bins, the K matrix is invertible, allowing an unbiased estimate of the true sky power:

$$D_b \equiv \left(K^{-1}\right)_{bb'} \hat{D}_{b'}. \quad (2.6)$$

2.2.5 Simulations and the Transfer Function

The transfer function F_ℓ is calculated from end-to-end simulations. One hundred full-sky realizations are generated at a Healpix⁴ resolution of $N_{\text{side}}=8192$. These simulated skies include gravitationally lensed CMB anisotropy based on the best-fit Λ CDM model from K11, a Poisson distribution of radio galaxies, and Gaussian realizations of the thermal and kinematic Sunyaev-Zel’dovich (SZ) effects and cosmic infrared background (CIB). The lensed realizations of the CMB spectrum are generated out to $\ell = 8000$ using LensPix [79]. The Poisson radio galaxy contribution is based on the Dezotti model [35] for sources below the 5σ detection threshold in the SPT-SZ survey, and the observed counts [134] above that flux. The shape of the thermal SZ spectrum is taken from [116] with an amplitude taken from [106]. The kinematic SZ spectrum is based on the fiducial model in [138]. The CIB spectrum is taken from the best-fit values in [106].

Unlike the simulations in K11, these simulations cover the full sky. The full-sky simulations make it simple to account for overlap between fields when calculating the sample variance term of the bandpower covariance matrix (see Section 2.2.6). These simulations

4. <http://healpix.jpl.nasa.gov>

also account for any effects due to projecting from the curved sky to flat sky maps to first order in the transfer function, though these effects should be negligible, as argued in K11.

These simulated skies are observed using the SPT pointing information recorded during observations and then filtered and processed into maps using the same pipeline as for the real data. For each field, we calculate the transfer function by comparing the average power spectrum of these simulated maps to the known input spectrum using an iterative scheme [56].

The transfer function is equal to ~ 0.25 at $\ell = 650$ and reaches a plateau for $\ell \gtrsim 1200$. The transfer function does not reach unity at any scale due to the strong filtering of $\ell_x \lesssim 300$ modes.

2.2.6 Bandpower Covariance Matrix

The bandpower covariance matrix quantifies the bin-to-bin covariance of the unbiased spectrum. The covariance matrix contains signal and noise terms as well as terms accounting for beam and calibration uncertainties. The signal term, often referred to as “sample variance”, is calculated from the 100 simulations described in section 2.2.5. For each simulated Healpix sky, we calculate the combined power spectrum from all fields, then measure the variance of these 100 estimates. This process naturally accounts for any overlap between fields. The noise term, or “noise variance”, is estimated directly from the data using the distribution of individual cross-spectra D_b^{AB} as described by [86]. The sample variance is dominant at multipoles below $\ell \lesssim 2900$. At smaller angular scales, the noise variance dominates.

The initial estimate of the bandpower covariance matrix has low signal-to-noise on the off-diagonal elements. As in K11, we condition the covariance matrix to reduce the impact of this uncertainty.

We must also account for the bin-to-bin covariance due to the uncertainties in the beam function B_ℓ . We construct a “beam correlation matrix” for each source of beam uncertainty:

$$\boldsymbol{\rho}_{ij}^{beam} = \left(\frac{\delta D_i}{D_i} \right) \left(\frac{\delta D_j}{D_j} \right) \quad (2.7)$$

where

$$\frac{\delta D_i}{D_i} = 1 - \left(1 + \frac{\delta B_i}{B_i} \right)^{-2}. \quad (2.8)$$

We sum these matrices to find the full beam correlation matrix, and convert to a covariance matrix according to

$$\mathbf{C}_{ij}^{beam} = \boldsymbol{\rho}_{ij}^{beam} D_i D_j. \quad (2.9)$$

2.2.7 Combining Fields

The analysis described in the previous sections produces 19 sets of bandpowers and covariance matrices, one from each field. In either the limit of equal noise or the limit of sample variance domination, the optimal weight for each field would be its effective area (i.e., the integral of its window). Since we are approximately in these limits, we use area-based weights. Thus the combined bandpowers and covariance matrix are given by

$$D_b = \sum_i D_b^i w^i \quad (2.10)$$

$$\mathbf{C}_{bb'} = \sum_i \mathbf{C}_{bb'}^i (w^i)^2 \quad (2.11)$$

where

$$w^i = \frac{A^i}{\sum_i A^i} \quad (2.12)$$

is the area-based weight of the i^{th} field. The area A^i is the sum of the window for the i^{th} field.

We calculate the final covariance matrix as the sum of the signal plus noise covariance matrix, the beam covariance matrix, and the calibration covariance matrix. For the signal and noise terms, we combine the signal plus noise covariance matrices from all fields using

Equation 2.11. We condition this combined covariance matrix using Equation 11 from K11. For the beam covariance matrix, we take the beam covariance matrices for each year (see Section 2.2.6), and combine them into one composite beam covariance matrix using the area-based weight scheme. In this step, we take care to account for the beam errors that are correlated between years. Finally, we add the calibration covariance matrix, defined as $\mathbf{C}_{ij}^{cal} = \epsilon^2 D_i D_j$, where $\epsilon = 0.026$ is the 2.6% uncertainty in the SPT power calibration discussed in Section 2.1.4.

2.2.8 Bandpower Window Functions

Bandpower window functions are necessary to compare the measured bandpowers to a theoretical power spectrum. The window function \mathcal{W}_ℓ^b/ℓ is defined as

$$C_b^{\text{th}} = (\mathcal{W}_\ell^b/\ell) C_\ell^{\text{th}}. \quad (2.13)$$

Following the formalism described in Section 2.2.4, we can write this as

$$C_b^{\text{th}} = (K^{-1})_{bb'} P_{b'\ell'} M_{\ell'\ell} F_\ell B_\ell^2 C_\ell^{\text{th}}, \quad (2.14)$$

which implies that⁵

$$\mathcal{W}_\ell^b/\ell = (K^{-1})_{bb'} P_{b'\ell'} M_{\ell'\ell} F_\ell B_\ell^2. \quad (2.15)$$

We calculate the bandpower window functions to be used for the final spectrum measurement as the weighted average of the bandpower window functions from each field.

5. Note: due to conventions in the CosmoMC package, the window functions from the publicly downloadable “Newdat” files should be used as follows:

$$C_b^{\text{th}} = \left(\mathcal{W}_\ell^b \frac{(\ell + 0.5)}{(\ell + 1)} \right) C_\ell^{\text{th}}$$

2.3 Tests for Systematic Errors

It is important to verify that the data are unbiased by systematic errors. We perform two types of tests: null tests and pipeline tests.

2.3.1 Null Tests

As is common in CMB analyses, we check for possible systematic errors by performing a suite of null tests which are frequently referred to as jackknife tests. In each null test, all observations are divided into two equally sized sets based on a possible source of systematic error. Difference maps are then calculated by subtracting the two sets, thus removing the astrophysical signal. The power spectrum of the difference maps is calculated as described in the last section. This spectrum is compared to an “expectation spectrum,” the power we expect to see in the absence of contamination from systematic errors. The expectation spectrum will generically be non-zero due to small differences in observation weights, filtering, etc, and is calculated by applying the null test to simulated maps. The expected power is small ($D_\ell < 2\mu\text{K}^2$ at all multipoles) for all tests.

We perform six null tests:

- Time: Observations are ordered by time, then divided into first-half and second-half sets. This tests for long-term temporally varying systematic effects.
- Scan Direction: Observations are divided into maps made from left-going scans and right-going scans. This tests for scan-synchronous and scan-direction-dependent systematic errors.
- Azimuthal Range: We split the data into observations taken at azimuths that we expect to be more or less susceptible to ground pickup. These azimuth ranges are determined from maps of the 2009 data made using “ground-centered” (Azimuth/Elevation) coordinates in which ground pickup adds coherently, as opposed to the usual “sky-centered”

(R.A./decl.) coordinates. We use the ground-centered maps that were made for the analysis presented by K11. Although we detect emission from the ground on large scales ($\ell \sim 50$) in these ground-centered maps, this is not expected to bias our measurement; the amplitude of the ground pickup is significantly lower on the smaller angular scales for which the bandpowers are being reported, and the observations for a given field are distributed randomly in azimuth. We use the azimuth-based null test to verify this assertion.

- Moon: Observations are divided into groups based on when the Moon was above and below the horizon.
- Sun: Observations are divided into groups based on when the Sun was above and below the horizon. In this test, we include only fields in which more than 25% of the observations were taken with the Sun above the horizon.
- Summed Bolometer Weights: We calculate the sum of all bolometer weights during each observation and order maps based on this sum. This tests for bias introduced by incorrectly weighting observations or incomplete coverage in some maps.

For each test, the χ^2 of the residual power is calculated relative to the expectation spectrum in five bins with $\delta\ell = 500$. We calculate the probability to exceed (PTE) this value of χ^2 for five degrees of freedom. All null tests had reasonable PTEs, as listed in the next paragraph, with the exception of the Azimuthal Range null test, which produced a low PTE for the original set of observations. This was interpreted as evidence for some ground contamination. This interpretation was tested by cutting several sets of 5% of the data, and re-calculating the Azimuthal Range null test. Removing random 5% sets of the data did not change the failure of the Azimuthal Range null test. However, cutting the 5% of the observations from each field with the highest expected ground contamination resulted in passing the Azimuthal Range null test. Thus this cut was included with the other observation cuts, as described in Section 2.1.1. It is worth noting that the Azimuthal Range null test is

the worst-case scenario for ground pickup; this null test systematically aligns azimuth ranges to maximize the ground contamination. In the analysis of the power spectrum of the sky signal, the ground signal will add incoherently as the azimuth changes, thus reducing the power from ground contamination to a much lower level than in this null test.

We find a flat distribution of PTEs ranging from 0.02 to 0.99 for individual fields. The combined PTEs for the Time, Scan Direction, Azimuthal Range, Moon, Sun, and Summed Bolometer Weights are 0.26, 0.14, 0.17, 0.13, 0.30, 0.63, respectively. It is important to note that these null tests are extremely conservative for the SPT power spectrum where the uncertainties are sample variance dominated over most of the range reported in this work. It is possible to have a failure in these null tests without a significant impact on the final power spectrum. The measured power D_ℓ in each null test was less than $2.2 \mu K^2$ in all bins.

Though we cannot perform a direct year-to-year null test because the data for any given field was taken within a single year, we have verified that the spectra from different years (and therefore different fields, including those used in K11) are consistent within the uncertainties of cosmic variance.

2.3.2 Pipeline Tests

We test the robustness of our pipeline with simulations. In these tests, we create simulated maps with an input spectrum that differs from the Λ CDM model spectrum assumed in the calculation of the transfer function. We then use our full pipeline to calculate the power spectrum of these simulated maps, and compare this spectrum with the input spectrum. We looked at three categories of modifications:

- A slope was added to the best-fit Λ CDM spectrum from K11. This tests how well we can measure the slope of the damping tail.
- An additional Poisson point-source power term was added (see Section 2.5.1).
- The input spectrum was shifted by $\delta_\ell = 10$. This tests how well we can measure the

locations of the acoustic peaks, and therefore θ_s .

In all cases, we recover the input spectrum to well within our uncertainties.

We thus find no significant evidence for systematic contamination of SPT bandpowers.

2.4 Bandpowers

Following the analysis presented in Section 2.2, we measure the CMB temperature anisotropy power spectrum from 2540 deg² of sky observed by the SPT between 2008 and 2011. We report bandpowers in bins of $\delta\ell = 50$ between $650 < \ell < 3000$. The bandpowers and associated errors are listed in Table 2.3 and shown in Figures 2.3 and 2.4. The bandpowers, covariance matrix, and window functions are available for download on the SPT website.⁶

These bandpowers clearly show the third to ninth acoustic peaks. As Figure 2.4 demonstrates, the anisotropy power measured by this analysis (at 150 GHz, with a 50mJy point-source cut) is dominated by primary CMB, with secondary anisotropy and foregrounds contributing significantly only at the highest multipoles. At the time [129] was submitted, these bandpowers provided the most precise measurement to date of the CMB power spectrum over the entire multipole range presented in this analysis.

2.5 Cosmological Constraints

The SPT bandpowers are high signal-to-noise measurements of the CMB temperature anisotropy over a large range of angular scales, and can be used to perform sensitive tests of cosmological models. In this section, we present the constraints these bandpowers place on cosmological models. We first constrain the standard Λ CDM cosmological model. Next, we extend this model to constrain the amplitude of gravitational lensing of the CMB. We then consider models with free spatial curvature and constrain the mean curvature of the observable universe.

6. <http://pole.uchicago.edu/public/data/story12/>

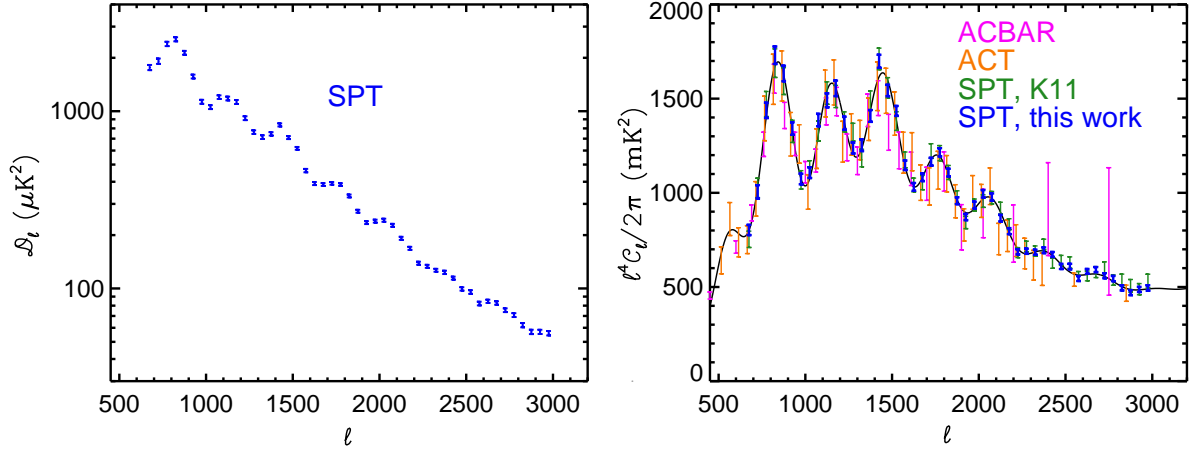


Figure 2.3: **Left panel:** The SPT power spectrum. The leftmost peak at $\ell \sim 800$ is the third acoustic peak. **Right panel:** A comparison of the new SPT bandpowers with other recent measurements of the CMB damping tail from ACBAR [105], ACT [32], and SPT (K11). Note that the point source masking threshold differs between these experiments which can affect the power at the highest multipoles. In order to highlight the acoustic peak structure of the damping tail, we plot the bandpowers in the right panel as $\ell^4 C_\ell / (2\pi)$, as opposed to $D_\ell = \ell(\ell + 1)C_\ell / (2\pi)$ in the left panel. The solid line shows the theory spectrum for the Λ CDM model + foregrounds that provides the best fit to the SPT+*WMAP*7 data. The bandpower errors shown in these plots contain sample and noise variance terms only; they do not include beam or calibration uncertainties.

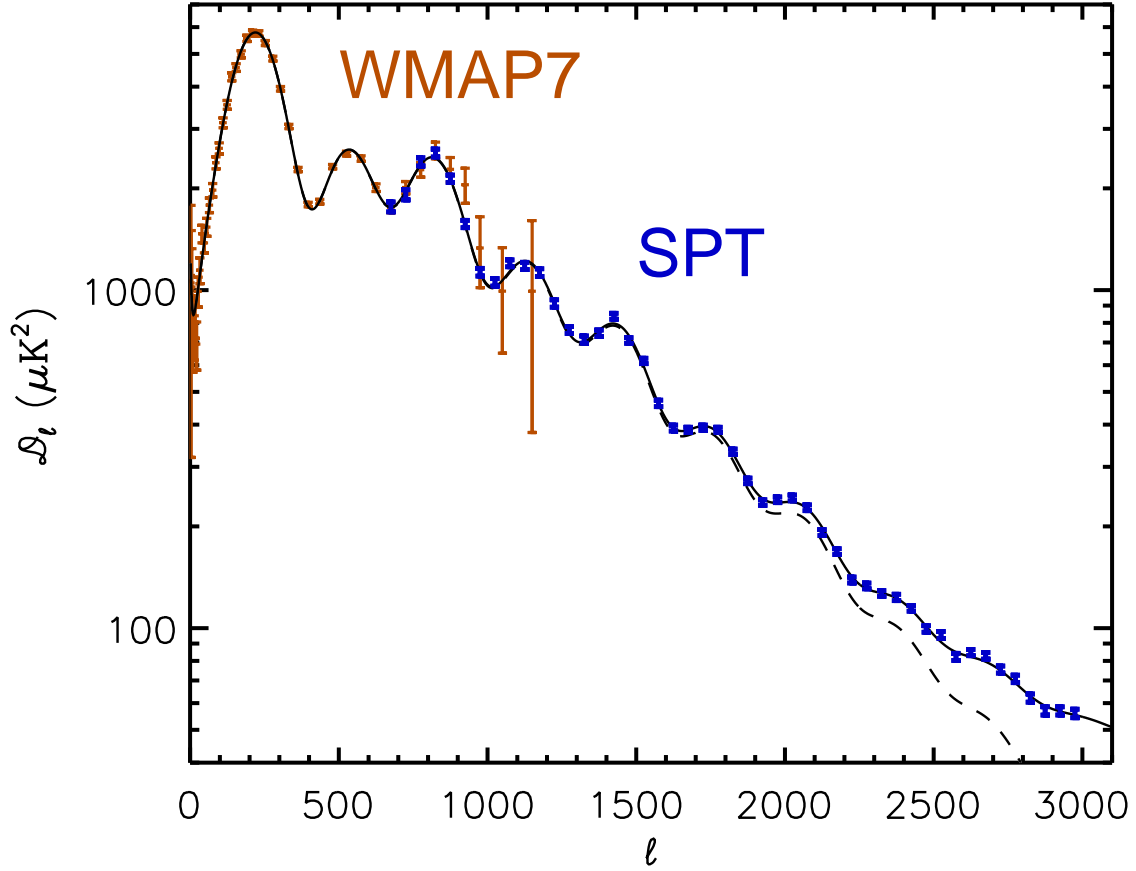


Figure 2.4: The SPT bandpowers (**blue**), *WMAP7* bandpowers (**orange**), and the lensed Λ CDM+foregrounds theory spectrum that provides the best fit to the SPT+*WMAP7* data shown for the CMB-only component (**dashed line**), and the CMB+foregrounds spectrum (**solid line**). As in Figure 2.3, the bandpower errors shown in this plot do not include beam or calibration uncertainties.

Table 2.3: SPT Bandpowers and Bandpower Errors

ℓ range	ℓ_{eff}	D_ℓ [μK^2]	σ [μK^2]	ℓ range	ℓ_{eff}	D_ℓ [μK^2]	σ [μK^2]
651 - 700	671	1786.2	59.5	1851 - 1900	1865	276.1	5.2
701 - 750	720	1939.3	66.9	1901 - 1950	1915	238.2	4.5
751 - 800	770	2426.4	67.2	1951 - 2000	1966	242.8	4.6
801 - 850	820	2577.1	68.3	2001 - 2050	2015	245.8	4.9
851 - 900	870	2162.3	53.8	2051 - 2100	2064	229.9	4.5
901 - 950	920	1588.8	39.0	2101 - 2150	2114	194.2	3.8
951 - 1000	969	1144.3	29.6	2151 - 2200	2164	170.6	3.4
1001 - 1050	1019	1068.0	27.2	2201 - 2250	2213	140.5	2.8
1051 - 1100	1069	1215.7	28.5	2251 - 2300	2265	135.0	2.6
1101 - 1150	1118	1193.8	29.1	2301 - 2350	2313	128.3	2.4
1151 - 1200	1169	1141.1	29.8	2351 - 2400	2364	124.8	2.7
1201 - 1250	1218	924.8	23.1	2401 - 2450	2413	115.8	2.2
1251 - 1300	1269	771.7	17.9	2451 - 2500	2462	100.7	2.2
1301 - 1350	1318	723.1	17.7	2501 - 2550	2512	96.7	2.3
1351 - 1400	1367	754.6	16.6	2551 - 2600	2562	83.3	2.0
1401 - 1450	1417	847.3	17.0	2601 - 2650	2613	85.7	1.8
1451 - 1500	1468	718.7	13.8	2651 - 2700	2663	83.9	1.9
1501 - 1550	1517	625.0	11.3	2701 - 2750	2712	76.4	1.8
1551 - 1600	1567	468.1	10.2	2751 - 2800	2761	71.7	1.8
1601 - 1650	1617	395.7	7.9	2801 - 2850	2811	62.9	1.7
1651 - 1700	1666	390.7	7.0	2851 - 2900	2860	57.6	1.6
1701 - 1750	1717	396.6	6.9	2901 - 2950	2910	57.6	1.6
1751 - 1800	1766	390.7	6.9	2951 - 3000	2961	56.6	1.6
1801 - 1850	1815	336.7	6.2				

Table 2.4: The ℓ -band range, weighted multipole value ℓ_{eff} , bandpower D_ℓ , and associated bandpower uncertainty σ of the SPT power spectrum. The errors are the square-root of the diagonal elements of the covariance matrix, and do not include beam or calibration uncertainties.

We finally consider tensor perturbations and discuss the implications of our observations for simple models of inflation. A wider range of cosmological models are tested in H14.

We parametrize the Λ CDM model with the six parameters described in section 1.0.2: $\Omega_b h^2$, $\Omega_c h^2$, τ , θ_s , $\Delta_R^2(k_0 = 0.05 \text{ Mpc}^{-1})$, and n_s . With the exception of Section 2.5.11, we consider only flat-universe models where the mean curvature of the observable universe $\Omega_k = 0$. In addition to the six parameters described above, we report several derived parameters that are calculated from the six Λ CDM parameters. These are the dark energy density Ω_Λ , the Hubble constant H_0 in units of $\text{km s}^{-1} \text{ Mpc}^{-1}$, the current amplitude of

linear matter fluctuations σ_8 on scales of $8 h^{-1}$ Mpc, the redshift of matter-radiation equality z_{eq} , and a hybrid distance ratio reported by baryon acoustic oscillation (BAO) experiments at two different redshifts $r_s/D_v(z = 0.35)$ and $r_s/D_v(z = 0.57)$, where r_s is the comoving sound horizon size at the baryon drag epoch, $D_V(z) \equiv [(1+z)^2 D_A^2(z) cz/H(z)]^{1/3}$, $D_A(z)$ is the angular diameter distance, and $H(z)$ is the Hubble parameter.

2.5.1 Foreground treatment

We marginalize over three foreground terms in all parameter fitting. The total foreground power, D_ℓ^{fg} , can be expressed as:

$$D_\ell^{\text{fg}} = D_\ell^{\text{gal}} + D_\ell^{\text{SZ}} \quad (2.16)$$

These two terms represent the following:

- *Power from galaxies* (D_ℓ^{gal}), which can be subdivided into a clustering term and a Poisson term. The Gaussian priors used by K11 are applied to the amplitude of each term at $\ell = 3000$. For the clustering term, the prior is $D_{3000}^{\text{CL}} = 5.0 \pm 2.5 \mu\text{K}^2$, based on measurements by [119]. The angular dependence of the clustering term is $D_\ell^{\text{CL}} \propto \ell^{0.8}$, which has been modified from that assumed by K11 to agree better with recent measurements (e.g., [1, 107]). For the Poisson term, the prior is $D_{3000}^{\text{PS}} = 19.3 \pm 3.5 \mu\text{K}^2$. This is based on the power from sources with $S_{150\text{GHz}} < 6.4$ mJy, as measured in [119], and the power from sources with $6.4 \text{ mJy} < S_{150\text{GHz}} < 50$ mJy, as measured in [134] and [87]. The Poisson term is constant in C_ℓ and thus varies as $D_\ell^{\text{PS}} \propto \ell^2$.
- *SZ power* (D_ℓ^{SZ}). The thermal and kinematic SZ effects are expected to contribute to the observed CMB temperature anisotropy. Both effects are expected to have similar power spectrum shapes over the angular scales relevant to this analysis. Therefore we adopt a single template to describe both effects. The chosen template is the thermal SZ model from [116]. We set a Gaussian prior on the amplitude of this term of

$D_{3000}^{\text{SZ}} = 5.5 \pm 3.0 \mu\text{K}^2$, as measured in [119]. This amplitude is defined at 153 GHz, corresponding to the effective SPT band center.

We have tested that all parameter constraints are insensitive to the details of the assumed foreground priors; we have completely removed the priors on the amplitudes of the foreground terms and re-calculated the best-fit ΛCDM model, and find all ΛCDM parameters shift by less than 0.06σ . Additionally, we see no evidence for significant correlations between the foreground and cosmological parameters.

In the above model, we have not accounted for the emission from cirrus-like dust clouds in the Milky Way. Repeating the calculation performed in K11, we cross-correlate the SPT maps with predictions for the galactic dust emission at 150 GHz in the SPT fields using model 8 of [43]. We use this cross-correlation to estimate the power from the galactic dust in the SPT fields, and find that it is small compared to the primary CMB power and the SPT bandpower errors. Specifically, subtracting this cirrus power can be balanced by moving the foreground terms by amounts that are small compared to their priors, so that the change in χ^2 is less than 0.1σ . The dust model can be improved in future analyses by cross-correlating SPT data with *Planck* 857 GHz maps (e.g., see [99]), though we expect this to have a negligible impact on cosmological parameters. Thus we conclude that galactic dust does not significantly contaminate the SPT power spectrum.

2.5.2 *Estimating Cosmological Parameters*

Our baseline model contains nine parameters: six for the primary CMB and three for foregrounds. We explore the nine-dimensional parameter space using a Markov Chain Monte Carlo (MCMC) technique [24] implemented in the CosmoMC⁷ [80] software package. For reasons of speed, we use PICO⁸ [42, 41], trained with CAMB⁹ [83], to calculate the CMB

7. <http://cosmologist.info/cosmomc/>

8. <https://sites.google.com/a/ucdavis.edu/pico>

9. <http://camb.info/> (January 2012 version)

power spectrum. We have trained PICO for a ten-parameter model that includes Λ CDM as well as several extensions. We use PICO when working with any subset of this model space, and CAMB for all other extensions to Λ CDM. The effects of gravitational lensing on the power spectrum of the CMB are calculated using a cosmology-dependent lensing potential [81]. To sample the posterior probability distribution in regions of very low probability, we run “high-temperature” chains in which the true posterior, P , is replaced in the Metropolis Hastings algorithm by $P_T = P^{1/6}$. This allows the chain to sample the parameter space more broadly. We recover the correct posterior from the chain by importance sampling each sample with weight P/P_T .

2.5.3 Goodness of fit to the Λ CDM Model

We quantify the goodness of fit of the Λ CDM model to the SPT bandpowers by finding the spectrum that best fits the SPT bandpowers and calculating the reduced χ^2 for the SPT data. The reduced χ^2 for the SPT data is 45.9/39 (PTE=0.21), thus the Λ CDM model is a good fit to the SPT bandpowers. In H14, we consider several extensions to the Λ CDM model, and find that the data show some preference (2σ to 3σ) for several of those extensions.

2.5.4 External Datasets

In this work, we focus on parameter constraints from the CMB data, sometimes in conjunction with measurements of the Hubble constant (H_0) or the BAO feature. For CMB measurements, we use the SPT bandpowers presented here as well as the *WMAP* bandpowers presented in *WMAP7*. For H_0 measurements, we use the low-redshift measurement from [108]. For the BAO feature, we use a combination of three measurements at different redshifts: the WiggleZ survey covering the redshift range $0.3 < z < 0.9$ [12], the SDSS-II survey (DR7) covering $0.16 < z < 0.44$ [94], and the BOSS survey covering $0.43 < z < 0.7$ [4].

Before combining the CMB, H_0 , and BAO datasets, we check their relative consistency

within the Λ CDM model. We quantify this consistency by calculating the χ^2_{\min} using a reference dataset (e.g., CMB) and comparing it to the χ^2_{\min} obtained using a new dataset (e.g., CMB+ H_0). For example, $\chi^2_{\min, [\text{CMB}+H_0]} - \chi^2_{\min, [\text{CMB}]} = 0.08$. The probability to exceed this $\Delta\chi^2$ given the one new degree of freedom provided by the H_0 measurement is 0.78, corresponding to an effective Gaussian significance of 0.3σ . Using this metric, we find that

- CMB and H_0 differ by 0.3σ .
- CMB and BAO differ by 1.5σ .
- (CMB+BAO) and H_0 differ by 1.8σ .
- (CMB+ H_0) and BAO differ by 2.1σ .

There is some tension between these datasets in the context of the Λ CDM model. This could be evidence for a departure from Λ CDM, a systematic error in one or more of the datasets, or simply a statistical fluctuation. We assume the uncertainties reported for each of the datasets are correct and combine them to produce many of the results presented here.

2.5.5 SPT-only Λ CDM constraints

We begin by examining parameter constraints from the SPT bandpowers alone. The SPT-only parameter constraints provide an independent test of Λ CDM cosmology and allow for consistency checks between the SPT data and other datasets. Because the scalar amplitude Δ_R^2 and the optical depth τ are completely degenerate for the SPT bandpowers, we impose a *WMAP7*-based prior of $\tau = 0.088 \pm 0.015$ for the SPT-only constraints. *Planck* released a significantly lower constraint of $\tau = 0.066 \pm 0.016$ [97]; using this prior instead would increase the SPT-only best-fit values of Δ_R^2 .

We present the constraints on the Λ CDM model from SPT and *WMAP7* data in columns two to four of Table 2.5. As shown in Figure 2.5, the SPT bandpowers (including a prior on

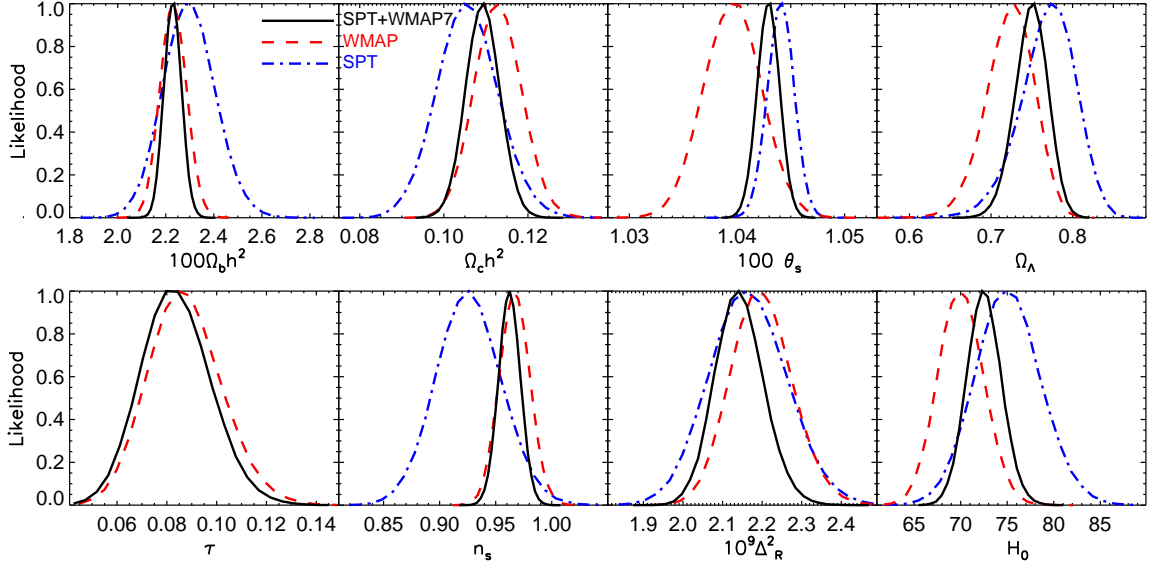


Figure 2.5: The one-dimensional marginalized likelihoods of the six parameters of the Λ CDM model, plus two derived parameters: the dark energy density Ω_Λ and the Hubble constant H_0 . The constraints are shown for the SPT-only (**blue dot-dashed lines**), *WMAP7*-only (**red dashed lines**), and SPT+*WMAP7* (**black solid lines**) datasets. With the exception of τ , the SPT bandpowers constrain the parameters approximately as well as *WMAP7* alone. In particular, the SPT bandpowers measure the angular sound horizon θ_s extremely well because they measure seven acoustic peaks. In the SPT-only constraints, the *WMAP7* measurement of τ has been applied as a prior; because of this we do not plot an SPT-only line on the τ plot.

τ from *WMAP7*) constrain the Λ CDM parameters approximately as well as *WMAP7*. The SPT and *WMAP7* parameter constraints are consistent for all parameters; θ_s changes the most significantly among the five free Λ CDM parameters, moving by 1.5σ and tightening by a factor of 2.2 from *WMAP7* to SPT. The SPT bandpowers measure θ_s extremely well by virtue of the sheer number of acoustic peaks – seven – measured by the SPT bandpowers. The SPT constraint on n_s is broader than the constraint from *WMAP7* due to the fact that *WMAP7* probes a much greater dynamic range of angular scales. Degeneracies with n_s degrade the SPT constraints on Δ_R^2 , the baryon density and, to a lesser extent, the dark matter density.

Table 2.5: Λ CDM Parameter Constraints from the CMB and external datasets

Parameter	<i>WMAP7</i>	SPT ^(a)	CMB (SPT+ <i>WMAP7</i>)	CMB+ H_0	CMB+BAO	CMB+ H_0 +BAO
Baseline parameters						
$100\Omega_b h^2$	2.231 ± 0.055	2.30 ± 0.11	2.229 ± 0.037	2.233 ± 0.035	2.204 ± 0.034	2.214 ± 0.034
$\Omega_c h^2$	0.1128 ± 0.0056	0.1056 ± 0.0072	0.1093 ± 0.0040	0.1083 ± 0.0033	0.1169 ± 0.0020	0.1159 ± 0.0019
$10^9 \Delta_R^2$	2.197 ± 0.077	2.164 ± 0.097	2.142 ± 0.061	2.138 ± 0.062	2.161 ± 0.057	2.160 ± 0.057
n_s	0.967 ± 0.014	0.926 ± 0.029	0.9623 ± 0.0097	0.9638 ± 0.0090	0.9515 ± 0.0082	0.9538 ± 0.0081
$100\theta_s$	1.0396 ± 0.0027	1.0441 ± 0.0012	1.0429 ± 0.0010	1.0430 ± 0.0010	1.04215 ± 0.00098	1.04236 ± 0.00097
τ	0.087 ± 0.015	0.087 ± 0.015	0.083 ± 0.014	0.084 ± 0.014	0.076 ± 0.012	0.077 ± 0.013
Derived parameters ^(b)						
Ω_Λ	0.724 ± 0.029	0.772 ± 0.033	0.750 ± 0.020	0.755 ± 0.016	0.709 ± 0.011	0.7152 ± 0.0098
H_0	70.0 ± 2.4	75.0 ± 3.5	72.5 ± 1.9	73.0 ± 1.5	69.11 ± 0.85	69.62 ± 0.79
σ_8	0.819 ± 0.031	0.772 ± 0.035	0.795 ± 0.022	0.791 ± 0.019	0.827 ± 0.015	0.823 ± 0.015
z_{eq}	3230 ± 130	3080 ± 170	3146 ± 95	3124 ± 78	3323 ± 50	3301 ± 47
$100 \frac{r_s}{D_V}(z = 0.35)$	11.43 ± 0.37	12.15 ± 0.55	11.81 ± 0.29	11.89 ± 0.24	11.28 ± 0.12	11.35 ± 0.12
$100 \frac{r_s}{D_V}(z = 0.57)$	7.58 ± 0.21	7.98 ± 0.31	7.80 ± 0.16	7.84 ± 0.13	7.505 ± 0.068	7.545 ± 0.065

Notes: The constraints on cosmological parameters from the Λ CDM model, given five different combinations of datasets. We report the median of the likelihood distribution and the symmetric 68.3% confidence interval about the mean.

^(a) We impose a *WMAP7*-based prior of $\tau = 0.088 \pm 0.015$ for the SPT-only constraints.

^(b) Derived parameters are calculated from the baseline parameters in CosmoMC. They are defined at the end of Section 2.5.1.

2.5.6 Combined Λ CDM constraints

Next, we present the constraints on the Λ CDM model from the combination of SPT and *WMAP7* data. As previously mentioned, we will refer to the joint SPT+*WMAP7* likelihood as the CMB likelihood. We then extend the discussion to include constraints from CMB data in combination with BAO and/or H_0 data.

We present the CMB constraints on the six Λ CDM parameters in the fourth column of Table 2.5. Adding SPT bandpowers to the *WMAP7* data tightens these parameter constraints considerably relative to *WMAP7* alone. Of these parameters, the constraint on θ_s sees the largest improvement; adding SPT data decreases the uncertainty on θ_s by a factor of 2.70 relative to *WMAP7* alone. Constraints on $\Omega_b h^2$, $\Omega_c h^2$, and Ω_Λ tighten by factors of 1.49, 1.40, and 1.45, respectively. For comparison, the addition of the K11 bandpowers to *WMAP7* led to improvements of 1.33, 1.16, and 1.11, respectively. Finally, the constraint on the scalar spectral index tightens by a factor of 1.44 to give $n_s < 1.0$ at 3.9σ .

The preferred values for $\Omega_b h^2$ and $\Omega_c h^2$ for *WMAP7* do not shift significantly with the addition of the SPT data and, therefore, neither does the sound horizon, r_s , which depends only on these parameters in the Λ CDM model. Thus the shift in $\theta_s = r_s/D_A$, driven by the SPT acoustic peak locations, must lead to a shift in D_A . Shifting D_A requires shifting Ω_Λ (or, equivalently, H_0). This shift in Ω_Λ and H_0 can be seen in Figure 2.5.

We explore how the SPT+*WMAP7* constraints on the Λ CDM model change if different ℓ -ranges of the SPT data are used in Section 2.5.9.

We show the parameter constraints after adding the H_0 and/or BAO data to the CMB data in the last three columns of Table 2.5. Combining the CMB bandpowers with this low-redshift information tightens the constraints on $\Omega_c h^2$ and Ω_Λ by a further factor of 1.2 or 2 for CMB+ H_0 and CMB+BAO, respectively, with smaller but significant improvements to other parameters. Of special note is the constraint on the scalar spectral index which tightens to $n_s = 0.9638 \pm 0.0090$ for the CMB+ H_0 dataset, 0.9515 ± 0.0082 for the CMB+BAO dataset, and 0.9538 ± 0.0081 for the CMB+ H_0 +BAO dataset. These constraints correspond to a

preference for $n_s < 1$ at 4.0σ , 6.1σ , and 5.9σ respectively, for these three data combinations. This is the most significant reported measurement of $n_s \neq 1$ to date. See Section 2.5.12 for a more detailed discussion of constraints on n_s .

2.5.7 Consistency of Λ CDM constraints

Comparing the best-fit cosmological model with K11, all Λ CDM parameters are consistent at $< 1\sigma$ with the exception of θ_s , which shifts up by 1.0σ . It is not surprising that the most significant shift is seen in θ_s ; of the six Λ CDM parameters, SPT data has the strongest effect on the θ_s constraint, as can be seen in Figure 2.5. Thus the results in this chapter are consistent with those from K11.

The σ_8 constraints presented here are consistent with previous measurements. The SPT-only and *WMAP7*-only values are consistent at $\sim 1\sigma$, with the SPT data preferring a lower value. The ACT+*WMAP7* constraint, 0.813 ± 0.028 [39], is consistent with that from SPT+*WMAP7*, though we note that the *WMAP7* data are used in both. The *Planck* data prefer a higher value of $\sigma_8 = 0.829 \pm 0.015$ [97]; this is a 1.2σ shift from the SPT+*WMAP7* constraint and consistent with the constraint that includes BAO and H_0 measurements. Comparing to X-ray measurements of cluster abundance, we re-scale the σ_8 constraint from [135] to the SPT+*WMAP7* value of Ω_M to find $\sigma_8 = 0.813 \pm 0.027$, which is again consistent with our measured values. Optical and SZ-based surveys give comparable and consistent constraints, for example, [109] and [107]. Finally, SPT gravitational lensing measurements are consistent; [131] found $\sigma_8 = 0.810 \pm 0.026$ (*WMAP7*+SPT_{Lensing}). Further discussion of σ_8 constraints, particularly in the context of the Λ CDM + Σm_ν model, can be found in H14.

2.5.8 Physical origin of SPT constraints on Λ CDM

In this section, we discuss the physical origin of the SPT constraints on the matter and baryon density in the Λ CDM model. This section expands on the discussion presented in

the introduction.

The *WMAP7* constraint on the matter density $\omega_m \equiv \Omega_m h^2$ comes from differences in the acoustic oscillations during the radiation-dominated and matter-dominated eras. Modes that enter the horizon during the radiation-dominated era receive a boost to their amplitudes from the decay of the gravitational potential that occurs during their first compression into potential wells. For density fluctuations to maintain a constant gravitational potential in an expanding universe, the density fluctuations must grow unimpeded by any pressure. Photons in the primordial plasma provide pressure, slowing the growth of density fluctuations, and leading to a decaying gravitational potential. The decay boosts the oscillation amplitude since photons gain more energy during their compression into the initially larger potential well than they lose during the expansion out of the much reduced potential well. Modes that enter the horizon during matter domination receive no such boost, since the potential is predominantly sourced by pressure-less dark matter. This difference in oscillation amplitudes allows us to determine the angular scale θ_{eq} separating modes that entered the horizon during radiation domination from those that entered during matter domination. θ_{eq} can then be related to the redshift of matter-radiation equality, z_{eq} . The radiation energy density is completely specified in Λ CDM by the well-measured CMB blackbody temperature today and assumptions about neutrino production. Thus the measurement of z_{eq} corresponds to a determination of ω_m through the relation $1 + z_{\text{eq}} = \omega_m / \omega_{\text{rad}}$.

The SPT bandpowers probe angular scales corresponding to modes that entered the horizon during the radiation-dominated era; that transition occurs around $\ell_{\text{eq}} = \pi / \theta_{\text{eq}} \simeq 434$. The SPT bandpowers are thus largely insensitive to the matter density through the mechanism described above. To confirm this, we removed the largest scales measured by the SPT bandpowers (third peak, $\ell < 1000$) and find only a minimal (5%) degradation in the SPT-only constraint on ω_m . Instead, the SPT bandpowers are sensitive to the amplitude of gravitational lensing which in turn depends on ω_m . Gravitational lensing is discussed in section 2.5.10 and chapter 3. Briefly, gravitational lensing smooths the acoustic peaks of the

CMB power spectrum. Increased ω_m increases the amplitude of the lensing power spectrum. In order to support the claim that the SPT bandpowers are sensitive to ω_m through their sensitivity to amplitude of the lensing spectrum, we remove the lensing information by rescaling the lensing power spectrum $C_\ell^{\phi\phi}$ by a free parameter A_L , defined by:

$$C_\ell^{\phi\phi} \rightarrow A_L C_\ell^{\phi\phi}. \quad (2.17)$$

Marginalizing over A_L doubles the uncertainty on ω_m , degrading the constraint from $\omega_m = 0.1286 \pm 0.0071$ to $\omega_m = 0.129 \pm 0.013$. In the combined SPT+*WMAP7* dataset, ω_m is still constrained primarily by its effect on θ_{eq} .

The *WMAP7* constraint on the baryon density $\omega_b \equiv \Omega_b h^2$ comes primarily from the relative heights of the even and odd acoustic peaks. In contrast to dark matter, baryons interact with photons, changing the primordial plasma pressure. Baryons add mass to the compression into potential wells (odd peaks), but do not enhance the rarefaction onto potential hills (even peaks). Increasing the baryon density thus raises the odd peaks relative to the even peaks.

The SPT constraint on the baryon density is primarily derived from the same peak asymmetry. Although all of the angular scales measured by SPT entered the horizon during the radiation-dominated era, the height of the third acoustic peak is still sensitive to this effect; Increasing ω_b at fixed z_{eq} and θ_s increases the height of the third peak relative to higher peaks. We support this claim by removing the SPT bandpowers over the third peak ($\ell < 1000$); the resulting SPT-only constraint on ω_b degrades by nearly a factor of 2 from $\omega_b = 0.0230 \pm 0.0011$ to $\omega_b = 0.0236 \pm 0.0020$.

The damping scale provides a second constraint on the baryon density from the SPT data. The diffusion of photons through the primordial plasma is described by the diffusion length r_d , the root mean squared comoving distance a photon has traveled up to the epoch

of decoupling between photons and baryons. The diffusion length is given approximately by

$$r_d^2 = \pi^2 \int_0^{a_*} \frac{da}{a^3 \sigma_T n_e H} \left[\frac{R^2 + \frac{16}{15}(1+R)}{6(1+R^2)} \right], \quad (2.18)$$

where a_* is the scale factor at decoupling, n_e is the number density of free electrons, σ_T is the Thompson cross-section of electrons, and $R = 3\rho_b/(4\rho_\gamma)$. The factor in the brackets is due to the dependence of Thompson scattering on direction and polarization [65, 139]. The diffusion length depends on ω_m through the number density of free electrons, $n_e(z) \propto X_e(z)\omega_b(1 - Y_p)$, where $X_e(z)$ is the fraction of Hydrogen atoms that are ionized and Y_p is the primordial fraction of baryonic mass in helium.

We test the importance of the damping scale information for constraining the baryon density from SPT data by introducing Y_p as a free parameter. For fixed ω_b , varying Y_p affects only the free electron density, and thus the damping scale. We allow Y_p to vary freely, and find that the uncertainty of ω_b increases only slightly from 0.0011 to 0.0013. We conclude that the SPT data are sensitive to the baryon density primarily through its effect on the third acoustic peak.

The SPT constraints on the other Λ CDM parameters (θ_s , n_s , and Δ_R^2) come from similar physical mechanisms to the *WMAP7* constraints, which are discussed in section 1.0.3.

We note that in the combined SPT+*WMAP7* dataset, the data prefer slightly less power at higher multipoles relative to the Λ CDM model which best fits the large-scale data at $\ell < 1000$. In the context of the Λ CDM model, this effect is manifested as a downward shift in n_s between *WMAP7*. The implications of this trend in extensions to the Λ CDM model were explored in detail in H14.

2.5.9 Dependence of SPT constraints on multipole range

As discussed in Section 2.5.6 and shown in Figure 2.5, the Λ CDM constraints tighten and shift from the *WMAP7* to the SPT+*WMAP7* dataset. We explore how different ℓ -ranges

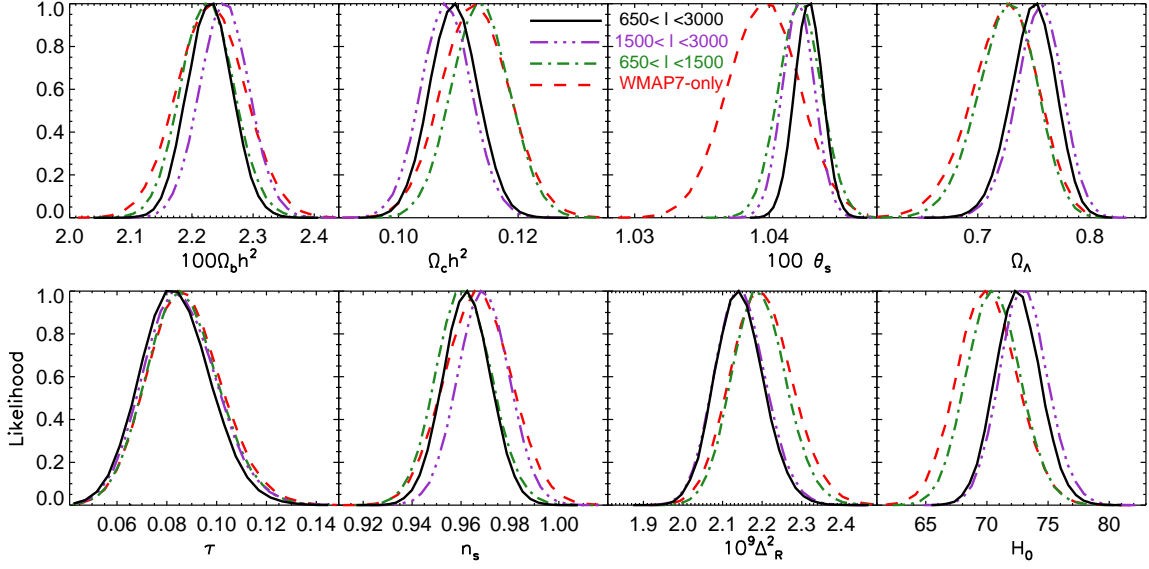


Figure 2.6: Same Λ CDM-model parameters as Figure 2.5, except showing the effect of including the SPT bandpowers over sub-sets of the ℓ -range. The constraints for *WMAP7*-only are shown (**red dashed lines**). Using the SPT+*WMAP7* dataset, the constraints are shown from the full ℓ -range of SPT data (**black solid lines**), from the high- ℓ range $1500 < \ell_{SPT} < 3000$ (**purple dot-dot-dashed lines**), and from the low- ℓ range $650 < \ell_{SPT} < 1500$ (**green dot-dashed lines**).

of the SPT data drive these changes in Figure 2.6. The shifts in $\Omega_c h^2$ and Ω_Λ (or H_0) are driven primarily by the bandpowers at higher multipoles, above $\ell = 1500$. As discussed in H14, this preference is largely driven by the sensitivity of the SPT data to gravitational lensing in the high- ℓ acoustic peaks. On the other hand, n_s is largely constrained by the lower multipoles; the bandpowers at higher multipoles prefer slightly higher values of n_s . The SPT data prefer higher values of θ_s than the *WMAP7* data; each of the sub-ranges pull θ_s above the WMAP value, but only the constraining power of the full dataset pulls θ_s up to the SPT+*WMAP7* value.

2.5.10 Gravitational Lensing

As CMB photons travel from the surface of last scattering to the Earth, their paths are deflected by gravitational interactions with intervening matter. This gravitational lensing

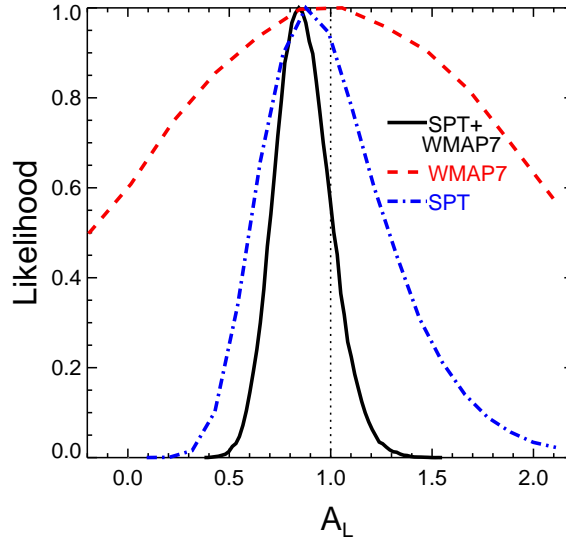


Figure 2.7: The SPT bandpowers allow a significant detection of gravitational lensing through the effective smoothing of the acoustic peaks. Here, we show the one-dimensional likelihood function for A_L , a rescaling parameter for the gravitational lensing potential power spectrum ($C_\ell^{\phi\phi} \rightarrow A_L C_\ell^{\phi\phi}$). The SPT+*WMAP7* data lead to a 8.1σ detection of CMB lensing (this was the most significant detection at the time of publication in [129]).

encodes information about the distribution of matter along the line of sight, providing a probe of the distance scale and growth of structure at intermediate redshifts ($0.1 \lesssim z \lesssim 5$). Lensing distorts the CMB anisotropy by shifting the apparent position of CMB photons on the sky, with typical deflection angles of 2.5 arcminutes which are coherent over degree scales. This process mixes power between multipoles in the CMB temperature power spectrum, which smooths the acoustic peak structure and increases the power in the damping tail at small angular scales (see [81] for a review).

The Λ CDM model already includes the effects of gravitational lensing. To quantify the sensitivity of the SPT bandpowers to gravitational lensing, we extend the Λ CDM model to include one additional free parameter, A_L [21], which rescales the lensing potential power spectrum, $C_\ell^{\phi\phi}$, according to

$$C_\ell^{\phi\phi} \rightarrow A_L C_\ell^{\phi\phi}. \quad (2.19)$$

We re-calculate $C_\ell^{\phi\phi}$ in a cosmology-dependent manner at each point in the MCMC. In effect, the A_L parameter modulates the amplitude of gravitational lensing. Setting $A_L = 1$ corresponds to the standard theoretical prediction and recovers the standard Λ CDM model, while setting $A_L = 0$ corresponds to no gravitational lensing. In the parameter fits, the range of A_L is allowed to extend well above 1 and below 0.

The first detection of gravitational lensing in the CMB used lensing-galaxy cross-correlations [121, 55], and subsequent papers using this technique have achieved higher signal-to-noise detections [15, 117].

The impact of lensing on the CMB power spectrum has been detected in numerous experiments, including combinations of *WMAP* with ACBAR [105], *WMAP* with ACT [31], *WMAP* with SPT (K11), and *Planck* [100]. Using this effect, [31] found $A_L = 1.3_{-0.5}^{+0.5}$ at 68% confidence. K11 found that the constraint on $A^{0.65}$ had the most Gaussian shape and thus reported $A_L^{0.65} = 0.94 \pm 0.15$, a $\sim 5\sigma$ detection of lensing.

CMB lensing has also been detected through the CMB temperature four-point function. [32] used ACT data to measure¹⁰ $A_L^{\text{ML}} = 1.16 \pm 0.29$. In [131], the SPT four-point analysis was applied to a subset of the data used in this work to measure $A_L = 0.90 \pm 0.19$, which was previously the most significant detection of CMB lensing to date, ruling out no lensing at 6.3σ . See Chapter 3 for more discussion of CMB lensing measurements and the four-point estimator.

We determine the significance of the observed CMB lensing by constraining A_L with the measured CMB power spectrum. The significance of the detection is quantified by calculating the probability for $A_L \leq 0$, $P(A_L \leq 0)$. As $A_L = 0$ is far out in the tail of the likelihood distribution of this parameter, we use high-temperature MCMC's chains to estimate $P(A_L \leq 0)$. Using SPT data only, we measure $P^{\{SPT\}}(A_L \leq 0) < 1.3 \times 10^{-9}$, the

10. In [32], A_L is calculated as the best-fit amplitude to the lensing potential in the cosmological model with the maximum likelihood Λ CDM parameters. This is in contrast to what was done for the CMB temperature power spectrum measurements of A_L , where constraints on A_L have been marginalized over cosmological parameters. The corresponding maximum likelihood measure from [131] is $A_L^{\text{ML}} = 0.86 \pm 0.16$.

equivalent of a 5.9σ preference for $A_L > 0$ in a Gaussian distribution. For SPT+*WMAP*7 we measure

$$P^{\{CMB\}}(A_L \leq 0) \leq 2.4 \times 10^{-16}, \quad (2.20)$$

which corresponds to a 8.1σ detection of lensing in a Gaussian distribution.

Next, we report constraints on A_L . Using SPT+*WMAP*7 data we find

$$A_L = 0.86^{+0.15(+0.30)}_{-0.13(-0.25)}, \quad (2.21)$$

where asymmetric 1σ (68.3%) and 2σ (95.5%) errors are shown. The observed lensing amplitude is consistent at 1σ with theoretical predictions in the Λ CDM model.

2.5.11 Mean Curvature of the Observable universe

The low-redshift information imprinted on the CMB by gravitational lensing, along with the other information in the CMB anisotropy power spectrum, enables the placement of tight constraints on the mean curvature of the observable Universe. The magnitude of the mean curvature today can be parametrized by $\Omega_k \equiv -K/H_0^2$ where $\sqrt{1/|K|}$ is the length scale over which departures from Euclidean geometry become important. Inflationary models generically predict $|\Omega_k| \lesssim 10^{-5}$ [e.g., 73]; thus a significant measurement of $\Omega_k \neq 0$ would challenge our standard picture of the very early universe. A positive value for Ω_k ($K < 0$) could be obtained by the nucleation of a bubble of lower vacuum energy in a surrounding medium with higher vacuum energy followed by a short period of inflation [18]. A determination that Ω_k is negative with high statistical significance would be very interesting; such a detection would be difficult to understand in the theoretical framework of inflation, challenge the string theory landscape picture, and rule out the de Sitter equilibrium cosmology of [2].

Absent lensing effects, one can leave the CMB power spectrum unchanged while simulta-

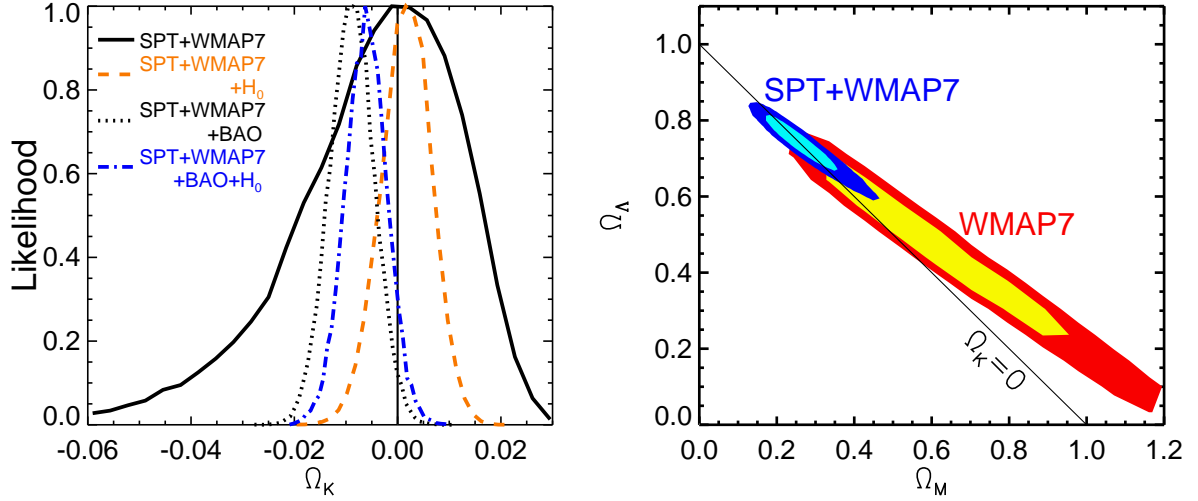


Figure 2.8: The low-redshift information imprinted on the CMB by gravitational lensing, along with the other information in the CMB anisotropy power spectrum, enables the placement of tight constraints on the mean curvature of the observable Universe. The addition of low-redshift probes further tighten CMB-only constraints on the mean curvature. **Left panel:** The one-dimensional marginalized constraints on Ω_k from SPT+WMAP7 (black solid line), SPT+WMAP7+ H_0 (orange dashed line), SPT+WMAP7+BAO (black dotted line), and SPT+WMAP7+BAO+ H_0 (blue dot-dashed line). The SPT+WMAP7 datasets measure the mean curvature of the observable universe to a precision of $\sim 1.5\%$, while combining SPT, WMAP7, and either H_0 or BAO data reduces the uncertainty by a factor of ~ 3 . **Right panel:** The two-dimensional constraints on Ω_M and Ω_Λ from the SPT+WMAP7 data alone. The SPT+WMAP7 data rule out $\Omega_\Lambda = 0$ at 5.4σ .

neously varying Ω_k and Ω_Λ in a way that keeps the distance to last scattering fixed [16, 141].¹¹ Historically the CMB data placed very coarse constraints on Ω_k , with finer constraints only possible from the addition of other data sensitive to Ω_k and Ω_Λ such as H_0 measurements and determinations of Ω_m [e.g., 38] from, for example, the baryon fraction in clusters of galaxies [136].

The sensitivity of the CMB to low-redshift information through gravitational lensing makes it possible to constrain the mean curvature of the observable universe, and thus the cosmological constant, using the CMB alone. The lensing amplitude is sensitive to the distance and growth of structure at intermediate redshifts ($0.5 \lesssim z \lesssim 4$). These observables are, in turn, sensitive to curvature, dark energy, and neutrino masses, as discussed in H14. The recent detections of CMB lensing have measured an amplitude that is consistent with $\Omega_K \sim 0$ and $\Omega_\Lambda \sim 0.7$ [31, 32, 118, 69, 131]. Simply put, the strength of CMB lensing in a universe with no dark energy and positive mean curvature would be much larger than that observed (see e.g., [118]).

Using the SPT+*WMAP7* bandpowers, we measure the mean curvature of the observable universe using only the CMB:

$$\Omega_k = -0.003^{+0.014}_{-0.018}. \quad (2.22)$$

This result tightens curvature constraints over *WMAP7* combined with low-redshift probes by $\sim 20\%$. This constraint is consistent with zero mean curvature, and corresponds to a dark energy density of $\Omega_\Lambda = 0.740^{+0.045}_{-0.054}$ and Hubble constant, $H_0 = 70.9^{+9.2}_{-8.0}$ (km s⁻¹ Mpc⁻¹). This measurement rules out $\Omega_\Lambda = 0$ at 5.4σ using the CMB alone. The right panel of Figure 2.8 shows the corresponding two-dimensional marginalized constraints on Ω_M and Ω_Λ . We have confirmed that the strength of this constraint relies on the lensing signal; allowing A_L to vary freely causes the curvature constraint to degrade dramatically.

11. There is an exception to this at very large scales due to the late ISW effect, but sample variance makes these changes unobservably small in the CMB power spectrum.

Table 2.6: Constraints on n_s and r from CMB and external datasets

Model	Parameter	CMB (SPT+ <i>WMAP</i> 7)	CMB+ H_0	CMB+BAO	CMB+ H_0 +BAO
Λ CDM	n_s	0.9623 ± 0.0097	0.9638 ± 0.0090	0.9515 ± 0.0082	0.9538 ± 0.0081
Λ CDM+ r	n_s	0.969 ± 0.011	0.9702 ± 0.0097	0.9553 ± 0.0084	0.9577 ± 0.0084
	r (95% C.L.)	< 0.18	< 0.18	< 0.11	< 0.11

CMB lensing enables an independent constraint on curvature, although the most powerful curvature constraints still come from combining CMB data with other low-redshift probes (e.g., H_0 , BAO). The curvature constraint using CMB+ H_0 data is $\Omega_k = 0.0018 \pm 0.0048$, while the constraint using CMB+BAO data is $\Omega_k = -0.0089 \pm 0.0043$. The tightest constraint on the mean curvature that we consider comes from combining the CMB, H_0 , and BAO datasets:

$$\Omega_k = -0.0059 \pm 0.0040. \quad (2.23)$$

While the CMB+BAO constraint shows a 2.0σ preference for $\Omega_k < 0$, the significance of this preference decreases as more data are added. The tightest constraint, coming from CMB+ H_0 +BAO, is consistent with zero mean curvature at 1.5σ . These results are summarized in Figure 2.8. As discussed by H14, other extensions of Λ CDM can also explain the data (e.g., allowing for both non-zero mean curvature and a dark energy equation of state $w \neq -1$), thus these constraints are significantly degraded when multiple extensions to Λ CDM are simultaneously considered.

2.5.12 Inflation

Cosmic inflation is an accelerated expansion in the early universe [50, 85, 3] that generically leads to a universe with nearly zero mean curvature and a nearly scale-invariant spectrum of “initial” density perturbations [89, 53, 125, 51, 7] that evolved to produce the observed spectrum of CMB anisotropies. Models of inflation compatible with current data generally

predict, over the range of observable scales, scalar and tensor perturbations well characterized by a power law in wavenumber k ,

$$\Delta_R^2(k) = \Delta_R^2(k_0) \left(\frac{k}{k_0} \right)^{n_s-1} \quad (2.24)$$

$$\Delta_h^2(k) = \Delta_h^2(k_0) \left(\frac{k}{k_0} \right)^{n_t}. \quad (2.25)$$

Here $\Delta_h^2(k_0)$ is the amplitude of tensor (gravitational wave) perturbations specified at the same pivot scale, with scale dependence set by n_t . The amplitude of the tensor perturbation spectrum is expressed in terms of the tensor-to-scalar ratio

$$r = \left. \frac{\Delta_h^2(k)}{\Delta_R^2(k)} \right|_{k=0.002 \text{ Mpc}^{-1}}. \quad (2.26)$$

For single-field models in slow-roll inflation, n_t and r are related by a consistency equation [28, 72]:

$$n_t = -r/8. \quad (2.27)$$

The tensor and scalar perturbations predicted by such models of inflation can thus be characterized by the three parameters n_s , $\Delta_R^2(k_0)$, and r .

In the following, we first consider constraints on n_s assuming $r = 0$, and then on both n_s and r . We then compare the constraints in the n_s - r plane to predictions of inflationary models. Constraints on the scale dependence of the spectral index ($dn_s/d \ln k$) are considered in H14.

Constraints on the Scalar Spectral Index

Inflation is a nearly time-translation invariant state, however this invariance must be broken for inflation to eventually come to an end. The wavelength of perturbations depends solely on the time that they were produced, thus a time-translation invariant universe would produce

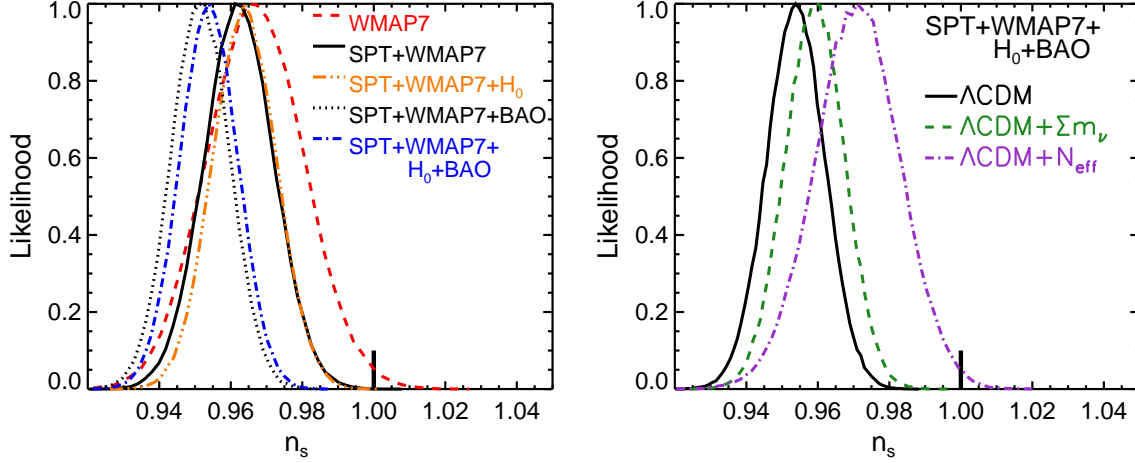


Figure 2.9: The data strongly prefer departures from a scale invariant primordial power spectrum ($n_s < 1$), as predicted by inflation. **Left panel:** The marginalized one-dimensional constraints on n_s for the standard Λ CDM model (with $r = 0$) using several datasets. SPT data tightens the constraint on n_s relative to *WMAP7* alone. Adding BAO data further tightens this constraint and leads to a preference for lower values of n_s , while adding H_0 has little effect. **Right panel:** The one-dimensional marginalized constraints on n_s from the SPT+*WMAP7*+ H_0 +BAO dataset given three different models. Plotted are Λ CDM (**black solid line**), Λ CDM + Σm_ν (**purple dashed line**) as a typical case for extensions affecting the late-time universe, and Λ CDM + N_{eff} (**green dot-dashed line**) as a typical case for extensions affecting the Silk damping scale. Of the extensions considered here, only those that affect the damping tail – in this case by varying neutrino species – causes noticeable movement towards $n_s = 1$. We note that in all cases the data robustly prefer a scale-dependent spectrum with $n_s < 1$.

scale-invariant perturbations ($n_s = 1$).¹² The prediction that inflation should be nearly, but not fully, time-translation invariant gives rise to the prediction that n_s should deviate slightly from unity [37]. This prediction is consistent across most single-field, slow-roll inflation models.

Because of the special status of $n_s = 1$, and because we generally expect a departure from $n_s = 1$ for inflationary models, detecting this departure is of great interest. K11 combined data from SPT and *WMAP7* to measure a 3.0σ preference for $n_s < 1$ in a Λ CDM model, with $n_s = 0.966 \pm 0.011$. We show our constraints on n_s for the Λ CDM model from several combined datasets in the left panel of Figure 2.9. All datasets strongly prefer $n_s < 1$.

Using SPT+*WMAP7* data, we find

$$n_s = 0.9623 \pm 0.0097. \quad (2.28)$$

For this dataset, we find $P(n_s > 1) = 4 \times 10^{-5}$, a 3.9σ departure from $n_s = 1$; $n_s < 1$ is strongly favored.

Including BAO data substantially shifts and tightens the constraints on n_s , as can be seen in Figure 2.9. The BAO distance measure r_s/D_V depends on Ω_Λ , breaking the partial degeneracy between Ω_Λ and n_s in the CMB power spectrum. The BAO preference for lower Ω_Λ pulls the central value of n_s down to $n_s = 0.9515 \pm 0.0082$. Using a high-temperature MCMC, we measure the probability for n_s to exceed one to be 1.1×10^{-9} , corresponding to a 6.0σ detection of $n_s < 1$.

Including H_0 data has a smaller effect on the n_s constraint than BAO, slightly disfavoring low- n_s values as seen in Figure 2.9. The mechanism for the improvement is the same as for BAO, however, the CMB and H_0 datasets individually prefer similar values of Ω_Λ . Thus the two datasets tighten the n_s constraint around the CMB-only value, leading to $n_s =$

12. Scale invariance here means that the contribution to the rms density fluctuation from a logarithmic interval in k , at the time when $k = aH$, is independent of k . Here $a(t)$ is the scale factor and $H \equiv \dot{a}/a$ is the Hubble parameter.

0.9638 ± 0.0090 . Using the combined CMB+ H_0 dataset, we measure the probability for n_s to exceed one to be 3.1×10^{-5} , corresponding to a 4.0σ preference for $n_s < 1$.

As expected, combining CMB with both BAO and H_0 data nudges the constraint on n_s up slightly from the CMB+BAO constraint to $n_s = 0.9538 \pm 0.0081$, thus weakening the preference for $n_s < 1$ slightly from 6.0 to 5.7σ .

In summary, regardless of which datasets we use, the data strongly prefer $n_s < 1$ in the Λ CDM model.

The importance of detecting a departure from scale invariance leads us to review our modeling assumptions. Specifically, are there extensions to the standard Λ CDM model that could reconcile the data with a scale-invariant spectrum, $n_s = 1$? We answer this question by calculating the n_s constraints from the CMB+ H_0 +BAO dataset for several physically motivated Λ CDM model extensions.

We consider two classes of model extensions: those that can affect the slope of the CMB damping tail, and those that cannot. As a representative case of the first class of extensions, we consider Λ CDM+ N_{eff} , in which the number of relativistic species is allowed to vary. As an example of the second class of extensions, we consider massive neutrinos Λ CDM+ Σm_ν (with N_{eff} fixed at its fiducial value of 3.046). These example extensions as well as several others are explored in considerable detail in H14.

Of the extensions considered, only models that can affect the slope of the damping tail significantly increase the likelihood of $n_s = 1$. The results of this test are displayed in the right panel of Figure 2.9, where we show the marginalized constraints on n_s from the CMB+BAO+ H_0 dataset. Even the N_{eff} extension does a poor job reconciling the data with a scale-invariant spectrum; the cumulative probability for $n_s > 1$ is 6.1×10^{-3} , constraining n_s to be less than one at 2.5σ . The preferred value for N_{eff} is far greater than the nominal value of 3.046 in the limited allowed parameter space.

We conclude that the data robustly prefer a scale-dependent spectrum with $n_s < 1$.

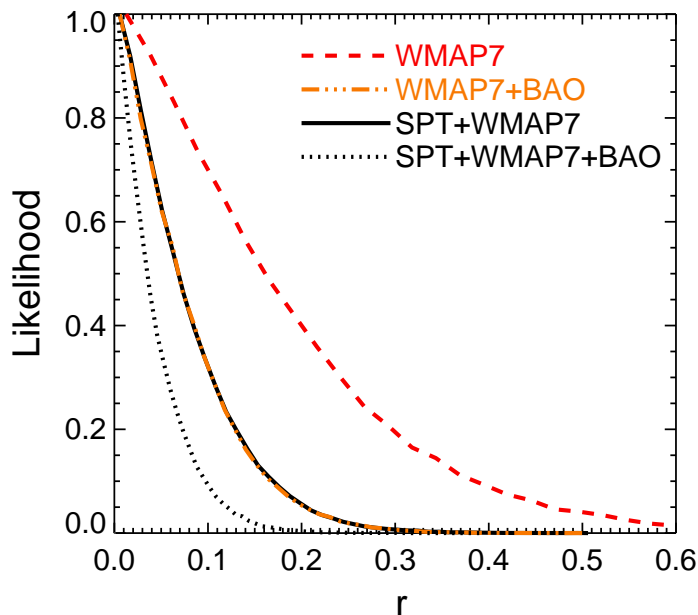


Figure 2.10: This figure highlights the contributions of the SPT data to constraints on the tensor-to-scalar ratio, r . We show four datasets: *WMAP7* (**red dashed line**), *WMAP7*+BAO (**orange dot-dashed line**), SPT+*WMAP7* (**black solid line**), and SPT+*WMAP7*+BAO (**black dotted line**). Note that the *WMAP7*+BAO and SPT+*WMAP7* likelihood functions are nearly identical. SPT data tightens the r constraint significantly, regardless of whether BAO data are included. While adding low-redshift H_0 measurements has minimal effect on the constraints on r (not shown), adding low-redshift information from BAO tightens constraints on r considerably. SPT+*WMAP7* constrains $r < 0.18$ (95% C.L.), while adding low-redshift BAO measurements tightens the constraint to $r < 0.11$ (95% C.L.).

Constraints on Tensor Perturbations

The last inflationary parameter we consider is the tensor-to-scalar ratio r . Because r is related to the energy scale of inflation,¹³ a detection of r would provide an extremely interesting window onto the early universe. We first consider the marginalized constraints on r for the Λ CDM+ r model, shown in Table 2.6 and Figure 2.10, then move on to a comparison with inflationary models in the n_s - r plane in Section 2.5.12 and Figure 2.11.

One can think of the r measurement in the following way. The CMB power spectrum is

13. The tensor-to-scalar ratio r is proportional to the inflaton potential $V(\phi)$ and the energy scale of inflation is proportional to $V(\phi)^{1/4}$ [71, 8].

first measured at $\ell \gtrsim 60$ (where tensor perturbations are negligible) to determine the Λ CDM model parameters, thus determining the scalar contributions to the power spectrum. This scalar-only spectrum is then extrapolated to low ℓ ; any excess power observed is due to tensor perturbations. In this way, although the SPT data presented here do not directly measure power that could be from gravitational waves, by pinning down other model parameters, the extrapolation of the scalar power to large scales is more precise.

Even with the parameters that determine the scalar power spectrum perfectly known, there would still be significant uncertainty in the value of r due to cosmic variance. [74] showed that for different realizations of a universe where $r = 0$, 50% of cosmic variance limited full sky temperature surveys will be able to place a limit of $r < 0.1$ at 95% confidence. As we will see, the results we present here approach that limit.

WMAP7 data alone have been used to constrain $r < 0.36$ at 95% confidence in the Λ CDM+ r model [77]. Prior to the current SPT analysis, the tightest published constraint on r was reported by [110], who used the combination of datasets from BOSS-CMASS, *WMAP7*, and K11 to constrain $r < 0.16$ at 95% confidence.

The bandpowers presented here lead to a significant reduction in the upper limit on r . These measurements are summarized in Table 2.6. As shown in Figure 2.10, SPT bandpowers tighten the constraint on r regardless of whether low-redshift information from BAO or H_0 is included. Using the CMB datasets, we measure

$$r < 0.18 \text{ (95\% C.L.)} . \tag{2.29}$$

This limit remains unchanged for the CMB+ H_0 datasets, while from the CMB+BAO datasets we measure $r < 0.11$ (95% C.L.). As with constraints on n_s , the improvement with the addition of BAO comes from the improved BAO constraints on Ω_Λ breaking a partial three-way degeneracy between Ω_Λ , n_s , and r . In contrast, adding in the H_0 measurement to CMB data does not significantly tighten the CMB-only result because the H_0 measurement sharpens

up the Ω_Λ distribution around the values that allow for larger r . It is worth noting that the SPT bandpowers tighten the constraint on r even in the presence of BAO data; this can be seen in the tighter r constraint from the *WMAP7*+BAO to the SPT+*WMAP7*+BAO datasets in Figure 2.10.

Using the combination of the CMB+BAO+ H_0 datasets, we measure

$$r < 0.11 \text{ (95\% C.L.)}; \quad (2.30)$$

this limit is unchanged from the CMB+BAO constraint. The H_0 and BAO data pull in opposite directions on the CMB-only data in the $r_s/D_V - H_0$ plane, however the statistical weight of the BAO measurements dominate the constraint in the combined dataset.

With the addition of low-redshift information from the BAO measurement, the constraints on tensor perturbations approach the theoretical limit of what can be achieved with temperature anisotropy alone. With the combination of these data, the cosmological parameters controlling the scalar perturbations are now sufficiently well known that they do not significantly degrade the limit on r . This is evident in Figure 2.11, where adding BAO removes most of the degeneracy between n_s and r . Further improvements now await precision B -mode CMB polarization observations [114, 66]. The current upper limit on r from B -modes is $r = 0.12$ (95% C.L.) from a combination of data from three experiments: BICEP2, the Keck Array, and *Planck* [11]¹⁴.

Implications for Models of Inflation

We now turn to a comparison of model predictions with data constraints in the n_s - r plane. This comparison is illustrated in Figure 2.11, where we show the two-dimensional marginalized constraints from three combinations of data with predictions from simple models of inflation over-plotted. First, we note that the confidence contours for the CMB-only case in

14. Note: at the time of publication, the lowest upper limit on r from B -modes was $r < 0.7$ (95% C.L.) from the BICEP experiment [23].

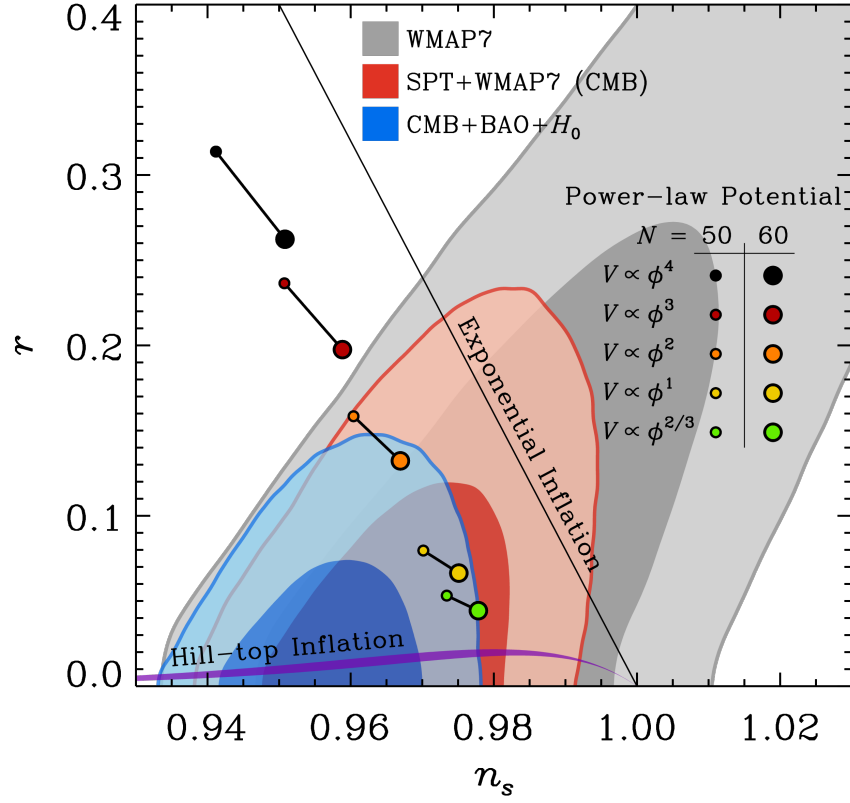


Figure 2.11: We compare the constraints on the $\Lambda\text{CDM}+r$ model with predictions from models of inflation in the $n_s - r$ plane. We show the two-dimensional constraints on r and n_s as colored contours at the 68% and 95% confidence levels for three datasets: *WMAP7* (**grey contours**), CMB (**red contours**), and CMB+ H_0 +BAO (**blue contours**). Adding the SPT bandpowers partially breaks the degeneracy between n_s and r in the *WMAP7* constraint, which can be seen clearly moving between the grey and red contours. Plotted over the constraint contours are predictions for several models of inflation. We restrict our comparison with model predictions to the simplest cases of slow-roll inflation due to a single scalar field as reviewed in [8].

Solid black line: The predictions of exponential inflation ($V(\phi) \propto \exp \left[\sqrt{16\pi\phi^2/(p M_{\text{Pl}}^2)} \right]$) lie on this line. In exponential inflation, increasing p moves the prediction towards the Harrison-Zel'dovich-Peebles point $n_s = 1, r = 0$.

Black lines with colored circles: The predictions of power-law potential inflation models ($V(\phi) \propto (\phi/\mu)^p, p > 0$) for five different values of p lie on the corresponding line. The predictions in the $r - n_s$ plane are a function of N , where N is expected to be in the range $N \in [50, 60]$.

Purple region: This region represents the upper limit on r from large-field hill-top inflation models. The width of the curve represents the uncertainty due to varying $N \in [50, 60]$, but does not take into account effects of higher order terms in the potential which may become important at the end of inflation.

Fig. 2.11 show the expected positive correlation between n_s and r . Essentially, the suppression of large-scale power when increasing n_s can be countered by adding extra large-scale power sourced by tensors. The SPT data disfavor large values of n_s (and hence r), significantly reducing the degeneracy between these two parameters. With BAO data added to SPT+*WMAP*7, the $n_s - r$ correlation nearly disappears. Adding H_0 data has little effect on constraints from the CMB or CMB+BAO datasets, removing only the smallest allowed values of n_s in both cases. As mentioned above, we are approaching the cosmic variance limit for the temperature anisotropy on measuring r – at which point improved knowledge of the six Λ CDM parameters no longer translates into better limits on r .

We restrict the model comparisons to the simplest cases of single-field, slow-roll inflation, as reviewed in [8]. Models can be broadly characterized according to how much the inflaton field ϕ changes from the time perturbations on observably large scales were being produced until the end of inflation; this change in ϕ defined as $\Delta\phi$. Models in which $\Delta\phi$ is larger than the Planck mass (M_{Pl}) are classified as “large-field” models, while those in which $\Delta\phi < M_{\text{Pl}}$ are classified as “small-field” models. The dividing line between the two cases corresponds to $r = 0.01$.

Here we look at large-field inflation models, considering several forms of the inflaton effective potential: large-field power-law potential inflation models ($V(\phi) \propto (\phi/\mu)^p$, $p > 0$), large-field hill-top inflation models ($V(\phi) \propto 1 - (\phi/\mu)^2$), and exponential inflation models ($V(\phi) \propto \exp \left[\sqrt{16\pi\phi^2/(p M_{\text{Pl}}^2)} \right]$).

Large-field power-law potential models have the fewest free parameters, and we discuss them first. Given a choice of p , these models have just one free parameter, and this parameter is highly constrained by the requirement of reproducing the well-known amplitude of the scalar perturbation spectrum. Thus, these models make fairly localized predictions in the $n_s - r$ plane. The uncertainty in these predictions is dominated by the details of the end of inflation which are not specified by $V(\phi)$ but, instead, depend on the coupling of the inflaton field ϕ to other fields. This uncertainty can be captured by the parameter N where e^N gives

the increase in the scale factor between the time when the observable scale leaves the horizon and the end of inflation.¹⁵ Assuming a standard slow-roll inflation scenario,¹⁶ N is expected to lie in the range 50 to 60 [84]. The spread in values is dominated by uncertainty in how much the energy density drops between the end of inflation and reheating, though this range can be extended in either direction by modifications to the standard thermal history. In Figure 2.11 we consider several large-field power-law potential models, each with a different value of p , and indicate the predictions of each model as N varies between 50 and 60.

The $\lambda\phi^4$ ($p = 4$) and $\lambda\phi^3$ ($p = 3$) models were ruled out by earlier data [75, 39], given the expected range of N . These models possibly could have been saved with a non-standard post-inflation thermal history (designed to make N very large, thus moving the prediction towards $r = 0$ and $n_s=1$ in Figure 2.11), but such a maneuver no longer works. The CMB+BAO dataset excludes the $\lambda\phi^4$ model with greater than 95% confidence for all values of N , while the ϕ^3 ($p = 3$) model is excluded with greater than 95% confidence by the CMB or CMB+ H_0 datasets given the expected range of N , and excluded with greater than 95% confidence by the CMB+BAO datasets regardless of N .

While the $m^2\phi^2$ ($p = 2$) model was consistent with previous constraints [69, 110], the current combinations of CMB with BAO data place a tight upper limit on r and disfavor the $m^2\phi^2$ model, which produces predictions that fall at the edge of the 95% confidence contour. This model is allowed by CMB or CMB+ H_0 . Models with smaller values of p are consistent with the data, as shown in Figure 2.11.

The exponential models lead to n_s and r predictions that are independent of scale and therefore independent of N . The predictions, as p varies, form a line in the $n_s - r$ plane. This whole class of models is allowed at 95% confidence for a range of p by the CMB+ H_0 data, and is excluded ($> 95\%$ C.L.) by the CMB+BAO and CMB+ H_0 +BAO data.

15. A note of clarification: N says nothing about the total increase in the scale factor between the beginning and end of inflation, which is expected to be much larger.

16. The assumption here is that inflation stops by the end of slow roll and is followed by the field oscillating in an approximately quadratic potential near the minimum. The universe eventually reheats to a density greater than that during BBN, and then the standard thermal history ensues.

The potential in hill-top models has the shape of symmetry-breaking potentials that drive ϕ away from the origin. The generic form of the hill-top potential is $V(\phi) \propto 1 - (\phi/\mu)^p$. Such models, for a fixed p , have three free parameters: the proportionality constant, μ , and ϕ_{end} . The first two are found in the potential. The third is needed because the potential does not naturally lead to an end to inflation; without making ϕ_{end} explicit, the end of inflation depends either on the details of unspecified higher order terms in the potential or on external physics. The proportionality constant is set by the amplitude of scalar fluctuations Δ_R^2 , while μ , for fixed ϕ_{end} , is constrained by n_s and r . In turn, we take ϕ_{end} to be constrained above by μ , of order the vacuum expectation value of the field.

For $p \leq 2$, hill-top models can have the behavior of large-field models for the range of n_s allowed by the data. The behavior of the $p = 2$ case in the large-field ($\phi_{end} = \mu$) limit is shown as a purple region in Figure 2.11, and is consistent with the data.

Finally, we consider small-field inflation models. Examples of small-field potentials include hill-top potentials with $p > 2$ (for some values of μ), the Coleman-Weinberg potential [26] (with suitably adjusted parameters), and warped D-brane inflation [64]. Because small-field models predict $r \leq 0.01$, the SPT data have no constraining power on these models through limits on r . All of these models are consistent with the data, so long as they are consistent with the limits on n_s .

Constraints on the scale dependence of the spectral index ($dn_s/d \ln k$) are considered in H14.

2.6 Discussion

In this chapter, we have presented a measurement of the CMB temperature power spectrum from 2540 deg² of sky observed with the SPT, which was reported in [129]. These are the first CMB power spectrum results reported for the full SPT-SZ survey, which encompasses three times the area used in previous SPT power spectrum analyses (K11, [107]) The bandpowers cover the third to ninth acoustic peaks ($650 < \ell < 3000$) with sample-variance-limited

precision at $\ell < 2900$. At the time of publication, this measurement represented a significant advance over previous measurements of the damping tail by ACBAR [105], QUaD [17, 45], ACT [32], and SPT [69].

We find the SPT bandpowers are well fit by a spatially flat Λ CDM cosmology with gravitational lensing by large-scale structure. We use this SPT measurement to extend the dynamic range probed by the *WMAP* power spectrum, thus tightening parameter constraints in the six-parameter Λ CDM model. With the exception of the optical depth τ which is constrained by the large-scale polarization data from *WMAP7*, adding the full survey SPT bandpowers significantly improves measurements of all Λ CDM parameters. Most notably, the measurement of the angular sound horizon, θ_s , tightens by a factor of 2.7 due to the number of acoustic peaks detected at high signal-to-noise. Uncertainties on the other four parameters are reduced by a factor of ~ 1.4 . The combination of SPT and *WMAP7* data is used to constrain $n_s < 1$ at 3.9σ .

We examine constraints on three extensions to the Λ CDM model. We first allow for a rescaling of the gravitational lensing potential by a parameter A_L . Using CMB data, we rule out the no-lensing hypothesis ($A_L \leq 0$) at 8.1σ , the most significant detection to date using the CMB alone, and measure a lensing amplitude, $A_L = 0.86^{+0.15(+0.30)}_{-0.13(-0.25)}$ (68% and 95% C.L.), consistent with the Λ CDM expectations. We expect the lensing detection significance to triple in a future analysis of the full SPT-SZ survey using an optimized four-point lensing estimator, similar to the one applied to one fifth of the survey by [131].

Second, we allow non-zero mean curvature of the observable universe. The low-redshift information encoded in the CMB by gravitational lensing helps to improve constraints on the mean curvature of the observable universe for the Λ CDM+ Ω_k model. Using the CMB alone, we measure $\Omega_k = -0.003^{+0.014}_{-0.018}$, which is consistent with a flat universe. Models without dark energy are ruled out at 5.4σ .

Finally, we look at constraints on the amplitude of tensor perturbations. The combination of SPT+WMAP7 is used to constrain the tensor-to-scalar ratio to be $r < 0.18$ with 95%

confidence.

Adding low-redshift probes of H_0 and BAO further tightens these constraints. Combining the CMB and H_0 datasets mildly tightens our parameter constraints, and is fully consistent with the CMB constraints. Combining the CMB and BAO datasets, on the other hand, leads to significant improvements in our parameter constraints. Combining all three datasets produces constraints that lie close to the CMB+BAO constraints; the combination of CMB+ H_0 +BAO is used to constrain $n_s < 1$ at 5.7σ in the Λ CDM model, measure $\Omega_k = -0.0059 \pm 0.0040$ in the Λ CDM+ Ω_k model, and constrain $r < 0.11$ at 95% confidence in the Λ CDM+ r model. This constraint on r approaches the theoretical limit of how well tensor perturbations can be constrained from CMB temperature anisotropy, $r < 0.1$ (95% C.L.). We compare these constraints on n_s and r to the predictions of single-field inflation models and exclude several models with greater than 95% confidence.

There is some tension between the six datasets included in the CMB+BAO+ H_0 combination for a Λ CDM cosmology. However, we assume the uncertainties reported for each of the datasets are correct and combine them to produce many of the results presented here. We refer the reader to H14 for a more detailed discussion of the consistency of the datasets.

In this chapter, we have focused on the amplitude and shape of the primordial power spectrum of scalar and tensor perturbations, as well as the effects of gravitational lensing and curvature. Further cosmological implications of the bandpowers from the full SPT-SZ survey, including constraints on the neutrino masses, the dark energy equation of state, the primordial Helium abundance, and the effective number of neutrino species are explored in H14.

Measurements of the CMB power spectrum continue to improve. Since the publication of these results in [129], the *Planck* satellite has released full-sky measurements of the temperature and polarization power spectra [99, 96] which significantly improves cosmological constraints [100, 97]. Measurements of CMB polarization are now providing new and complementary information from experiments including *Planck*, ACT-Pol, POLARBEAR, and

SPT_{pol}.

CHAPTER 3

CMB GRAVITATIONAL LENSING POTENTIAL POWER SPECTRUM

Gravitational lensing of the CMB has become a powerful observational tool for probing the geometry of the universe and the growth of large-scale structure. CMB photons are deflected by gravitational interactions with matter; these deflections encode information about the geometry of the universe and growth of large-scale structure at late times, providing a way to directly study the distribution of mass in the universe. As a result, measurements of lensing are sensitive to several physical phenomena. In the Λ CDM model at angular scales probed by SPTpol, the CMB lensing potential power spectrum is primarily sensitive to the total matter density¹ Ω_m [95]. Beyond Λ CDM, lensing measurements are sensitive to dark energy and modified gravity scenarios primarily through their effects on structure growth at late times [19]. Finally, lensing measurements are sensitive to the mass of neutrinos [78]. Massive neutrinos affect the energy density (expansion rate) throughout the history of the universe and neutrinos cluster only on scales longer than their free-streaming length, thus suppressing structure on small scales.

The CMB provides a unique source for lensing measurements. First, the CMB is a well-characterized source of light. The CMB anisotropies are well understood theoretically and have been measured to exquisite precision in temperature (see chapter 2), while polarization measurements are improving rapidly. Second, the CMB originated at a well known redshift of $z \sim 1100$. Finally, CMB photons have traversed nearly the entire observable universe², in principle providing information about all of the structure between Earth and the last scattering surface of the CMB. The lensing signal is thus sourced from a broad range of redshifts, primarily $0.1 < z < 5$ [81].

1. The lensing power spectrum is also sensitive to the growth function of the gravitational potential, but only on larger scales than those measured in SPTpol data.

2. In principle, the cosmic neutrino background will be measured someday, probing further out and forcing the “observable” universe to be re-defined.

Gravitational lensing can be measured by looking for distortions in the characteristic patterns of the primordial CMB temperature and polarization ([13]; for a review, see [81]). In the unlensed CMB, the covariance between CMB Fourier modes does not depend on direction (i.e., the statistics of the unlensed CMB are isotropic). In the real universe, CMB photons will be deflected around over-densities in the large-scale structure of the universe, stretching the pattern of CMB anisotropies in the direction of over-densities, and compressing the CMB anisotropies around the edges; this effect is demonstrated in figure 1 of [63]. The stretching and compressing of CMB anisotropies distorts the covariance of CMB modes in the direction of the lenses; thus the statistics of the lensed CMB depend on direction in a way that is correlated with the underlying large-scale structure (i.e. the statistics of the lensed CMB are anisotropic). In summary, lensing induces *statistical anisotropy* in the CMB.

The distortions introduced by lensing smooth the CMB temperature power spectrum [113], reducing the heights of the acoustic peaks and shifting anisotropy power from large to small scales down the steeply-falling spectrum. This was precisely the effect detected in the SPT power spectrum in section 2.5.10. In polarization, lensing distorts even-parity *E*-mode anisotropy, smoothing the *E*-mode power spectrum and producing odd-parity *B*-mode power on scales where there is very little primordial power [140]. Finally, lensing correlates modes that were originally independent [25]. The smoothing of the CMB power spectrum has been well measured in temperature [129, 30, 100] and should soon be detected in the *E*-mode power spectrum.

Lensing-induced *B*-modes were first detected in cross-correlation using data from SPTpol [52, hereafter H13]. In that analysis, a *B*-mode template was created by combining SPTpol *E*-mode maps with an estimate of the lensing potential from a Herschel-SPIRE map of the cosmic infrared background. This template was then cross-correlated with the SPTpol *B*-mode map, resulting in a 7.7σ detection of *B*-modes. Using similar cross-correlation analyses, POLARBEAR found 2.3σ evidence for lensed *B*-modes ([103]), and the Atacama Cosmology Telescope Polarimeter (ACTPol) collaboration measured lensed *B*-modes with a

3.2σ significance [132]. Recently, POLARBEAR made a measurement of the B -mode auto-spectrum which disfavored the no-lensing hypothesis at 2.0σ ([102]), BICEP2 measured a B -mode auto-spectrum which contains a lensing component measured at 5.5σ [10], and SPTpol measured the B -mode auto-spectrum at a detection significance of 4.3σ [68].

The correlation between initially independent CMB modes introduced by lensing can be measured using a quadratic estimator technique [115, 58, 63]. With this technique, the amplitude of the lensing potential power spectrum has been measured to high precision using CMB temperature data: 22% using data from $\sim 600 \text{ deg}^2$ of sky observed with the Atacama Cosmology Telescope (ACT) [30], 19% using data from $\sim 590 \text{ deg}^2$ of the 2500 deg^2 SPT-SZ survey observed with the SPT [131], and 4% using data from $\sim 28000 \text{ deg}^2$ of sky (70% of the full sky) observed with *Planck* [101]³. Data from the full 2500 deg^2 SPT-SZ survey is expected to yield a measurement of the lensing amplitude with a significance similar to that of the temperature-only *Planck* result. POLARBEAR has detected gravitational lensing with a quadratic-estimator technique using only estimators that include B -modes, rejecting the no-lensing hypothesis at 4.2σ over 30 deg^2 ([104]); combining this with their B -mode auto-spectrum measurement, POLARBEAR rejected the no-lensing hypothesis at 4.7σ ([102]).

In this chapter, we construct a map of the gravitational lensing potential and its power spectrum from temperature and polarization data collected with SPTpol within a 100 deg^2 patch of the southern sky. We combine the temperature and polarization measurements into a minimum-variance (MV) estimate of the lensing potential, and measure its power spectrum.

Throughout this chapter, we use a fiducial Λ CDM cosmological model that provides the best fit to the combination of *Planck* power spectrum, *Planck* lensing spectrum, *WMAP*-polarization, SPT, and ACT data [100], with the following parameters: baryon density $\Omega_b h^2 = 0.0222$, cold dark matter density $\Omega_c h^2 = 0.1185$, Hubble parameter $H_0 = 100 h \text{ km}$

3. The fractional precision is reported relative to the mean of each measurement.

$\text{s}^{-1} \text{Mpc}^{-1}$ with $h = 0.6794$, power spectrum of primordial curvature perturbations with an amplitude (at $k = 0.05 \text{ Mpc}^{-1}$) $A_s = 2.21 \times 10^{-9}$ and spectral index $n_s = 0.9624$, optical depth to reionization $\tau = 0.0943$, and a neutrino energy density corresponding to a sum over the neutrino mass eigenstates of 0.06 eV . Hereafter, this model will be referred to as the “PLANCK+LENS+WP+HIGHL” model. This fiducial model serves as the input to our simulations and the reference for calculating the amplitude of the lensing potential power spectrum.

This chapter is organized as follows: We describe the data used in this chapter in Section 3.1. We review the theoretical description of gravitational lensing and describe our implementation of the quadratic estimator in Section 3.2. We describe the simulations in Section 3.3. We detail our uncertainty budget in Section 3.4. We present our results in Section 3.5. We discuss potential sources of systematic errors in Section 3.6. We discuss the implications of this measurement in Section 3.7.

3.1 Sptpol Observations and Data-Processing

This chapter uses maps of the CMB temperature and polarization made with data from SPTpol deep field obtained during 2012 and a few months of 2013. The 2012 data have already been used to make the first detection of lensing B modes (H13) and to make the most precise measurement of the high- ℓ E -mode power spectrum and temperature- E -mode cross-spectrum to date [29]. The SPTpol instrument and observations are discussed in section 1.0.6 and C14; here we summarize the most important properties of the SPTpol data, processing, and resulting maps.

Only the 150 GHz data are used in this analysis. In a lensing measurement, the 150 GHz and 90 GHz data are probing the same underlying large-scale structure, and for SPTpol observations the 150 GHz data is much deeper primarily because there are more detectors in the focal plane at this frequency. The data consists of 5182 individual field observations, each covering half of the field and lasting approximately 30 minutes and composed of either

34 or 52 azimuthal scans. These observations were performed using a lead-trail strategy identical to the one used for SPT-SZ observations (see section 2.1.1). In this work we coadd lead and trail observations into single observation maps.

The raw field observations consist of time-ordered data (TOD) for each SPTpol bolometer. The TOD are combined into maps by calculating the Stokes parameters I , Q , and U in each map pixel. We refer to the Stokes parameter I as T (temperature), and use temperature units for our T , Q , and U maps. Bolometer TOD are processed into maps with the following steps:

1. Filter individual bolometer TOD.
2. Notch-filter the data in Fourier space to remove contamination from the pulse-tube.
3. Calibrate individual bolometers relative to each other.
4. Calculate individual bolometer weights based on their noise performance.
5. Cut bad bolometers on at the level of individual scans as well as full observations.
6. Combine bolometer TOD into CMB maps in T , Q , and U .
7. Coadd all observations of sufficient quality into single T , Q , and U maps.

We now describe these steps in detail.

The individual bolometer TOD are recorded as ADC counts and converted to CMB temperature units. These TOD are bandpass-filtered to remove low frequency noise from the instrument and atmosphere and to avoid high frequency noise that would be aliased from temporal noise at the pixelization scale during map-making. The high-pass filter is implemented by fitting and subtracting a fourth-order polynomial from the TOD of each detector for every scan. The low-pass filter is chosen to suppress power above a maximum angular scale of $\ell \sim 4000$ (~ 3 Hz at the telescope scan-speed), and is implemented by taking the FFT of each detector's TOD for each scan, exponentially suppressing power above the

~ 3 Hz cutoff, then taking the inverse-FFT. During the low-pass filter process, small regions of the Fourier-space signal are “notched out” by setting the TOD to zero; these regions correspond to the frequency of the pulse-tube cooler used to cool the receiver and the second to ninth harmonics of this frequency.

The individual bolometer TOD are calibrated relative to one another using a combination of regular calibration observations of an internal chopped blackbody source and of the galactic HII region RCW38. The absolute calibration (T_{cal}) is tied to the CMB maps produced by *Planck*. The absolute temperature calibration uncertainty is estimated to be $\delta T_{\text{cal}} = 1.3\%$. This calibration process is described in more detail in section 3.1.1.

The TOD are accumulated into maps using the pointing, polarization angle, and efficiency of each detector, as well as a weight calculated from the noise power of each detector between 1 and 3 Hz ($1300 \lesssim \ell \lesssim 3900$ at the telescope scan-speed). The maps are pixelized in an oblique Lambert azimuthal equal-area projection, with square $2' \times 2'$ pixels. As in chapter 2, we adopt the flat-sky approximation throughout this chapter.

The Q and U maps are multiplied by an additional calibration factor P_{cal} to correct for errors in the measured detector polarization calibration and efficiency. We use a value of $P_{\text{cal}} = 1.048$ from Table 3 in C14. This value is calculated using a Markov Chain Monte Carlo (MCMC)⁴ by fitting the SPTpol EE and TE bandpowers jointly with *Planck* TT bandpowers [100] and *WMAP9* polarization data [54] in a Λ CDM model with varying nuisance parameters; see C14 for details. The value of P_{cal} for the best-fit model from this MCMC-chain is taken as our estimate of the polarization calibration parameter. The P_{cal} calibration has an uncertainty of $\delta P_{\text{cal}} = 1.7\%$, which is calculated from the marginalized posterior of P_{cal} . We treat δP_{cal} as uncorrelated with other systematic uncertainties in Section 3.4; this over-estimates the uncertainty since P_{cal} is partially correlated with other parameters in the fit (e.g., T_{cal}).

The final SPTpol deep field maps have nearly homogeneous coverage, with inverse-noise-

4. We calculate the MCMC chain using the COSMOMC package [80].

weighted pixel hit counts varying by less than $\sim 35\%$ over the 100 deg^2 field (corresponding to the difference in the cosine of the declination angle between the top and bottom of the field), except for a $\sim 2\times$ deeper strip at the center caused by overlap of the lead and trail fields. The maps have an effective noise level, estimated between $2000 < \ell < 3000$, of $\sim 11 \mu\text{K-arcmin}$ in temperature and $\sim 9 \mu\text{K-arcmin}$ in Q and U (atmospheric noise causes a higher noise level in T than in Q or U). We use data-quality checks to cut data at three stages: individual bolometers, scans, and observations. These cuts are described in detail in C14. All data that pass these cuts are coadded into final T , Q , and U maps.

Systematic effects such as detector gain errors can cause temperature power to leak into the Q and U polarization maps. We correct for the leakage by subtracting the appropriately scaled temperature map from each polarization map as follows: $Q = Q_{\text{raw}} - \hat{\epsilon}^Q T$, and an analogous expression for U . We find $\hat{\epsilon}^Q = +0.0050$ and $\hat{\epsilon}^U = -0.0083$. See C14 for more detail⁵.

Signal power in the final maps is suppressed by two processes: data filtering and the telescope angular response function, or beam. We model the signal power removed by filtering as a 2D Fourier-space transfer function F_{ℓ}^{filt} . We obtain this transfer function using simulations of the filtering process. The SPT beam suppresses power on arcminute scales. We approximate this beam as radially symmetric, with a 2D Fourier-space transfer function F_{ℓ}^{beam} measured using observations of Mars as well as bright point sources in the deep field. The beam was measured independently in both 2012 and 2013; we use a composite beam calculated as the inverse-noise-variance weighted average of the beams from each year. Taken together, we model the total transfer function as

$$F_{\ell}^{\text{tot}} = F_{\ell}^{\text{pix}} F_{\ell}^{\text{filt}} F_{\ell}^{\text{beam}} \quad (3.1)$$

5. While this treatment is sufficient for the current analysis (see Section 3.4), more thorough cleaning is required for large angular scale B -mode power spectrum measurements such as [10] and [68]. Leakage is treated differently in those analyses because they consider larger angular scale B -modes where T and E have more power that can be leaked, and reconstruction noise dominates our lensing measurement uncertainty (as opposed to leaked power).

where F_{ℓ}^{pix} is the 2D Fourier transform of a square 2 arcminute pixel.

The SPTpol deep field contains a number of bright point sources, which we mask. We identify all sources detected at $> 5\sigma$ at 150 GHz from [88], which corresponds to a flux-cut of approximately 6 mJy; all pixels within 5 arcminutes of each source are masked in both the TOD filtering and the final maps. We extend this mask to 10 arcminutes for all very bright sources detected at $> 75\sigma$. We also use a 10 arcminutes radius to mask all galaxy clusters detected in this field by [133] using the Sunyaev-Zeldovich Effect effect. This masking removes approximately 120 sources, cutting 5 deg^2 of the field. We additionally multiply the maps by a sky mask that down-weights the noisy edges of the maps.

The processing described in this section results in a set of three coadded, masked maps: $T(\hat{\mathbf{n}})$, $Q(\hat{\mathbf{n}})$, and $U(\hat{\mathbf{n}})$. These maps are filtered with the C-inverse filtering process (see Section 3.2.1), which transforms the set of maps into filtered Fourier-space maps \bar{T}_{ℓ} , \bar{E}_{ℓ} , and \bar{B}_{ℓ} .

We apply two cuts to the coadded maps in Fourier-space. The data maps have noise that arises from two contributions: a roughly isotropic component from atmosphere at low $|\ell|$ and an anisotropic component from low-frequency noise that is uncorrelated between detectors at low $|\ell_x|$. We remove these noisy regions of Fourier space, keeping only modes with $|\ell_x| > 450$. Second, we use only modes with $|\ell| < 3000$ when estimating the lensing potential. We verify that our results are not sensitive to the exact choices of these cuts; see Section 3.6 for details.

Thus the data input to the estimator of the lensing potential (i.e., Equation 3.31) is a set of three filtered maps: \bar{T}_{ℓ} , \bar{E}_{ℓ} , and \bar{B}_{ℓ} .

3.1.1 Calibration

In this section we describe how the data are calibrated. Conceptually, the process has two steps: the TOD from each detector are calibrated relative to each other, then the data are calibrated to an absolute scale.

Relative Calibration between Detectors

The relative calibration between detectors is especially important for polarized observations, since the linear polarization of the CMB is calculated by differencing detectors of orthogonal polarizations. The relative calibration is calculated using a combination of regular observations of the galactic HII region RCW38 and of an internal chopped blackbody source. RCW38 is observed with ~ 45 minute schedules in which all detectors are scanned over the source multiple times. The internal source is observed in ~ 1 minute observations, taken approximately once per hour. Detectors in different locations on the focal plane see the internal source with different illuminations. This results in a unique effective temperature of the internal source for each detector, which is calculated from the season average of the ratio of the detector response to the internal source divided by the response to RCW38. Temperature drifts in the internal source are corrected for using the ratio of the response to the internal source in each observation divided by the season-averaged response to the internal source, averaged over all well-behaved detectors. Finally, differences in atmospheric opacity between observations are accounted for using the same strategy with RCW38 observations: we calculate the ratio of the detector response to RCW38 divided by the season-average response to RCW38, averaged over all well-behaved detectors.

Absolute Calibration

The SPTpol maps are calibrated to an absolute CMB temperature scale with a two-step process. First, the SPTpol maps are calibrated to the SPT-SZ map on the 100 deg^2 deep-field from chapter 2 and [129]. Many different half-depth SPT-SZ maps are calculated by splitting the SPT-SZ observations into random halves and coadding the two groups. Two half-depth SPTpol maps are also calculated. The absolute calibration is then

$$r_{b,i} = \frac{\hat{D}_{b,i}^{\text{SPTSZ}, \text{SPTpol}} B_b^{\text{SPTpol}}}{\hat{D}_{b,i}^{\text{SPTpol}, \text{SPTpol}} B_b^{\text{SPTSZ}}} \quad (3.2)$$

where $\widehat{D}_b^{A,B}$ is the binned cross-spectrum between maps A and B in ℓ -space bin b defined in equation 2.2, i runs over different half-depth SPT-SZ maps, B_b^{SPTpol} is the SPTpol beam averaged over the bin, and the bins cover the range $200 < \ell < 2200$ and have width $\Delta\ell = 50$. The SPT-SZ and SPTpol observations were taken with the same observing strategy and filtered identically; as a result, the filter transfer function cancels out. The uncertainty on this calibration is 0.5% in temperature. The SPT-SZ maps have been calibrated to *Planck* using the procedure described in section 2.1.4. The uncertainty on the SPT-SZ to *Planck* calibration is 1.2% in temperature; adding these uncertainties in quadrature, the absolute calibration uncertainty is 1.3%.

Polarization Calibration

We must know the precise polarization angle and efficiency of each detector in order to make accurate temperature and polarization maps. Detectors are arranged on the focal plane with nominal orientations from 0° to 180° in steps of 15° . The true polarization angles and efficiencies are measured with dedicated observations of a polarization-calibration source: a chopped thermal source mounted in the middle of a $7\text{m} \times 7\text{m}$ reflector pointed at the sky and located ~ 3 kilometers from the telescope. The source is placed source behind two wire-grid polarizers; the grid on the thermal-source side is fixed, while the second polarizer is mounted to a stepped rotation stage. For each pixel-pair, the telescope is pointed to locate the source at the center of that pixel’s beam. The outer polarizer is stepped through a series of known angles, and the resulting data are fit to a model including polarization angle and efficiency.

These observations are conducted for all pixel pairs. After cutting poor observations, measurements for $\sim 60\%$ of the detectors were obtained. The remaining detectors are given the median parameter values measured from good observations within the appropriate angle-grouping. The median statistical error to the fits of the polarization angle and efficiency are 0.46° and 0.8% , respectively, per detector. The mean polarization efficiency is 97%. The systematic uncertainty on the detector alignment angles was measured with a series of similar

observations; details are given in C14.

3.1.2 Noise estimation

Estimates of the noise in the data are used for two purposes: to create realistic simulations of SPTpol observations (including noise); and to form the C-inverse filter described in section 3.2.1. Taking advantage of the highly redundant observation strategy, the noise is estimated directly from the data. The astrophysical signal in each properly calibrated observation should be identical, however, the atmosphere and instrument noise will be uncorrelated between observations. By differencing pairs of observations, the full anisotropic structure of the noise is estimated in a model-independent way.

In practice, 500 independent realizations of the noise are created in the following way. We first make left-going and right-going maps from scans (the sum of which produces the raw data maps). All observations are divided into two halves with left-going and right-going maps for each observation separated into opposite halves. The coadd of one half is then subtracted from the coadd of the other half. Many realizations of the noise are created by choosing random sets of halves. This method of calculating the noise variance gives an unbiased but potentially noisy estimate; however, given the number of independent observations used in this work, the noise on the variance estimate is expected to be negligible.

The noise power that is correlated between detectors is estimated as the average 2D power spectrum of these noise realizations:

$$C_{\ell}^N = \left\langle \left| N_{\ell}^i \right|^2 \right\rangle_{i \in \text{realizations}} - (\text{uncorrelated pixel noise}), \quad (3.3)$$

where N_{ℓ}^i is the i^{th} noise realization described above. We set the uncorrelated pixel noise level equal to $7 \mu\text{K-arcmin}$ in both temperature and polarization. The noise power is used to create the C-inverse filter for the data; specifically, C_{ℓ}^N is the power spectrum of N_{ℓ} from

equation 3.14 and “uncorrelated pixel noise” is the noise level in n_j from equation 3.14⁶.

3.2 CMB Lensing Analysis

As CMB photons travel through the universe, their paths are deflected by gravitational interactions with intervening large-scale structure. These deflections can be described as a remapping of the CMB temperature and polarization fields [81]:

$$T(\hat{\mathbf{n}}) = \tilde{T}(\hat{\mathbf{n}} + \nabla\phi(\hat{\mathbf{n}})) \quad (3.4)$$

$$[Q \pm iU](\hat{\mathbf{n}}) = [\tilde{Q} \pm i\tilde{U}](\hat{\mathbf{n}} + \nabla\phi(\hat{\mathbf{n}})), \quad (3.5)$$

where $\hat{\mathbf{n}}$ is a unit-vector denoting a particular line-of-sight direction on the sky. Throughout this chapter, tildes denote *unlensed* quantities. The projected lensing potential $\phi(\hat{\mathbf{n}})$ is an integral over the 3-dimensional potential $\Psi(\chi\hat{\mathbf{n}}; \eta_0 - \chi)$:

$$\phi(\hat{\mathbf{n}}) = -2 \int_0^{\chi_{\text{CMB}}} d\chi \frac{f_K(\chi_{\text{CMB}} - \chi)}{f_K(\chi_{\text{CMB}}) f_K(\chi)} \Psi(\chi\hat{\mathbf{n}}; \eta_0 - \chi). \quad (3.6)$$

where χ is the comoving distance along the line of sight, χ_{CMB} is the comoving distance to the surface of last scattering, the quantity $\eta_0 - \chi$ is the conformal time at which a CMB photon would have been at position $\chi\hat{\mathbf{n}}$, and $f_K(\chi)$ is the comoving angular distance with $f_K(\chi) = \chi$ in a flat universe. The deflection field of CMB photons is given by $\vec{d}(\hat{\mathbf{n}}) = \nabla\phi(\hat{\mathbf{n}})$. The apparent local expansion or contraction of the CMB is given by the divergence of $\nabla\phi$; the convergence field is defined as $\kappa(\hat{\mathbf{n}}) \equiv -\frac{1}{2}\nabla^2\phi(\hat{\mathbf{n}})$. In this chapter, final maps and power spectra will be presented in terms of κ .

The unlensed CMB sky is well described as a statistically-isotropic, Gaussian random

6. Note: in `sptpol_software`, $\langle |N_{\ell}^i|^2 \rangle_i$ is implemented in `lensing/lens100d/make_clnk.py`, and C_{ℓ}^N is calculated in `lensing/lensing/cinv/opfilt_teb.py`, function `cl2sinv()`, including the subtraction of the uncorrelated pixel noise. The uncorrelated pixel noise n_j is calculated in `lensing/lensing/maps.py`, function `make_tqumap_wt()`.

field; in this case, all statistical information about the field is contained in the power spectrum

$$C_{\ell}^{XY} = \delta(\ell - \ell') \langle X_{\ell} Y_{\ell'}^* \rangle,$$

where $X, Y \in [T, E, B]$ are harmonic-space CMB maps. Gravitational lensing introduces statistical anisotropy in the CMB temperature and polarization fields, correlating multipole moments across a range defined by the lensing deflection field $\vec{d}(\hat{\mathbf{n}})$ [63]. Averaging over realizations of the lensed CMB fields for a fixed lensing potential, we can expand the covariance of CMB fields in a Taylor series as a function of ϕ [63]:

$$\langle X_{\ell} Y_{\ell'}^* \rangle_{\text{CMB}} = \delta(\ell - \ell') C_{\ell}^{XY} + \mathcal{T}_{\ell, \ell'}^{\phi XY} \phi_{\ell - \ell'} + \mathcal{O}(\phi^2), \quad (3.7)$$

where $\mathcal{T}_{\ell, \ell'}^{\phi XY}$ is the coefficient on the $\mathcal{O}(\phi)$ term. Information about the lensing potential is thus contained in the off-diagonal elements ($\ell \neq \ell'$) of the second term and subsequent higher order terms. Said another way, lensing distorts the observed CMB anisotropies, which introduces statistical anisotropy in the covariance of the CMB; these changes are encapsulated in the second and higher-order terms in Equation 3.7.

The analysis in this chapter will proceed in the following manner: First we filter the CMB fields in order to maximize signal to noise for the lensing calculation. Next we estimate the two-dimensional lensing potential ϕ from these filtered fields. We correct ϕ for two effects: a multiplicative normalization and an additive “mean-field” bias correction. Then we calculate the power spectrum of ϕ , and subtract two noise-bias terms. Finally, we calculate the amplitude of the final spectrum relative to a fiducial cosmology.

3.2.1 Map Filtering

The first step in this analysis is to filter the CMB fields to maximize the CMB signal relative to the noise. This is essentially a “matched filter” technique using an inverse-variance filter for data maps that have anisotropic noise and a filter transfer function. Here we first develop

the mathematical formulation of this filtering, then define the specific filter used in this analysis.

Suppose we have measurements of a field Y_ℓ which trace X_ℓ . Then we can use Y to obtain an unbiased estimator of X as

$$\hat{X}_\ell^Y = \frac{C_\ell^{XX}}{C_\ell^{XY}} \hat{Y}_\ell. \quad (3.8)$$

This measurement of X will have some noise associated with the components of Y that do not trace X . This noise is characterized by the variance $\text{Var}(\hat{X}_\ell^Y) = \langle \hat{X}_\ell^Y \rangle^2 - \langle (\hat{X}_\ell^Y)^2 \rangle$, which has the spectrum

$$C_\ell^{NN} = \left(\frac{C_\ell^{XX}}{C_\ell^{XY}} \right)^2 \left(C_\ell^{YY} - \frac{(C_\ell^{XY})^2}{C_\ell^{XX}} \right) \quad (3.9)$$

The inverse-variance filtered estimate \bar{X} is then

$$\bar{X}_\ell^Y = \left[C_\ell^{XX} + C_\ell^{NN} \right]^{-1} \hat{X}_\ell^Y \quad (3.10)$$

$$= \left[C_\ell^{XX} + C_\ell^{NN} \right]^{-1} \frac{C_\ell^{XX}}{C_\ell^{XY}} \hat{Y}_\ell. \quad (3.11)$$

Substituting in the definitions of C_ℓ^{NN} , we find

$$\bar{X}_\ell^Y = \frac{C_\ell^{XY}}{C_\ell^{XX}} \frac{1}{C_\ell^{YY}} \hat{Y}_\ell \quad (3.12)$$

$$= \frac{C_\ell^{XY}}{C_\ell^{XX}} \bar{Y}_\ell \quad (3.13)$$

In reality, we do not measure the fields Y directly. Instead, we measure noisy sky maps which contain signal convolved with the instrumental beam, TOD filtering, and pixelization operator, as well as instrumental noise and bright sources that must be masked. In order to account for the processing of our data maps, we use the following data model to

motivate our filtering choices. We will refer to data maps in position-space as d_j , where $d \in [T(\hat{\mathbf{n}}), Q(\hat{\mathbf{n}}), U(\hat{\mathbf{n}})]$ and j is the pixel index. We assume that these data maps are a combination of the sky signal $X_{\ell} \in [T_{\ell}, E_{\ell}, B_{\ell}]$ and noise given by

$$d_j = \sum_{\ell} P_{j\ell} X_{\ell} + \sum_{\ell} P_{j\ell} N_{\ell} + n_j. \quad (3.14)$$

Here, $P_{j\ell}$ is a matrix operator that applies any filter transfer functions (for example, smoothing by the instrumental beam, pixelization, and timestream filtering, e.g., Equation 3.1) and inverse-Fourier transforms the sky signal. For scalar fields (e.g., $X = T$), this operator is defined as

$$P_{j\ell} \equiv e^{i\ell \cdot \mathbf{x}_j} F_{\ell}^{\text{tot}} \frac{C_{\ell}^{XY}}{C_{\ell}^{XX}}. \quad (3.15)$$

In the analysis below, $X = Y = T$ such that the ratio of power spectra in the above equation drops out. We solve for $X(\ell) = [E \pm iB](\ell)$ simultaneously from polarized fields $[Q \pm iU](\mathbf{x}_j)$ using the operator

$$P_{j\ell} \equiv e^{i\ell \cdot \mathbf{x}_j \pm 2i\psi_{\ell}} F_{\ell}^{\text{tot}} \frac{C_{\ell}^{XY}}{C_{\ell}^{XX}}, \quad (3.16)$$

where $\psi_{\ell} = \cos^{-1}(\hat{\ell} \cdot \hat{\mathbf{x}}_j)$ is the azimuthal angle of ℓ .

The map noise is modeled with two components. The Fourier-domain noise contribution N_{ℓ} represents “sky noise” that comes from components of the sky that do not trace the CMB, such as foregrounds or emission from the atmosphere. The map-domain noise contribution n_j arises from instrumental noise; it is assumed to be white and uncorrelated between pixels. For modes that are heavily filtered, the instrumental noise may be rolled off just as the sky signal is. We ignore this effect, with the understanding that it causes our inverse-variance filtering procedure to *overestimate* the instrumental variance on such scales (relative to the sky component, which does include a filter-transfer function). Over-estimating the instrumental variance in the filter is slightly sub-optimal but will not bias the CMB filtered fields.

With a map d_j described by Equation 3.14, we can determine inverse-variance filtered Fourier modes \bar{X} as

$$\left[S^{-1} + P^\dagger n^{-1} P \right] S \bar{X} = P^\dagger n^{-1} d. \quad (3.17)$$

We solve for \bar{X} , using a conjugate-gradient-descent method to evaluate the expression

$$\bar{X} = S^{-1} \left[S^{-1} + P^\dagger n^{-1} P \right]^{-1} P^\dagger n^{-1} d, \quad (3.18)$$

where throughout this chapter, we will use an over-bar notation for inverse-variance-weighted quantities. Here S is the total sky signal covariance matrix, defined as the sum of the signal and “sky noise” power: $S \equiv C_\ell^X + C_\ell^N$; in this expression, C_ℓ^X is the theoretical power spectrum of X evaluated on the 2D Fourier plane, and C_ℓ^N is the 2D power spectrum of N_ℓ from Equation 3.14, specifically, $\langle |N_\ell|^2 \rangle$; this term is estimated from the data and is defined explicitly in equation 3.3. The matrix n^{-1} is the sky mask multiplied by the inverse of the map-noise variance $\langle |n_j^2| \rangle$. Specifically, n is calculated by taking the map-noise n_j from Equation 3.14 then setting the inverse-noise level $n_j^{-1} = 0$ for masked pixels j (this is equivalent to taking $n_j \rightarrow \infty$ for masked pixels).

In order to relate Equation 3.18 to the equations earlier in this section, consider estimating field X from a map d_j^Y (in the form of Equation 3.14) of the Y field. In the limit of low map-noise, we can set $n_j = \epsilon$ to find

$$\lim_{\epsilon \rightarrow 0} \bar{X}_\ell = \lim_{\epsilon \rightarrow 0} S^{-1} \left[S^{-1} + P^\dagger (1/\epsilon) P \right]^{-1} P^\dagger (1/\epsilon) d_j^Y \quad (3.19)$$

$$= \lim_{\epsilon \rightarrow 0} S^{-1} \left[P^\dagger (1/\epsilon) P \right]^{-1} P^\dagger (1/\epsilon) d_j^Y \quad (3.20)$$

$$= \lim_{\epsilon \rightarrow 0} S^{-1} P^{-1} \epsilon (P^\dagger)^{-1} P^\dagger (1/\epsilon) d_j^Y \quad (3.21)$$

$$= \lim_{\epsilon \rightarrow 0} S^{-1} P^{-1} d_j^Y \quad (3.22)$$

$$= \lim_{\epsilon \rightarrow 0} S^{-1} \frac{C_\ell^{XX}}{C_\ell^{XY}} (F_\ell^{\text{tot}})^{-1} \left(e^{-i\ell \cdot \mathbf{x}_j} d_j^Y \right) \quad (3.23)$$

Intuitively, from right to left, this corresponds to (1) Fourier-transforming the map, (2) deconvolving the transfer function, and (3) determining the filtered multipoles \bar{X} following Equation 3.11.

Finally, we would like to write the C-inverse filter of Equation 3.18 in a simpler, approximate form which is useful for analytic calculations. The C-inverse filter can be described as an operator in two-dimensional Fourier-space that can mix power between ℓ -modes. By ignoring the mode-mixing, this filter can be approximated as a diagonal Fourier-space filter function. We can model the signal \bar{X}_ℓ as a filtered signal plus noise component,

$$\bar{X}_\ell \approx \mathcal{F}_\ell^X X_\ell + n_\ell^X, \quad (3.24)$$

and approximate each operator in Equation 3.18 as diagonal in Fourier-space. Considering only the signal component of the map (Equation 3.14), the filter function \mathcal{F}_ℓ^X then takes the form:

$$\mathcal{F}_\ell^X X_\ell = S^{-1} \left[S^{-1} + P^\dagger n^{-1} P \right]^{-1} P^\dagger n^{-1} (P X) \quad (3.25)$$

$$= S^{-1} \left[S^{-1} + P^2/n \right]^{-1} (P^2/n) X \quad (3.26)$$

$$= S^{-1} \left[n S^{-1} / P^2 + 1 \right]^{-1} X \quad (3.27)$$

$$= \left[n/P^2 + S \right]^{-1} X \quad (3.28)$$

$$= [C^{nn} + S]^{-1} X_\ell, \quad (3.29)$$

where $C^{nn} \equiv n/P^2$ is the power spectrum of the map noise (in which the beam (F_ℓ^{beam}) and filter-transfer function (F_ℓ^{filt}) have been divided out in Fourier-space; see Section 3.1 for more detail). In summary, the effect of the C-inverse filter on a signal X can be approximated as

a filter that is diagonal in Fourier-space with the following form⁷:

$$\mathcal{F}_{\ell}^X X_{\ell} = [C^{nn} + S]^{-1} X_{\ell}. \quad (3.30)$$

The filtered fields \bar{X}_{ℓ} form the input to the estimator of the lensing potential.

3.2.2 Quadratic Estimator of ϕ

We now construct an estimator for the lensing potential that takes advantage of the off-diagonal correlations introduced by lensing in the CMB fields [63]. Calculating a properly normalized, unbiased estimate of ϕ requires three steps that are detailed below:

1. Calculate an inverse-variance-weighted estimate of the lensing potential ($\bar{\phi}_{\mathbf{L}}$) from two filtered CMB fields, i.e., TT , TE , EE , EB , and TB ⁸.
2. Remove a “mean-field” bias.
3. Normalize the estimate. In the ϕ -estimator we use in this chapter, the correct normalization of the estimate of ϕ for a given value of \mathbf{L} . is one over the total inverse-variance weight. The best estimate of the lensing potential after normalization will be designated with a hat symbol, $\hat{\phi}_{\mathbf{L}}$.

Using two CMB fields \bar{X} and \bar{Y} that have been filtered as described in Section 3.2.1, we estimate the inverse-variance-weighted lensing potential as follows:

$$\bar{\phi}_{\mathbf{L}}^{XY} = \int d^2\ell W_{\ell, \ell-\mathbf{L}}^{XY} \bar{X}_{\ell} \bar{Y}_{\ell-\mathbf{L}}^* \quad (3.31)$$

where $W_{\ell, \ell-\mathbf{L}}^{XY}$ is a weight function as described below. Analogous to \bar{X} , we continue to use the over-bar notation to indicate that $\bar{\phi}_{\mathbf{L}}$ is an inverse-variance-weighted field. This

7. Note: \mathcal{F}_{ℓ}^X is implemented in `sptpol.software` in `lensing/lensing/sims/cinv.py`, class “library”, function “`get.fl()`”.

8. BB has vanishing signal-to-noise; see the discussion following Equation 3.38.

estimation technique amounts to taking a weighted sum of the covariance between \bar{X}_{ℓ} and $\bar{Y}_{\ell'}$ at all pairs of angular wavenumbers ℓ and ℓ' separated by $\ell - \ell' = \mathbf{L}$. As indicated by Equation 3.7, modes ℓ in \bar{X} and ℓ' in \bar{Y} have a covariance that is imprinted by modes in the lensing potential ϕ with angular wavenumber \mathbf{L} .

The weight function $W_{\ell, \ell-\mathbf{L}}^{XY}$ acts like a matched filter; in Equation 3.31 this weight is convolved in Fourier-space with the two filtered CMB fields to maximize the response to the lensing signal. We use the minimum-variance estimator for this analysis [63], in which this weight function is simply the leading-order coefficient on ϕ in Equation 3.7: $W_{\ell, \ell-\mathbf{L}}^{XY} \equiv \mathcal{T}_{\ell, \ell-\mathbf{L}}^{\phi^{XY}}$.⁹ In general, other weight functions can be used (for example, “bias-hardened” estimators defined in [90]).

This estimator is biased since it includes contributions that arise from the statistical anisotropy introduced by non-lensing sources such as the sky mask, in-homogeneous map noise, etc. These terms constitute a “mean-field” (MF) bias, defined as

$$\bar{\phi}_{\mathbf{L}}^{XY, \text{MF}} = \int d^2\ell W_{\ell, \ell-\mathbf{L}}^{XY} \langle \bar{X}_{\ell} \bar{Y}_{\ell-\mathbf{L}}^* \rangle, \quad (3.32)$$

where the average is taken over realizations of the CMB and noise. We calculate the MF contribution by averaging over estimates of ϕ from Monte-Carlo (MC) simulations with independent realizations of the CMB, lensing potential, and instrument noise. Since the simulated lensing signal is uncorrelated from simulation to simulation, it averages to zero in this calculation; the common signal that remains after averaging is the MF bias.

Finally, we need to normalize the response of the estimator to produce an unbiased estimate of ϕ . This unbiased estimate will be designated with a hat symbol, $\hat{\phi}_{\mathbf{L}}$. We calculate this normalization in a two-step process. We analytically calculate the normalization as a 2D Fourier-space object, then correct the analytic normalization using simulations.

9. In contrast to [63] which uses the unlensed CMB spectrum in this definition, we use the lensed CMB spectrum following the treatment of [82].

Drawing on the intuition that the estimator is a weighted sum of off-diagonal elements in the covariance between \bar{X}_ℓ and \bar{Y}_ℓ , the desired normalization is the reciprocal of the sum of these weights. In the analytic calculation of the normalization, we account for the map-filtering process described in Section 3.2.1 with the diagonal approximation of the C-inverse filter, \mathcal{F}_ℓ , from Equation 3.30.

Under this approximation, the normalization is given by

$$\mathcal{R}_{\mathbf{L}}^{XY, \text{Analytic}} = \int d^2\ell W_{\ell, \ell-\mathbf{L}}^{XY} \times W_{\ell, \ell-\mathbf{L}}^\phi \mathcal{F}_\ell^X \mathcal{F}_{\ell-\mathbf{L}}^Y, \quad (3.33)$$

where the weight function $W_{\ell, \ell-\mathbf{L}}^\phi = W_{\ell, \ell-\mathbf{L}}$ in the MV estimator used here, but can be different in the general case. Note that in the absence of filtering (i.e., $\mathcal{F}_\ell = 1$), this equation is effectively the sum of the weights from Equation 3.31. The approximation \mathcal{F}_ℓ^X is not exact; we therefore calculate a multiplicative normalization correction $\mathcal{R}_{\mathbf{L}}^{XY, \text{MC}}$ from simulations,

$$\mathcal{R}_{\mathbf{L}}^{XY, \text{MC}} = \frac{\langle \hat{\phi}_{\mathbf{L}}'^{XY} \phi_{\mathbf{L}}^{I*} \rangle}{\langle \phi_{\mathbf{L}}^I \phi_{\mathbf{L}}^{I*} \rangle}, \quad (3.34)$$

where for each simulated realization, $\phi_{\mathbf{L}}^I$ is the input and

$$\hat{\phi}_{\mathbf{L}}'^{XY} = \frac{1}{\mathcal{R}_{\mathbf{L}}^{XY, \text{Analytic}}} (\bar{\phi}_{\mathbf{L}}^{XY} - \bar{\phi}_{\mathbf{L}}^{XY, \text{MF}}) \quad (3.35)$$

is the matching reconstruction, normalized by the analytic normalization. The reconstruction $\hat{\phi}_{\mathbf{L}}'^{XY}$ is masked, the denominator is taken directly from the harmonic-space input maps, and the appropriate factor of f_{mask} (see Equation 3.68) is applied. The average is taken over 400 simulations. In principle (or the limit of many, many simulations), the correct normalization would be the product of $\mathcal{R}_{\mathbf{L}}^{XY, \text{Analytic}}$ with $\mathcal{R}_{\mathbf{L}}^{XY, \text{MC}}$ in the 2D \mathbf{L} -plane, however, each individual mode in $\mathcal{R}_{\mathbf{L}}^{XY, \text{MC}}$ is still very noisy, making this method intractable. We expect this normalization to be isotropic, so we average $\mathcal{R}_{\mathbf{L}}^{XY, \text{MC}}$ within annuli in \mathbf{L} -space

to produce

$$\mathcal{R}_L^{XY,MC} = \langle \mathcal{R}_{\mathbf{L}}^{XY,MC} \rangle. \quad (3.36)$$

The normalization we use is the product of the analytically calculated normalization with the annulus-averaged *MC* correction:

$$\mathcal{R}_{\mathbf{L}}^{XY} \equiv \mathcal{R}_{\mathbf{L}}^{XY,\text{Analytic}} \times \mathcal{R}_L^{XY,MC}. \quad (3.37)$$

We expect the *MC* correction to be relatively small, and indeed, we find that $\mathcal{R}_L^{XY,MC}$ is a $\leq 10\%$ correction.

For each combination of fields X and Y , our estimator of the lensing potential is defined as

$$\hat{\phi}_{\mathbf{L}}^{XY} = \frac{1}{\mathcal{R}_{\mathbf{L}}^{XY}} (\bar{\phi}_{\mathbf{L}}^{XY} - \bar{\phi}_{\mathbf{L}}^{XY, \text{MF}}). \quad (3.38)$$

We calculate all five temperature and polarization estimators $XY \in [TT, TE, EE, EB, TB]$ (a quadratic estimate of ϕ from BB has vanishing signal-to-noise in a cosmology with negligible gravitational wave perturbations¹⁰ [81]).

We now want to combine these estimates into one MV estimate of the lensing potential, denoted by $\hat{\phi}_{\mathbf{L}}^{\text{MV}}$. We form $\hat{\phi}_{\mathbf{L}}^{\text{MV}}$ from a weighted average of the five estimators, where the optimal weight $w_{\mathbf{L}}^{XY}$ for the MV estimator is $\mathcal{R}_{\mathbf{L}}^{XY}$. This can be understood as follows. In quadratic maximum likelihood estimators, $\mathcal{R}_{\mathbf{L}}^{XY}$ is the Fisher matrix for $\phi_{\mathbf{L}}^{XY}$; this means that the un-normalized estimate $\bar{\phi} - \bar{\phi}^{\text{MF}}$ is the inverse-variance-weighted lens reconstruction. Thus we calculate the average of the inverse-variance-weighted estimators $(\bar{\phi} - \bar{\phi}^{\text{MF}})$, and divide by the sum of the normalizations. This is equivalent to calculating a weighted-sum

10. This can be understood intuitively as follows. A cosmology with negligible gravitational wave perturbations has negligible primordial B -mode power. The main contribution of B -mode power will come from E -modes that have been lensed. This means that when the B -mode power is expanded as Taylor-series in the lensing potential ϕ , the leading-order term will be first-order and higher in ϕ . The quadratic BB estimator is constructed from two copies of the B -mode field; therefore the leading term will be second-order in ϕ and will thus be negligible.

of the $\hat{\phi}$ estimators, where the weight $w_{\mathbf{L}}^{XY}$ is the normalization, $\mathcal{R}_{\mathbf{L}}^{XY}$. For each \mathbf{L} mode,

$$\hat{\phi}_{\mathbf{L}}^{\text{MV}} = \frac{\sum_{XY} w_{\mathbf{L}}^{XY} \hat{\phi}_{\mathbf{L}}^{XY}}{\sum_{XY} w_{\mathbf{L}}^{XY}}, \quad (3.39)$$

where the sum is taken over $XY \in [TT, TE, ET, EE, EB, BE, TB, BT]$. We additionally form a polarization-only (POL) estimate $\hat{\phi}_{\mathbf{L}}^{\text{POL}}$ from a weighted average of the EE , EB , and BE estimators. Maps and power spectra of the lensing potential are calculated from both the MV and POL estimators.

3.2.3 Evaluating the ϕ -estimator

The integrals in the quadratic estimates of ϕ (e.g., Equation 3.31) are convolutions in ℓ -space. It is thus much more computationally efficient to calculate these integrals as the product of Fourier transforms according to the convolution theorem.

Convolution Formalism

Generically, the convolution theorem can be shown as follows. Define two fields, $f(\mathbf{x})$ and $g(\mathbf{y})$. The Fourier transforms of these fields are then

$$F(\boldsymbol{\ell}) = \mathcal{F}\{f(\mathbf{x})\} \equiv \int d^2\mathbf{x} f(\mathbf{x}) e^{-i2\pi\boldsymbol{\ell}\cdot\mathbf{x}} \quad (3.40)$$

$$f(\mathbf{x}) = \mathcal{F}^{-1}\{F(\boldsymbol{\ell})\} \equiv \int d^2\boldsymbol{\ell} F(\boldsymbol{\ell}) e^{i2\pi\boldsymbol{\ell}\cdot\mathbf{x}}. \quad (3.41)$$

The convolution of $F(\boldsymbol{\ell})$ and $G(\boldsymbol{\ell})$ is

$$\text{Conv}(F, G)(\mathbf{L}) \equiv \int d^2\boldsymbol{\ell} F(\boldsymbol{\ell}) G(\mathbf{L} - \boldsymbol{\ell}) \quad (3.42)$$

This convolution can be re-written in terms of Fourier-transforms as follows:

$$\text{Conv}(F, G)(\mathbf{L}) = \int d^2\boldsymbol{\ell} F(\boldsymbol{\ell}) G(\mathbf{L} - \boldsymbol{\ell}) \quad (3.43)$$

$$= \int d^2\boldsymbol{\ell} d^2\mathbf{x} d^2\mathbf{y} f(\mathbf{x}) e^{-i2\pi\boldsymbol{\ell}\cdot\mathbf{x}} g(\mathbf{y}) e^{-i2\pi(\mathbf{L}-\boldsymbol{\ell})\cdot\mathbf{y}} \quad (3.44)$$

$$= \int d^2\mathbf{x} d^2\mathbf{y} f(\mathbf{x}) g(\mathbf{y}) e^{-i2\pi\mathbf{L}\cdot\mathbf{y}} \int d^2\boldsymbol{\ell} e^{-i2\pi\boldsymbol{\ell}\cdot(\mathbf{x}-\mathbf{y})} \quad (3.45)$$

$$= \int d^2\mathbf{x} d^2\mathbf{y} f(\mathbf{x}) g(\mathbf{y}) e^{-i2\pi\mathbf{L}\cdot\mathbf{y}} \delta(\mathbf{y} - \mathbf{x}) \quad (3.46)$$

$$= \int d^2\mathbf{x} f(\mathbf{x}) g(\mathbf{x}) e^{-i2\pi\mathbf{L}\cdot\mathbf{x}} \quad (3.47)$$

$$= \int d^2\mathbf{x} \mathcal{F}^{-1}\{F(\mathbf{l}_0)\} \mathcal{F}^{-1}\{G(\mathbf{l}_1)\} e^{-i2\pi\mathbf{L}\cdot\mathbf{x}} \quad (3.48)$$

$$= \mathcal{F}\{\mathcal{F}^{-1}\{F(\mathbf{l}_0)\}(\mathbf{x}) \mathcal{F}^{-1}\{G(\mathbf{l}_1)\}(\mathbf{x})\}(\mathbf{L}) \quad (3.49)$$

For the weight functions used in this analysis, the integrand of Equation 3.31 can be factored into the form

$$W_{\boldsymbol{\ell}, \mathbf{L}-\mathbf{L}}^{XY} \bar{X}_{\boldsymbol{\ell}} \bar{Y}_{\mathbf{L}-\mathbf{L}}^* = F(\boldsymbol{\ell}) \times G(\mathbf{L} - \boldsymbol{\ell}) \times H(\mathbf{L}), \quad (3.50)$$

where $\boldsymbol{\ell}$ is the integration variable. Equation 3.31 can then be evaluated with FFT's using the convolution theorem as follows:

$$\bar{\phi}_{\mathbf{L}}^{XY} = \int d^2\boldsymbol{\ell} W_{\boldsymbol{\ell}, \mathbf{L}-\mathbf{L}}^{XY} \bar{X}_{\boldsymbol{\ell}} \bar{Y}_{\mathbf{L}-\mathbf{L}}^* \quad (3.51)$$

$$= \int d^2\boldsymbol{\ell} F(\boldsymbol{\ell}) \times G(\mathbf{L} - \boldsymbol{\ell}) \times H(\mathbf{L}) \quad (3.52)$$

$$= H(\mathbf{L}) \int d^2\boldsymbol{\ell} F(\boldsymbol{\ell}) \times G(\mathbf{L} - \boldsymbol{\ell}) \quad (3.53)$$

$$= H(\mathbf{L}) \times \mathcal{F}\{\mathcal{F}^{-1}\{F(\boldsymbol{\ell})\}(\mathbf{x}) \mathcal{F}^{-1}\{G(\mathbf{L} - \boldsymbol{\ell})\}(\mathbf{x})\}(\mathbf{L}). \quad (3.54)$$

Example 1: $\bar{\phi}_{\mathbf{L}}^{TT}$

In this example, we show in explicit detail the terms for the $\bar{\phi}_{\mathbf{L}}^{TT}$ estimator. The weight function from Equation 3.31 is:

$$W_{\boldsymbol{\ell}, \boldsymbol{\ell}'}^{TT} = \mathbf{L} \cdot \boldsymbol{\ell} C_{\boldsymbol{\ell}}^{TT} + \mathbf{L} \cdot (\mathbf{L} - \boldsymbol{\ell}) C_{\boldsymbol{\ell}'}^{TT} \quad (3.55)$$

$$= \mathbf{L} \cdot \boldsymbol{\ell} C_{\boldsymbol{\ell}}^{TT} + \mathbf{L} \cdot (-\boldsymbol{\ell}') C_{\boldsymbol{\ell}'}^{TT} \quad (3.56)$$

$$= \mathbf{L} \cdot \boldsymbol{\ell} C_{\boldsymbol{\ell}}^{TT} + \mathbf{L} \cdot (\boldsymbol{\ell}_1) C_{\boldsymbol{\ell}'}^{TT} \quad (3.57)$$

where again $\boldsymbol{\ell}' = \boldsymbol{\ell} - \mathbf{L}$, and we have defined $\boldsymbol{\ell}_1 \equiv -\boldsymbol{\ell}'$. We now factor this equation into the desired form, expressing the dot-products as cosines in their exponential form:

$$\mathbf{L} \cdot \boldsymbol{\ell} = L\ell \cos(\theta_0 - \theta_L) \quad (3.58)$$

$$= L\ell \frac{1}{2} \left(e^{+i(\theta_0 - \theta_L)} + e^{-i(\theta_0 - \theta_L)} \right) \quad (3.59)$$

$$= L\ell \frac{1}{2} \left(e^{+i\theta_0} e^{-i\theta_L} + e^{-i\theta_0} e^{+i\theta_L} \right), \quad (3.60)$$

where θ_0 and θ_L are the azimuthal angles of $\boldsymbol{\ell}$ and \mathbf{L} , respectively. thus we find:

$$\begin{aligned} W_{\boldsymbol{\ell}, \boldsymbol{\ell}'}^{TT} &= W_{\boldsymbol{\ell}, (-\boldsymbol{\ell}_1)}^{TT} = \\ &\left[C_{\boldsymbol{\ell}}^{TT} L\ell \frac{1}{2} \left(e^{+i\theta_0} e^{-i\theta_L} + e^{-i\theta_0} e^{+i\theta_L} \right) + C_{\boldsymbol{\ell}_1}^{TT} L\ell_1 \frac{1}{2} \left(e^{+i\theta_1} e^{-i\theta_L} + e^{-i\theta_1} e^{+i\theta_L} \right) \right] \\ &= \left\{ \left[\left(\frac{1}{2} L e^{-i\theta_L} \right) C_{\boldsymbol{\ell}}^{TT} \ell e^{+i\theta_0} \right] + \left[\left(\frac{1}{2} L e^{+i\theta_L} \right) C_{\boldsymbol{\ell}}^{TT} \ell e^{-i\theta_0} \right] + \right. \\ &\quad \left. \left[\left(\frac{1}{2} L e^{-i\theta_L} \right) C_{\boldsymbol{\ell}_1}^{TT} \ell_1 e^{+i\theta_1} \right] + \left[\left(\frac{1}{2} L e^{+i\theta_L} \right) C_{\boldsymbol{\ell}_1}^{TT} \ell_1 e^{-i\theta_1} \right] \right\} \end{aligned} \quad (3.61)$$

The integral in Equation 3.31 can thus be expressed as the sum of these four terms, each of which is now in the form of Equation 3.50. This is implemented in the analysis computer

Table 3.1: Terms in the evaluation of $\bar{\phi}^{TT}$

term	t0 (i=0)		t1 (i=1)		t2 (i=2)		t3 (i=3)	
	wl[i=0][:]	sl[i=0][:]	wl[i=1][:]	sl[i=1][:]	wl[i=2][:]	sl[i=2][:]	wl[i=3][:]	sl[i=2][:]
$F(\boldsymbol{\ell})$	$C_{\boldsymbol{\ell}}^{TT}\boldsymbol{\ell}$	+1	$C_{\boldsymbol{\ell}}^{TT}\boldsymbol{\ell}$	-1	$-\frac{1}{2}$	0	$-\frac{1}{2}$	0
$G(\boldsymbol{\ell}_1)$	$-\frac{1}{2}$	0	$-\frac{1}{2}$	0	$C_{\boldsymbol{\ell}_1}^{TT}\boldsymbol{\ell}_1$	+1	$C_{\boldsymbol{\ell}_1}^{TT}\boldsymbol{\ell}_1$	-1
$H(\mathbf{L})$	L	+1	L	-1	L	+1	L	-1

These terms are related to Equation 3.50 as follows:

$$\begin{aligned} F(\boldsymbol{\ell}) &= \text{wl}[i][0](\boldsymbol{\ell})\bar{X}(\boldsymbol{\ell})e^{+i(\text{sl}[i][0])\theta_0}, \\ G(\boldsymbol{\ell}_1) &= \text{wl}[i][1](\boldsymbol{\ell}_1)\bar{Y}(\boldsymbol{\ell}_1)e^{+i(\text{sl}[i][1])\theta_1}, \text{ and} \\ H(\mathbf{L}) &= \text{wl}[i][2](\mathbf{L})e^{-i(\text{sl}[i][2])\theta_L}. \end{aligned}$$

Note: This system of coefficients implemented in `sptpol_software` in `lensing/lensing/qest.py`, class “qest”, function “eval()”. The 1/2 factor in equation 7.5 of [81] is included in “qest.eval()”, rather than in the filter function. The coefficients for $\bar{\phi}^{TT}$ are specified in class “qest.plm_TT” with the fields “self.wl” and “self.sl”.

code as 2-dimensional arrays of coefficients “wl” and “sl” such that

$$\bar{\phi}^{XY} = \frac{1}{2} \times \sum_{i=0}^{\text{nterm}} \text{wl}[i][2](\mathbf{L})e^{-i(\text{sl}[i][2])\theta_L} \times \text{Conv} \left(\text{wl}[i][0](\boldsymbol{\ell})\bar{X}(\boldsymbol{\ell})e^{+i(\text{sl}[i][0])\theta_0}, \text{wl}[i][1](\boldsymbol{\ell}_1)\bar{Y}(\boldsymbol{\ell}_1)e^{+i(\text{sl}[i][1])\theta_1} \right) \quad (3.62)$$

where we have used the theorem that because $Y(\hat{n})$ is a real field, it’s Fourier conjugate $\bar{Y}(\boldsymbol{\ell}')$ obeys the following identity: $\bar{Y}^*(\boldsymbol{\ell}') = \bar{Y}(-\boldsymbol{\ell}') = \bar{Y}(\boldsymbol{\ell}_1)$. In the case of $\bar{\phi}^{TT}$ described above, $\text{nterm}=4$. The coefficients are given explicitly in Table 3.1. The factor of $1/(\tilde{C}_l^{TT,tot}\tilde{C}_{|\boldsymbol{\ell}-\mathbf{L}|}^{TT,tot})$ which appears in Equation 14 of [63] and Equation 7.5 of [81] is built into the filtered fields \bar{X} and \bar{Y} .

Example 2: $\mathcal{R}_{\mathbf{L}}^{TT,\text{Analytic}}$

In this example, we show in explicit detail the calculation of the normalization $\mathcal{R}_{\mathbf{L}}^{TT,\text{Analytic}}$, as defined in Equation 3.33. The weight function is the same as in Equation 3.55, so the integrand of Equation 3.33 is given by

$$\left[\mathbf{L} \cdot \boldsymbol{\ell} C_l^{TT} + \mathbf{L} \cdot (\mathbf{L} - \boldsymbol{\ell}) C_{|\boldsymbol{\ell}-\mathbf{L}|}^{TT} \right]^2 \times \mathcal{F}_{\boldsymbol{\ell}}^X \mathcal{F}_{\boldsymbol{\ell}-\mathbf{L}}^Y, \quad (3.63)$$

where the filtering functions \mathcal{F}_{ℓ}^X and \mathcal{F}_{ℓ}^Y are calculated using the diagonal approximation from Equation 3.30. The integrand can again be factored into the form of Equation 3.50 by again expressing the trigonometry functions as exponentials. The normalization can then be expressed in the following form:

$$F(\ell, i, j) \equiv \text{wl}[i][0](\ell) \times \text{wl}[j][0](\ell) \times \mathcal{F}_{\ell}^X \times e^{+i(\text{sl}[i][0] + \text{sl}[j][0])\theta_0} \quad (3.64)$$

$$G(\ell_1, i, j) \equiv \text{wl}[i][1](\ell_1) \times \text{wl}[j][1](\ell_1) \times \mathcal{F}_{\ell_1}^Y \times e^{+i(\text{sl}[i][1] + \text{sl}[j][1])\theta_1} \quad (3.65)$$

$$H(\mathbf{L}, i, j) \equiv \text{wl}[i][2](\mathbf{L}) \times \text{wl}[j][2](\mathbf{L}) e^{-i(\text{sl}[i][2] + \text{sl}[j][2])\theta_L} \quad (3.66)$$

$$\mathcal{R}_{\mathbf{L}}^{TT, \text{Analytic}} \equiv \sum_{i=0}^{\text{nterm}_1} \sum_{j=0}^{\text{nterm}_2} H(\mathbf{L}, i, j) \times \text{Conv}(F(\ell, i, j), G(\ell_1, i, j)) \quad (3.67)$$

The coefficients wl and sl are again those given in Table 3.1.

3.2.4 The Power Spectrum of ϕ

In this section, we present our method for estimating the power spectrum of the lensing potential. The steps are as follows, with a more detailed description given below.

1. Calculate a cross-spectrum ($C_{\mathbf{L}}^{\hat{\phi}^{UV} \hat{\phi}^{XY}}$) from two estimates of ϕ , $\hat{\phi}_{\mathbf{L}}^{UV}$ and $\hat{\phi}_{\mathbf{L}}^{XY}$.
2. Calculate and subtract noise-bias terms ($\Delta C_{\mathbf{L}}^{\phi^{UV} \phi^{XY}} \Big|_{\text{RDN0}}$ and $\Delta C_{\mathbf{L}}^{\phi^{UV} \phi^{XY}} \Big|_{\text{N1}}$). The de-biased spectrum for this combination of CMB fields is denoted as $\hat{C}_{\mathbf{L}}^{\phi^{UV} \phi^{XY}}$, with a hat symbol to indicate that this is our best estimate.
3. Average this spectrum into bins in L . The binned spectrum we report is denoted as $\hat{C}_{L_b}^{\phi^{UV} \phi^{XY}}$.
4. Finally, calculate the amplitude of $\hat{C}_{\mathbf{L}}^{\phi^{UV} \phi^{XY}}$ relative to a fiducial spectrum. Note, the amplitude is calculated directly from the 2D \mathbf{L} -plane, rather than from the binned spectrum.

The power spectrum from two estimates $\hat{\phi}^{UV}$ and $\hat{\phi}^{XY}$ is

$$C_{\mathbf{L}}^{\hat{\phi}^{UV}\hat{\phi}^{XY}} \equiv f_{\text{mask}}^{-1} \langle \hat{\phi}_{\mathbf{L}}^{UV} \hat{\phi}_{\mathbf{L}}^{*XY} \rangle, \quad (3.68)$$

where f_{mask} is the average value of the fourth power of the apodization and point-source mask. In the following discussion, we will drop the UV, XY superscripts ($C_L^{\phi\phi}$) unless they are needed for clarity. Note that in this power spectrum calculation, the mean-field correction ϕ^{MF} is estimated from two independent sets of simulations for each of the two $\hat{\phi}$ estimates. We must do this because our estimates of the mean-field are noisy, owing to a finite number of simulations. By using separate estimates of the mean-field, we eliminate correlations between the two $\hat{\phi}$ estimates resulting from this noisy subtraction.

While this estimate of the $C_L^{\phi\phi}$ power spectrum has minimal variance, it suffers from additive biases which we must subtract. We now describe these additive bias terms. The estimates of ϕ are quadratic, i.e., 2-point functions of the CMB fields, thus the cross-spectrum $C_{\mathbf{L}}^{\hat{\phi}\hat{\phi}}$ between estimates of ϕ probes the 4-point function (trispectrum) of the CMB. The CMB trispectrum includes contributions from disconnected and connected pieces, only some of which contain information about $C_L^{\phi\phi}$. The remaining correlations show up as “noise bias” terms in $C_{\mathbf{L}}^{\hat{\phi}\hat{\phi}}$ [70]. At a given order, the disconnected pieces arise from lower-order correlations, while the connected pieces are new at each order. In the case of the CMB trispectrum, the 2-point (Gaussian) correlations in the CMB give rise to the disconnected pieces, while the higher-order (non-Gaussian) correlations introduced by lensing give rise to the connected pieces. We model the full cross-spectrum, including bias terms, as:

$$C_{\mathbf{L}}^{\hat{\phi}\hat{\phi}} = \hat{C}_{\mathbf{L}}^{\phi\phi} + \Delta C_{\mathbf{L}}^{\phi\phi}|_{\text{N0}} + \Delta C_{\mathbf{L}}^{\phi\phi}|_{\text{N1}} + \Delta C_{\mathbf{L}}^{\phi\phi}|_{\text{MC}} \quad (3.69)$$

where $\hat{C}_{\mathbf{L}}^{\phi\phi}$ is the term we want to calculate, $\Delta C_{\mathbf{L}}^{\phi\phi}|_{\text{N0}}$ and $\Delta C_{\mathbf{L}}^{\phi\phi}|_{\text{N1}}$ are the disconnected and connected pieces of the trispectrum, respectively, and $\Delta C_{\mathbf{L}}^{\phi\phi}|_{\text{MC}}$ encapsulates any remaining bias terms. We discuss each of these terms below, and show them in Figure 3.1.

The first bias term $\Delta C_{\mathbf{L}}^{\phi\phi}\big|_{\text{N0}}$ arises from disconnected contributions to the trispectrum. This term has no dependence on ϕ and arises from Gaussian correlations in the CMB fields, foregrounds, and noise; this term is called “N0” because it is zeroth-order in $C_L^{\phi\phi}$. We estimate the N0 contribution from simulations in the following way: We create two sets of simulations, MC and MC' , with different realizations of the CMB and ϕ (including foregrounds and noise). The prescription for calculating N0 from the MC and MC' simulations can be written as the sum of two terms:

$$\Delta C_{\mathbf{L}}^{\phi\phi}\big|_{\text{N0}} = \left\langle +C_{\mathbf{L}}^{\hat{\phi}\hat{\phi}}[\bar{U}_{\text{MC}}, \bar{V}_{\text{MC}'}, \bar{X}_{\text{MC}}, \bar{Y}_{\text{MC}'}] + C_{\mathbf{L}}^{\hat{\phi}\hat{\phi}}[\bar{U}_{\text{MC}}, \bar{V}_{\text{MC}'}, \bar{X}_{\text{MC}'}, \bar{Y}_{\text{MC}}] \right\rangle_{\text{MC}, \text{MC}'} \quad (3.70)$$

where we have re-written $C_{\mathbf{L}}^{\hat{\phi}^{UV}\hat{\phi}^{XY}}$ to explicitly show the dependence on the four input fields U, V, X, Y : $C_{\mathbf{L}}^{\hat{\phi}\hat{\phi}}[\bar{U}, \bar{V}, \bar{X}, \bar{Y}] \equiv C_{\mathbf{L}}^{\hat{\phi}^{UV}\hat{\phi}^{XY}}$.

This estimate of the N0 bias for the data will be imperfect because the power spectrum used in the simulations will be different from that of the data. We can reduce our sensitivity to this difference by using the data itself, a correction called the “realization-dependent N0” (RDN0) bias [90]. We calculate the RDN0 bias by replacing one of the CMB fields in the estimate of N0 with the data itself, then combining it with the N0 estimate above:

$$\begin{aligned} \Delta C_{\mathbf{L}}^{\phi\phi}\big|_{\text{RDN0}} = & \left\langle +C_{\mathbf{L}}^{\hat{\phi}\hat{\phi}}[\bar{U}_{\text{d}}, \bar{V}_{\text{MC}}, \bar{X}_{\text{d}}, \bar{Y}_{\text{MC}}] + C_{\mathbf{L}}^{\hat{\phi}\hat{\phi}}[\bar{U}_{\text{MC}}, \bar{V}_{\text{d}}, \bar{X}_{\text{d}}, \bar{Y}_{\text{MC}}] \right. \\ & + C_{\mathbf{L}}^{\hat{\phi}\hat{\phi}}[\bar{U}_{\text{d}}, \bar{V}_{\text{MC}}, \bar{X}_{\text{MC}}, \bar{Y}_{\text{d}}] + C_{\mathbf{L}}^{\hat{\phi}\hat{\phi}}[\bar{U}_{\text{MC}}, \bar{V}_{\text{d}}, \bar{X}_{\text{MC}}, \bar{Y}_{\text{d}}] \\ & \left. - C_{\mathbf{L}}^{\hat{\phi}\hat{\phi}}[\bar{U}_{\text{MC}}, \bar{V}_{\text{MC}'}, \bar{X}_{\text{MC}}, \bar{Y}_{\text{MC}'}] - C_{\mathbf{L}}^{\hat{\phi}\hat{\phi}}[\bar{U}_{\text{MC}}, \bar{V}_{\text{MC}'}, \bar{X}_{\text{MC}'}, \bar{Y}_{\text{MC}}] \right\rangle_{\text{MC}, \text{MC}'} , \end{aligned} \quad (3.71)$$

where the d subscript indicates a CMB field from the data. We subtract this RDN0 estimate from the data spectrum.

The second bias term $\Delta C_{\mathbf{L}}^{\phi\phi}\big|_{\text{N1}}$ arises from connected contributions to the trispectrum and depends linearly on $C_L^{\phi\phi}$ [70]; this term is called “N1” because it is first-order in $C_L^{\phi\phi}$. We estimate this term by creating two sets of simulations, MC and MC' , in which simulated pair has the same realization of ϕ , but different realizations of the unlensed CMB; see Section 3.3 for more detail. The N1 term is then¹¹

$$\begin{aligned} \Delta C_{\mathbf{L}}^{\phi\phi}\big|_{\text{N1}} = & \left\langle + C_{\mathbf{L}}^{\hat{\phi}\hat{\phi}}[\bar{U}_{\phi^1, \text{MC}}, \bar{V}_{\phi^1, \text{MC}'}, \bar{X}_{\phi^1, \text{MC}}, \bar{Y}_{\phi^1, \text{MC}'}] \right. \\ & + C_{\mathbf{L}}^{\hat{\phi}\hat{\phi}}[\bar{U}_{\phi^1, \text{MC}}, \bar{V}_{\phi^1, \text{MC}'}, \bar{X}_{\phi^1, \text{MC}'}, \bar{Y}_{\phi^1, \text{MC}}] \quad (3.72) \\ & \left. - \Delta C_{\mathbf{L}}^{\phi\phi}\big|_{\text{N0}} \right\rangle_{\text{MC}, \text{MC}'} \end{aligned}$$

The final term $\Delta C_{\mathbf{L}}^{\phi\phi}\big|_{\text{MC}}$ encapsulates any corrections that have not been accounted for as yet. For example, these could include higher-order bias terms beyond N0 and N1, bias from non-Gaussian foreground emission, etc. We calculate this term as the difference of the simulations from the input spectrum:

$$\Delta C_{\mathbf{L}}^{\phi\phi}\big|_{\text{MC}} = C_{\mathbf{L}}^{\hat{\phi}\hat{\phi}}_{\text{MC}} - \Delta C_{\mathbf{L}}^{\phi\phi}\big|_{\text{N0}} - \Delta C_{\mathbf{L}}^{\phi\phi}\big|_{\text{N1}} \quad (3.73)$$

We find that $\Delta C_{\mathbf{L}}^{\phi\phi}\big|_{\text{MC}}$ is small and do not subtract it in our final estimate; see Section 3.4 for further discussion.

Thus our final measured power spectrum may be written as

$$\hat{C}_{\mathbf{L}}^{\phi\phi} = C_{\mathbf{L}}^{\hat{\phi}\hat{\phi}} - \Delta C_{\mathbf{L}}^{\phi\phi}\big|_{\text{RDN0}} - \Delta C_{\mathbf{L}}^{\phi\phi}\big|_{\text{N1}}. \quad (3.74)$$

Now that we have the best estimate of our lensing power spectrum $\hat{C}_{\mathbf{L}}^{\phi\phi}$, we would like to average this spectrum into bins in L . The power in each bin is referred to as a “bandpower.” Because $\hat{C}_{\mathbf{L}}^{\phi\phi}$ is a two-dimensional quantity with varying signal-to-noise across the 2D \mathbf{L} -plane, a naive binning operation of simply averaging $\hat{C}_{\mathbf{L}}^{\phi\phi}$ in each bin is sub-optimal. Instead,

11. Note, Gaussian foreground power is not included in the simulations for N1.

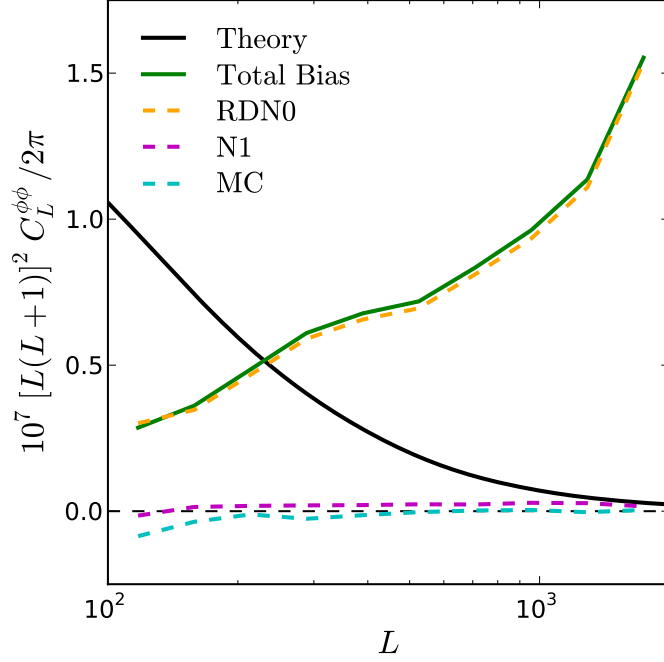


Figure 3.1: Noise-bias levels for this ϕ reconstruction. The theoretical Λ CDM lensing potential power spectrum is shown in **black**, and the individual bias terms defined in Equation 3.69 are shown individually. The realization-dependent N0 (RDN0) term (**dashed orange line**) is used to correct the data for the Gaussian noise bias (see Equation 3.71). The N1 bias (**dashed purple line**) arises from connected contributions to the CMB trispectrum (see Equation 3.72). The sum of these two terms is the total bias (**solid green line**) that we subtract. The residual Monte-Carlo (MC) bias term (**dashed cyan line**) from Equation 3.69 is calculated as the difference between the mean of de-biased lensed simulation spectra and the input spectrum to the simulations. The total bias shows the reconstruction-noise power in the reconstructed ϕ maps; thus this reconstruction measures ϕ modes with a signal-to-noise ratio greater than 1 (alternatively, the measurement is ϕ -sample-variance limited) for $100 < L \lesssim 250$.

we calculate the weighted average of $\hat{C}_{\mathbf{L}}^{\phi\phi}$ within each bin:

$$C_b^{\phi^{UV}\phi^{UV}} \equiv \frac{\sum_{\mathbf{L} \in b} w_{\mathbf{L}}^{UVXY} \hat{C}_{\mathbf{L}}^{\phi^{UV}\phi^{XY}}}{\sum_{\mathbf{L} \in b} w_{\mathbf{L}}^{UVXY}}. \quad (3.75)$$

The choice of the weight function $w_{\mathbf{L}}^{UVXY}$ follows from the same reasoning used to define the weights in Equation 3.39. Specifically, in the quadratic maximum likelihood estimator that we are using, $\mathcal{R}_{\mathbf{L}}^{XY}$ is the Fisher matrix for $\phi_{\mathbf{L}}^{XY}$; therefore the inverse-variance weight for $\hat{C}_{\mathbf{L}}^{\phi\phi}$ is the product of the normalization of the two estimates ϕ^{UV} and ϕ^{XY} :

$$w_{\mathbf{L}}^{UVXY} = \mathcal{R}_{\mathbf{L}}^{UV} \mathcal{R}_{\mathbf{L}}^{XY}. \quad (3.76)$$

This weight scheme is analytically optimal in two cases: either for an estimator of the auto-spectrum where $U = V = X = Y$ or for a complete set of cross-spectra between different estimators (e.g., the MV and POL estimators).

We calculate the amplitude A_b of our data spectrum relative to a theory spectrum within a bin b ,

$$A_b^{UVXY} \equiv \frac{C_b^{\phi^{UV}\phi^{UV}}}{C_b^{\phi^{UV}\phi^{XY}, \text{theory}}}, \quad (3.77)$$

where the binned theory spectrum is

$$C_b^{\phi^{UV}\phi^{XY}, \text{theory}} \equiv \frac{\sum_{\mathbf{L} \in b} w_{\mathbf{L}}^{UVXY} C_{\mathbf{L}}^{\phi\phi, \text{theory}}}{\sum_{\mathbf{L} \in b} w_{\mathbf{L}}^{UVXY}}. \quad (3.78)$$

We report bandpowers $\hat{C}_{L_b}^{\phi\phi}$ as the data-amplitude A_b multiplied by the theoretical spectrum $C_{L_b}^{\phi\phi, \text{theory}}$ evaluated at the bin center L_b ,

$$\hat{C}_{L_b}^{\phi\phi} \equiv A_b C_{L_b}^{\phi\phi, \text{theory}}. \quad (3.79)$$

Finally, we calculate two overall amplitudes of $\hat{C}_{\mathbf{L}}^{\phi\phi}$ relative to a theory spectrum: A_{MV} for the MV spectrum and A_{POL} for the polarization-only spectrum. These amplitudes are calculated using Equation 3.77, where the “bin” is taken to the full range $100 < L < 2000$. The reference theory spectrum $C_L^{\phi\phi, \text{theory}}$ is taken to be the PLANCK+LENS+WP+HIGHL spectrum. We additionally report the spectrum bandpowers as defined in Equation 3.79, which contain the information about the shape of our measured spectrum.

3.3 Simulations

The lensing analysis presented here relies heavily on accurate simulations. We use the spectra from the PLANCK+LENS+WP+HIGHL model as our fiducial cosmological model for simulations. We create simulations as follows.

First, we create realizations of spherical-harmonic coefficients (a_{lm}) for the CMB fields T , E , and B (including the proper correlations between the fields), as well as the lensing potential ϕ . We simulate modes with $\ell < 6000$. We evaluate the spherical harmonic transform¹² of the a_{lm} coefficients on a grid with an equidistant cylindrical projection (ECP) [79]. The lensing operation is applied by distorting the unlensed fields using the deflection map derived from ϕ . These distorted maps are interpolated back onto a fixed ECP grid, creating lensed CMB skies with full non-Gaussian information.

These maps are then mock-observed with the map-making pipeline. This involves creating simulated TOD for each bolometer, filtering the TOD, accumulating the TOD into flat-sky maps using the SPT pointing information, and coadding different detectors based on the individual detector weights. In effect, the resulting maps are what SPT would have seen if these simulated skies had been the true CMB sky, in the absence of noise and foregrounds.

The mock-observed maps are transformed back into Fourier space, where Gaussian fore-

12. The spherical harmonic transform is performed with routines from the HEALPIX library [49].

ground power is added. We use the foreground model from [129], with the following components: $D_{3000}^{\text{PS}} = 10\mu\text{K}^2$ is the power from Poisson-distributed point-sources that scales as $D^{\text{PS}} \propto \ell^2$, $D_{3000}^{\text{CL}} = 5\mu\text{K}^2$ is the power from clustered CIB sources that scales as $D^{\text{CL}} \propto \ell^{0.8}$, $D_{3000}^{\text{SZ}} = 5\mu\text{K}^2$ is the amplitude of the tSZ power spectrum that we use to scale the thermal SZ template taken from [116]. The three coefficients here are given at $\ell = 3000$. See Section 6.1 of [129] for details. The Fourier-space maps are multiplied by the Fourier-space SPT beam F_{ℓ}^{beam} .

We then add realizations of noise to the simulations. These realizations are estimated directly from the data, as described in section 3.1.2.

We make three sets of simulations:

1. Set “A”: 500 lensed simulations.
2. Set “B”: 100 lensed simulations with different realizations of the CMB but the *same* realizations of ϕ as the first 100 simulations in Set A.
3. Set “C”: 500 unlensed simulations.

These simulations are used as follows. The simulations in set “A” are used to calculate the mean-field (see Section 3.2.2), the N0 bias term (see Section 3.2.4), and the statistical uncertainty (see Section 3.4). Specifically, the first 100 simulations are used to calculate the mean-field; in each cross-spectrum we use the first 50 simulations to estimate the mean-field of the first ϕ and the second 50 simulations to estimate the mean-field of the second ϕ . The remaining 400 simulations are used to calculate the statistical uncertainty on the lensing spectrum and amplitude. The entire set is used to calculate $\Delta C_{\mathbf{L}}^{\phi\phi}\big|_{\text{RDN0}}$.

The simulations in set “B” are used to calculate $\Delta C_{\mathbf{L}}^{\phi\phi}\big|_{\text{N1}}$, as described in Equation 3.72. Specifically, the simulations labeled MC are comprised of 50 simulations from set “A”, while the simulations labeled MC' come from 50 matching simulations from set “B”.

Finally, the unlensed simulations that comprise set “C” are used for two purposes. First, we check that no spurious lensing in our pipeline is detected by measuring the amplitude of

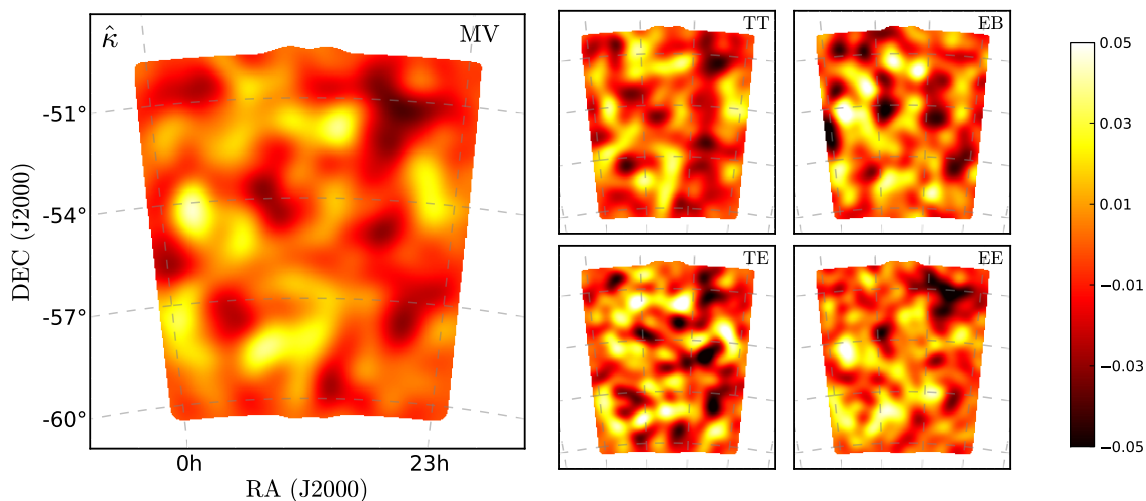


Figure 3.2: Lensing κ maps reconstructed from the SPTpol 100 deg² deep-field data, smoothed with a 1-degree Gaussian beam. The colorbar on the far right shows the color scale, which has been fixed for all κ maps in Figures 3.2 and 3.3. **Left:** The κ -map for our MV lensing estimator, which combines all temperature and polarization information. **Right:** Individual κ estimates from the TT, EB, TE, and EE estimators, with the same color scale.

the reconstructed lensing potential from these unlensed simulations. The average amplitude and variance of these simulations is $A_{\text{unl}} = -0.024 \pm 0.065$, thus passing this test. Second, we quantify how significantly we reject the no-lensing hypothesis by comparing the lensing amplitude measured in the data to the variance of these unlensed simulations. The first 100 simulations are used to calculate the mean-field, and the remaining 400 simulations are used to calculate the statistical uncertainty of unlensed skies.

In Figure 3.7, the distribution of lensing amplitudes from these lensed simulations is shown in green, and the distribution for unlensed simulations is shown in red.

3.4 Uncertainty budget

The uncertainties on the lensing spectrum and amplitude are comprised of variance (noise and sample), calibration and beam error, and other systematic errors. The variance component is calculated as the covariance between the power spectra of 400 lensed simulations.

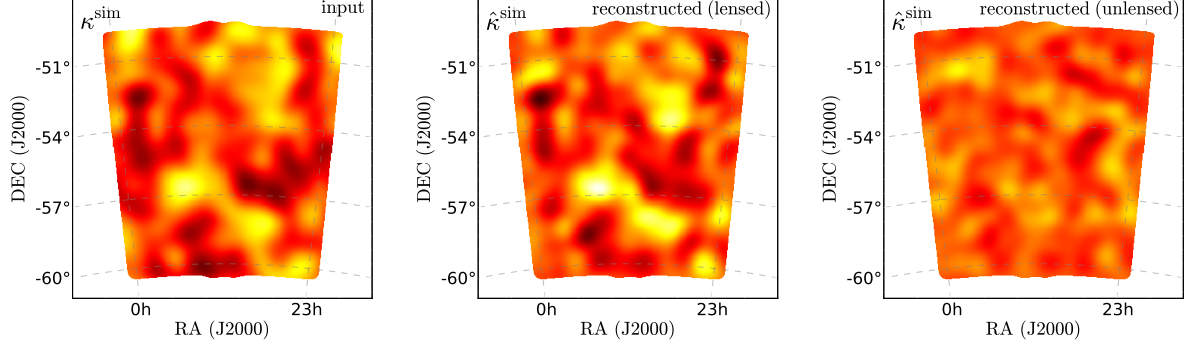


Figure 3.3: Example simulated κ -maps, plotted with the same color scale as Figure 3.2. **Left:** a simulated input κ -map. **Middle:** the reconstructed κ -map estimated from a noisy simulation that has been lensed using the potential shown in the left panel. **Right:** the reconstructed κ -map estimated from an unlensed simulation. Comparing the reconstructed lensed κ -map to the input map gives a visual sense of the fidelity of this reconstruction, and comparing to the unlensed κ -map gives a sense of the signal-to-noise in the MV κ -map.

Table 3.2: Systematic Uncertainties

Type	ΔA_{MV}	ΔA_{POL}
ΔA_{Tcal}	0.052	0.052
ΔA_{Pcal}	0.030	0.067
ΔA_{xtalk}	0.05	0.06
ΔA_{amp}	0.029	0.039
ΔA_{tot}	0.08	0.11

Table 3.3: The contributions to the systematic uncertainty budget. The quadrature sum of the systematic uncertainty terms gives the total systematic uncertainty, ΔA_{tot} .

These simulations use independent realizations of the unlensed CMB, lensing potential, and instrumental noise, thus this procedure naturally accounts for both instrumental noise and sample variance.

We also account for sources of systematic uncertainty. The resulting uncertainty on the lensing amplitude is calculated below and shown in Table 3.3.

3.4.1 Beam and Absolute Calibration

The estimation of the beam and absolute calibration contributes additional systematic uncertainty. The fractional uncertainties on the beam measurements are less than 1% over the multipoles used in this analysis, and the resulting uncertainty on the lensing amplitude is negligible. The 1σ uncertainty on the absolute calibration in temperature is $\delta T_{\text{cal}} = 1.3\%$ (C14). This will propagate into an uncertainty on the spectrum amplitude of $\Delta A_{\text{Tcal}} = A(1 + \delta T_{\text{cal}})^4$. We thus incorporate a systematic uncertainty on the amplitude from calibration and beams of $\Delta A_{\text{Tcal}} = 0.052$.

3.4.2 Polarization Calibration

Similarly, an error in the polarization calibration will propagate to an uncertainty on the spectrum amplitude of polarized estimators. We estimate the 1σ uncertainty on the polarization calibration to be $\delta P_{\text{cal}} = 1.7\%$ (C14). We incorporate a systematic uncertainty on the POL amplitude of $\Delta A_{\text{POL}}^{\text{Pcal}} = 0.067$. We estimate the resulting systematic uncertainty in the MV amplitude by calculating the relative change in the analytic normalization $\mathcal{R}_{\text{L}}^{\text{POL,Analytic}}$ resulting from a 1σ shift in P_{cal} . We find an uncertainty in the MV amplitude of $\Delta A_{\text{MV}}^{\text{Pcal}} = 0.030$.

3.4.3 *Temperature-to-Polarization Leakage*

Mis-estimating the temperature power leaked into Q and U maps would bias the lensing measurement. We recalculate the MV lensing amplitude without correcting for the leakage. The amplitude changes by less than 0.07σ ; this source of uncertainty is negligible.

3.4.4 *Electrical crosstalk between detectors*

There is some low-level electrical crosstalk between detectors. The main effect of crosstalk is to introduce a difference between the temperature and polarization instrumental beams, resulting in a small multiplicative bias in the polarization measurements; see C14 for a detailed discussion. The effect of crosstalk on this lensing analysis was investigated using the simulation pipeline described in Section 3.3 and adding the effect of crosstalk to the simulated timestreams. We find that crosstalk introduces a small bias in the lensing amplitude, which we estimate to be a 5% (6%) in the MV (POL) amplitude; we account for this by adding a contribution to our systematics uncertainty budget of $\Delta A_{MV}^{\text{xtalk}} = 0.05$ and $\Delta A_{POL}^{\text{xtalk}} = 0.06$. The bias in the data from crosstalk is expected to be smaller than this estimate, because the data uses an RDN0 bias subtraction that reduces the effect of a mismatch between the power in the simulations relative to the data itself. In contrast, these simulations use a normal N0 bias subtraction, rather than recalculating an RDN0 bias for each simulation. We keep this over-estimate of the crosstalk-induced bias and include this term in our systematic uncertainty budget. In future analyses, we plan to characterize and remove crosstalk from individual detector timestreams.

3.4.5 *Foregrounds*

Foreground emission from extra-galactic sources and galactic dust contributes both Gaussian power and non-Gaussian signal to CMB observations which, if not accounted for, will bias lensing reconstruction measurements. The Gaussian power component contributes to the

N0 bias, which we subtract using the simulations described in Section 3.3 and procedure described in Section 3.2.4.

The non-Gaussian mode-coupling from foreground emission has been studied in detail in [130, hereafter V14], and [92]. The work in V14 is particularly relevant to our analysis. They studied a comprehensive list of potential biases to the temperature lensing reconstruction that arise from foregrounds; they considered Poisson-distributed galaxies, CIB emission from clustered galaxies, tSZ signal from galaxy clusters, galaxy-lensing correlations, and tSZ-lensing correlations. For the point-source and cluster masking thresholds used in our analysis, the bias to the lensing spectrum never exceeds a few percent. [131] also tested diffuse Galactic cirrus emission and found that the bias was less than 2% in all L -bins.

The contribution to the N0 bias from polarized foregrounds is negligible at the sensitivity level of this analysis since the polarized power from point sources is too low to be detected significantly in the EE and TE polarization spectra in C14, even with the significantly higher flux cut of 50 mJy in that work. The non-Gaussian signature of polarized foregrounds is expected to be negligible as well: the polarization fraction of foreground emission is expected to be lower than the polarization fraction of the CMB, implying that the ratio of non-Gaussian foreground signal to CMB lensing signal will be lower in polarization than temperature, and the non-Gaussian contribution in temperature has already been shown to be negligible for this analysis.

Finally, we consider whether emission from polarized Galactic dust could contaminate the polarized lensing estimators. The Gaussian power in B modes from Galactic dust within the BICEP2 field was estimated in a joint analysis of BICEP2 and *Planck* data [11]; because the BICEP2 field contains the SPTpol deep field, this analysis provides a good estimate of Galactic dust in the SPTpol data. The best-fit model from the joint analysis is $D^{\text{dust}}(\ell) = D_{\ell=80}^{\text{dust}} \times (\ell/80)^{-0.42}$, where $D_{\ell=80}^{\text{dust}} = 0.0118 \mu\text{K-arcmin}$. Using this model, the dust power in this field is $\sim 10\%$ of the lensed B -mode power and $\sim 1\%$ of the B -mode noise power (as calculated in [68]) at the lowest multipoles used in the SPTpol lensing analysis ($\ell > 450$), and

the dust power drops rapidly with increasing ℓ . Thus we conclude that the Gaussian power from Galactic dust in our polarized maps has a negligible contribution to both our observed signal and variance. Significant non-Gaussian contributions from any foreground sources, including Galactic dust, should cause a failure of the curl test since foregrounds should contain both gradient and curl modes. Both the MV and POL estimators pass the curl test, thus we conclude that Galactic dust does not contribute significantly to the observed lensing signal in either temperature or polarization.

We conclude that given the level of precision of this analysis and our level of source masking, the RDN0 bias correction sufficiently accounts for the Gaussian power from unpolarized foregrounds, and that the Gaussian power from polarized foregrounds can be neglected in the RDN0 term. Furthermore, we conclude that the biases due to the non-Gaussian contribution from polarized and unpolarized foregrounds are negligible at the level of statistical precision of the current analysis.

3.4.6 Normalization Calculation

We find that the mean MV (POL) amplitude of our lensed simulations is 3% (4.5%) below unity; this can be seen as a shift in the histogram of lensed simulations in Figure 3.7. This bias could be an additive term (e.g., the $\Delta C_{\mathbf{L}}^{\phi\phi}|_{\text{MC}}$ term from Equation 3.69) or a multiplicative term (e.g., mis-estimation of the power-spectrum normalization). We treat this potential bias as a systematic uncertainty in our analysis of $\Delta A_{\text{MV}}^{\text{amp}} = +0.029$ and $\Delta A_{\text{POL}}^{\text{amp}} = +0.039$ on the MV and POL amplitudes, respectively.

3.4.7 Total Uncertainty

The four sources of significant systematic error described above are added in quadrature to calculate our final systematic uncertainty on the lensing amplitude: $\Delta A_{\text{MV}} = \pm 0.08$ and $\Delta A_{\text{POL}} = \pm 0.11$ on the amplitudes of the MV and POL spectra, respectively. Thus our uncertainty on the amplitude of the MV lensing power spectrum is $\Delta A_{\text{MV}} = \pm 0.14 (\text{Stat.}) \pm$

0.08 (Sys.), and our uncertainty on the amplitude of the POL lensing power spectrum is $\Delta A_{\text{POL}} = \pm 0.24 \text{ (Stat.)} \pm 0.11 \text{ (Sys.)}$,

Finally, we calculate a total uncertainty by adding the statistical and systematic uncertainties in quadrature: $\Delta A_{\text{MV}}^{\text{tot}} = \pm 0.16$ and $\Delta A_{\text{POL}}^{\text{tot}} = \pm 0.26$.

3.5 Results

We present three main results in this section: the MV map of the lensing convergence field, $\kappa(\hat{\mathbf{n}})$, the MV and POL estimates of the binned lensing potential power spectrum, and the amplitudes of these two spectra relative to the PLANCK+LENS+WP+HIGHL model.

3.5.1 Lensing Potential Map

We show measured lensing convergence maps¹³ $\kappa(\hat{\mathbf{n}})$ in Figure 3.2. These κ -maps are the real-space equivalent of $(1/2)L(L+1)\hat{\phi}_{\mathbf{L}}$, where $\hat{\phi}_{\mathbf{L}}$ is defined in Equation 3.38. We show the MV map, as well as four of the five individual estimators. The similarities between the different estimators are visually apparent.

We measure lensing modes with a signal-to-noise ratio greater than one for modes between $100 < L < 250$; thus the large-scale features that are visible by eye are real over-densities and under-densities in the projected mass distribution in the universe. This is the highest signal-to-noise lensing map from the CMB to date.

3.5.2 Lensing Potential Power Spectrum

Here we present the bandpowers from our estimate of the lensing potential power spectrum. We report the bandpowers between $100 < L < 2000$. The lower boundary is set at 100 to maximize the signal while keeping the *MC* bias sub-dominant to other systematic uncertain-

13. The map is presented as κ because this corresponds visually to the density of the integrated matter field along the line of sight: $\kappa > 0$ corresponds to an over-density that “stretches” the observed CMB pattern, while $\kappa < 0$ corresponds to an under-density that “contracts” the observed CMB pattern.

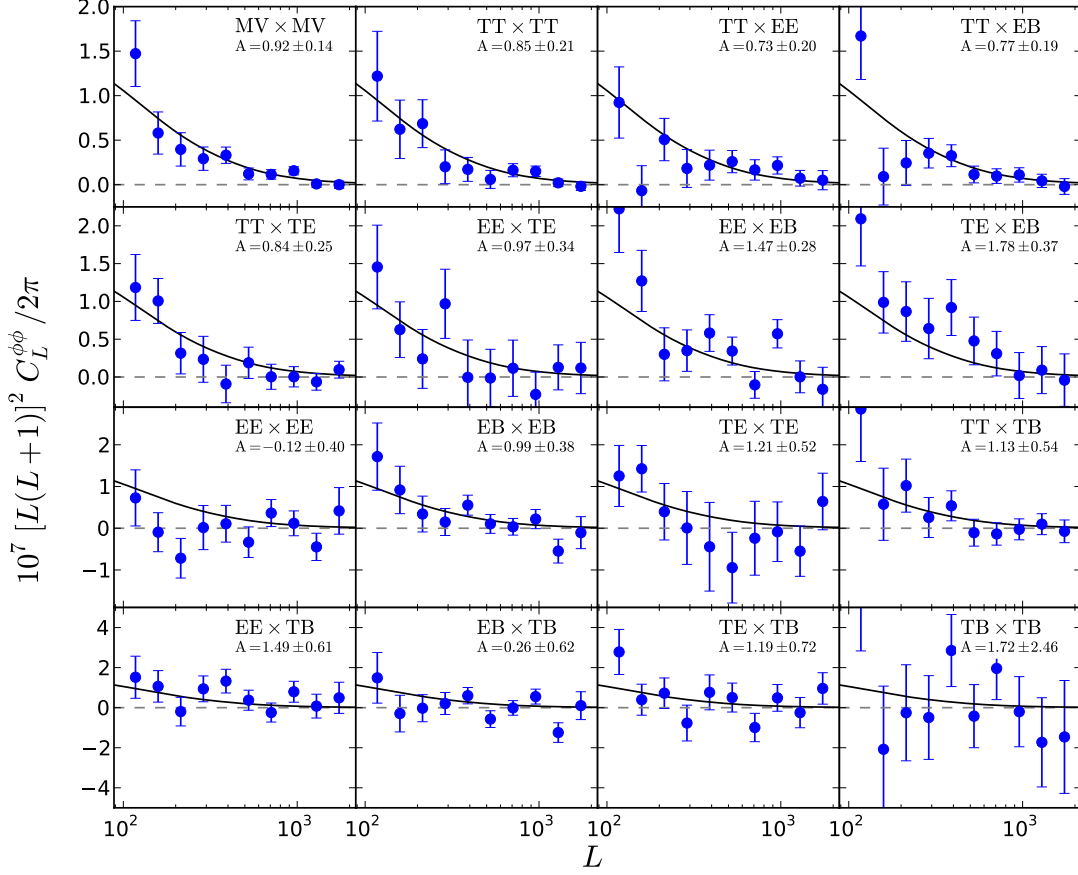


Figure 3.4: The $\hat{C}_{L_b}^{\phi\phi}$ power spectra for all estimators we consider in this chapter. “MV \times MV” is the spectrum from the minimum-variance estimator. The amplitudes of each spectrum relative to the fiducial PLANCK+LENS+WP+HIGHL model are calculated with Equation 3.77 and shown in each panel.

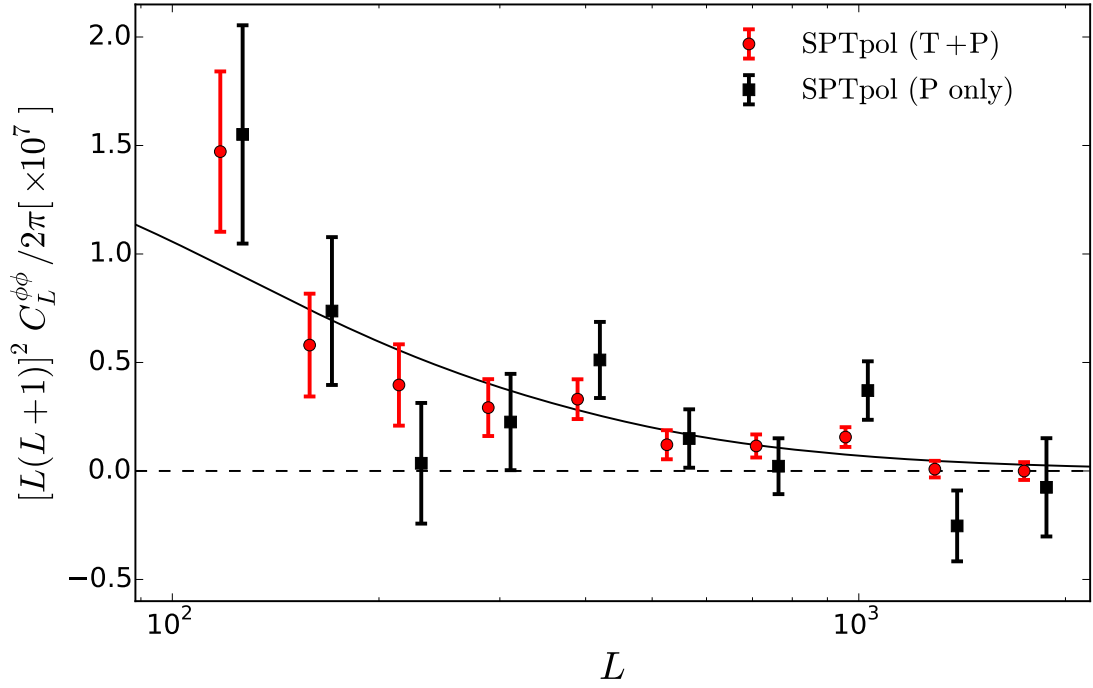


Figure 3.5: Lensing potential power spectrum bandpowers estimated from SPTpol. The MV and POL spectra are shown with red circles and black squares, respectively. The black solid line shows the PLANCK+LENS+WP+HIGHL best-fit Λ CDM model. Note the POL points have been shifted by 1/4 of a bin in L for plotting purposes.

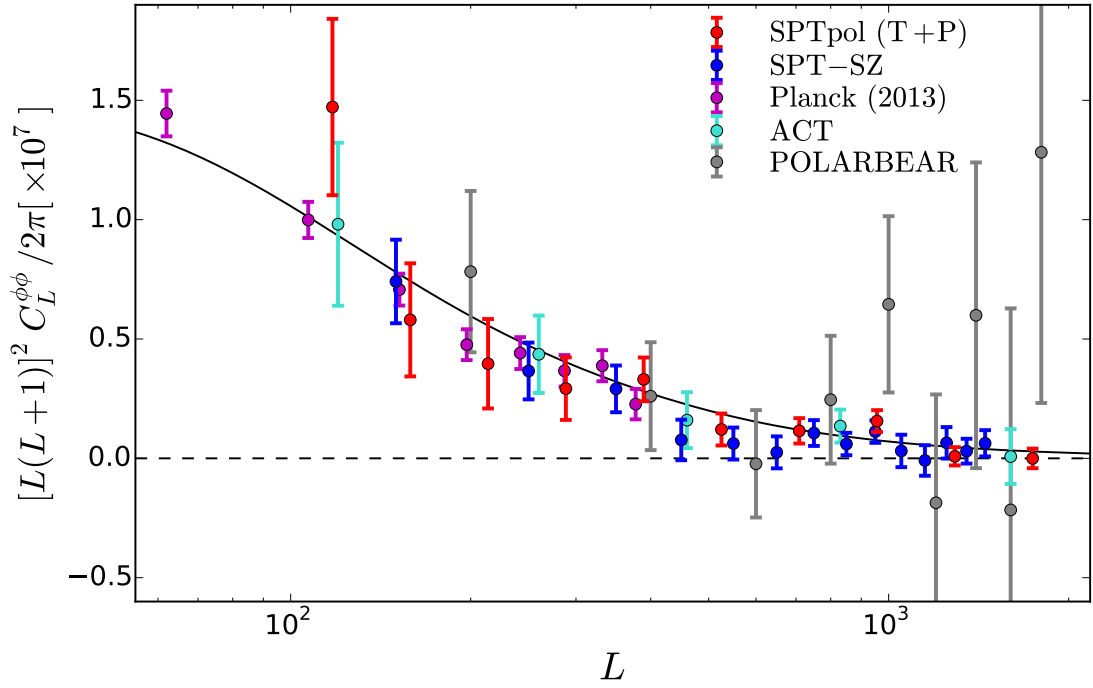


Figure 3.6: Lensing potential power spectrum bandpowers estimated from SPTpol, as well as those previously reported for temperature by SPT-SZ [131], ACT [30], *Planck* [101], and for polarization by POLARBEAR ([104]). The black solid line shows the PLANCK+LENS+WP+HIGHL best-fit Λ CDM model.

ties; the MC bias increases as this lower boundary is reduced. The upper boundary is deep in the noise-dominated region of the spectrum; we find that the statistical uncertainty on the lensing spectrum amplitude is roughly constant for any boundary value above $L \gtrsim 1000$ and $L \gtrsim 800$ for the MV and POL estimators, respectively. We calculate the cross-spectrum from each pair of estimators $[\hat{\phi}_{\mathbf{L}}^{UV}, \hat{\phi}_{\mathbf{L}}^{XY}]$, as well as two minimum-variance estimates, $\hat{C}_{L_b}^{\text{MV}}$ from the combination of all estimators, and $\hat{C}_{L_b}^{\text{POL}}$ from the polarization-only estimators EE , EB , and BE . The cross-spectra between each pair of these lensing potential estimators is shown in Figure 3.4.

The MV spectrum $\hat{C}_{L_b}^{\text{MV}}$ and POL spectrum $\hat{C}_{L_b}^{\text{POL}}$ are shown in Figure 3.5. The band-powers for the MV spectrum are presented in Table 3.5. We measure the amplitude of the spectrum using Equation 3.77 relative to the PLANCK+LENS+WP+HIGHL model. We find an amplitude of $A_{\text{MV}} = 0.92 \pm 0.14 (\text{Stat.}) \pm 0.08 (\text{Sys.})$ for the combined spectrum and $A_{\text{POL}} = 0.92 \pm 0.24 (\text{Stat.}) \pm 0.11 (\text{Sys.})$ for the polarization-only spectrum. Thus we measure the amplitude of the lensing potential power spectrum using solely polarization estimators with a precision of 26%; including systematic errors, this becomes a precision of 29%. Similarly, the precision of the MV measurement of the amplitude is 15%; including systematic errors, this becomes a precision of 18%.

We quantify how significantly we reject the null hypothesis of no lensing by comparing the data to unlensed simulations. In 400 unlensed simulations, none have a lensing amplitude as large as that in the data in either the MV or POL estimator. To estimate statistical significance, we fit a Gaussian to the 400 unlensed simulations, yielding a 14σ and 5.9σ rejection of the null hypothesis for the MV and POL estimators, respectively.

Figure 3.7 demonstrates the difference between these constraints. We rule out the no-lensing hypothesis much more significantly than the precision with which we measure the amplitude of the lensing spectrum (14σ vs. $15\% \sim 6.5\sigma$). This difference indicates that we measure the presence of lensing modes very significantly, however, the measurements are sample-variance dominated on large scales, limiting the precision of our constraint on the

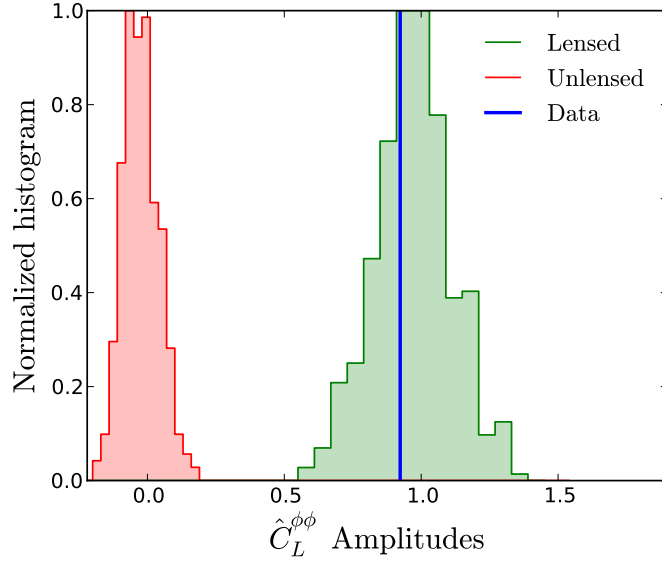


Figure 3.7: The distribution of reconstructed MV lensing amplitudes from simulations are shown here for lensed (green) and unlensed (red) simulations. The amplitude of the MV estimate for the data is shown as a blue line. The statistical uncertainty of the MV lensing construction is given by the standard deviation of the lensed simulations ($\Delta A_{\text{MV}} = 0.14$). The significance with which we rule out the no-lensing hypothesis is calculated from the standard deviation of the unlensed simulations (0.065).

lensing power spectrum amplitude.

We plot the MV spectrum in comparison with other measurements in Figure 3.6. All spectra are visually consistent at the current sensitivity levels; we discuss these measurements in Section 3.7. We compare our MV spectrum amplitude directly to the most precise of these measurements (*Planck*) by recalculating the MV amplitude relative to the same fiducial spectrum used in [101]. *Planck* measured an amplitude of $A_{\text{Planck}} = 0.94 \pm 0.04$; we find an amplitude relative to the same cosmology of $A_{\text{MV}}^{\text{Planck-Fiducial}} = 0.90 \pm 0.16$, which is consistent.

Table 3.4: MV lensing bandpowers

$[L_{\min} \quad L_{\max}]$	L_b	$10^7 [L_b(L_b + 1)]^2 \hat{C}_b^{\phi\phi} / 2\pi$
[100 133]	117	1.47 ± 0.37
[134 181]	158	0.58 ± 0.24
[182 244]	213	0.40 ± 0.19
[245 330]	288	0.29 ± 0.13
[331 446]	389	0.331 ± 0.092
[447 602]	525	0.121 ± 0.067
[603 813]	708	0.115 ± 0.053
[814 1097]	956	0.156 ± 0.046
[1098 1481]	1290	0.008 ± 0.038
[1482 1998]	1741	-0.000 ± 0.041

Table 3.5: The bandpowers for the MV spectrum are presented here as defined in Equation 3.79 and shown in Figures 3.5 and 3.6. Bins are evenly spaced in $\log(L)$, and bandpowers are reported at the center of each bin.

Table 3.6: MV Systematic Error and Null tests

Test Name	χ^2	(PTE)	ΔA_{MV} $\pm \text{var}(\Delta A_{\text{MV, sim}})$	(PTE)
L-R jackknife	7.1	(0.72)	0.0040 ± 0.0052	(0.45)
$l_{\text{xmin}} = 400$	17.5	(0.06)	-0.063 ± 0.030	(0.025)
$l_{\text{xmin}} = 500$	10.7	(0.38)	0.053 ± 0.033	(0.10)
$l_{\text{max}} = 2500$	13.6	(0.19)	-0.122 ± 0.107	(0.26)
$l_{\text{max}} = 3500$	9.2	(0.51)	0.007 ± 0.067	(0.91)
Apodized Mask	13.6	(0.19)	-0.043 ± 0.034	(0.22)
C-inverse	9.6	(0.47)	0.146 ± 0.534	(0.78)
Curl	7.4	(0.69)	0.082 ± 0.092	(0.39)

Table 3.7: Results of systematics tests. For each test, the χ^2 and PTE of the $C_L^{\phi\phi}$ spectrum are shown in the second column. The change in amplitude and associated PTE are shown in the third column. See Equation 3.80 for more detail. The $l_{\text{xmin}} = 400$ test fails, which is why we place the cut higher, at $l_{\text{xmin}} = 450$ in the analysis.

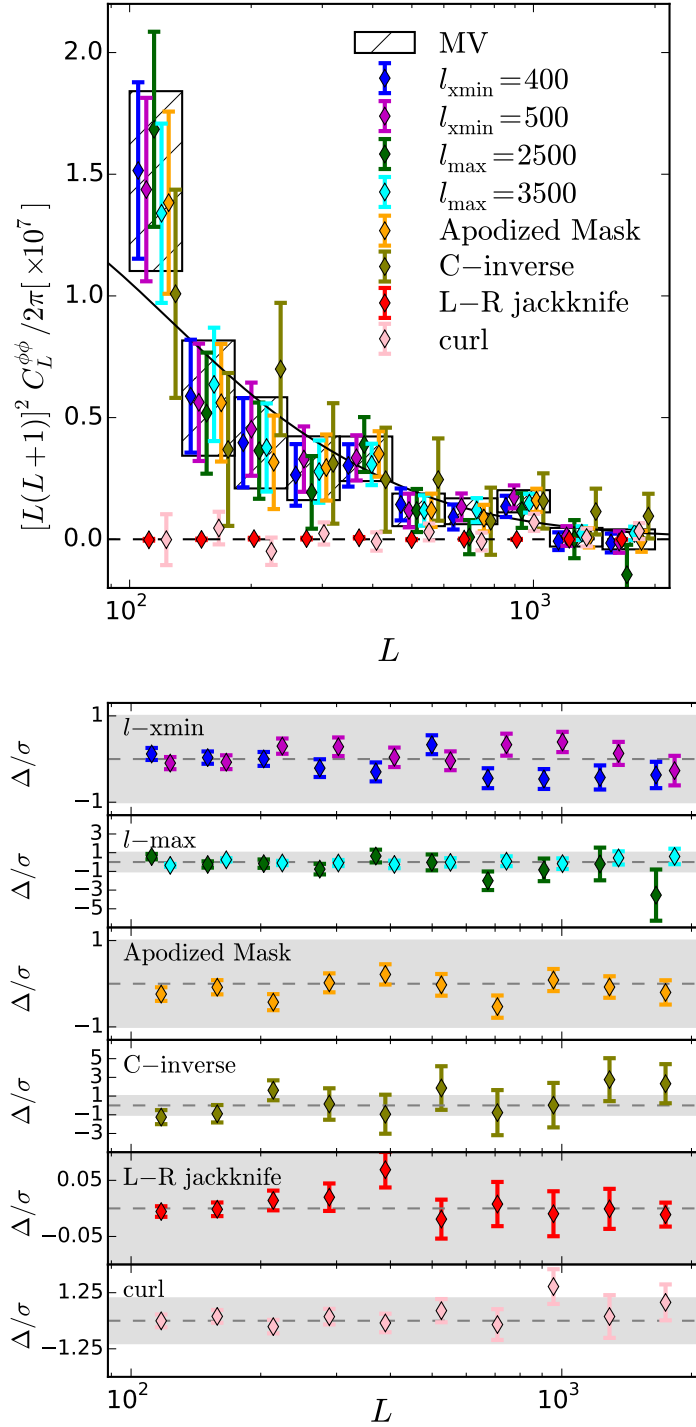


Figure 3.8: Power spectrum consistency tests. The **upper panel** shows the spectrum of each consistency test. The **lower panels** show the same set of consistency tests, plotted as the difference between each consistency test relative to the fiducial spectrum, divided by the 1σ statistical error bar of the MV spectrum. Note that the statistical uncertainty on these difference-spectra will be a function of the analysis and not necessarily the same as for the baseline MV spectrum. The grey band in each of the lower panels shows the 1σ statistical uncertainty region. The error bars shown in the lower panels are calculated from the variance in simulations of each consistency test.

3.6 Systematic Error Checks

We perform a suite of tests for systematic errors in our data. For each test, we change one aspect of the analysis and recalculate the lensing spectrum ($C_b^{\phi\phi}$ sys) and amplitude ($A_{\text{MV,sys}}$). We then calculate the difference between this spectrum (or amplitude) and the spectrum (or amplitude) from the baseline analysis (the baseline spectrum and amplitude are the MV results we report in Section 3.5). The difference-spectrum $\Delta C_b^{\phi\phi}$ and difference-amplitude ΔA_{MV} are the shifts induced in the spectrum and the amplitude, respectively, by the systematic under consideration; they can be expressed as

$$\Delta C_b^{\phi\phi} = C_{b,\text{sys}}^{\phi\phi} - C_b^{\phi\phi} \quad (3.80)$$

$$\Delta A_{\text{MV}} = A_{\text{MV,sys}} - A_{\text{MV}}. \quad (3.81)$$

The difference-spectra and difference-amplitudes are calculated for the data as well as for each simulation.

For each test, we use two metrics to determine if the data pass the test; these metrics are shown in Table 3.7. The first metric considers shifts in the lensing spectrum. We calculate the χ^2 of the data difference-spectrum ($\Delta C_{b,\text{data}}^{\phi\phi}$) using the variance of the simulation difference-spectra ($\sigma_{b,\text{sys}}$) as the uncertainty. This can be expressed as

$$\chi_{\text{sys}}^2 = \sum_b \frac{(\Delta C_{b,\text{data}}^{\phi\phi})^2}{\sigma_{b,\text{sys}}^2}. \quad (3.82)$$

The probability-to-exceed (PTE) of this χ^2 is calculated from a χ^2 distribution with 10 degrees of freedom (corresponding to the 10 bins in our spectrum).

The second metric considers the change in the lensing amplitude. We calculate the lensing difference-amplitudes (ΔA_{MV}) as defined in Equation 3.80 for the data and for each simulation. We then calculate the variance of the simulation difference-amplitudes ($\text{var}(\Delta A_{\text{MV,sim}})$); this variance estimates the expected magnitude of the change in the lensing

amplitude. Specifically, we expect the magnitude of the lensing difference-amplitude in the data to be less than or equal to $\sqrt{\text{var}(\Delta A_{\text{MV, sim}})}$ in $\sim 68\%$ of similar measurements. Finally, we calculate the PTE of the data difference-amplitude directly from the simulations as the percentage of simulations that have a difference-amplitude with a larger magnitude than ΔA_{MV} for the data. The data difference-amplitude, variance of simulated difference-amplitudes, and PTEs for each test are shown in Table 3.7.

The individual tests are described in detail below, and the results are reported in Table 3.7 and Figure 3.6.

1. **ℓ_{min} cut:** As described in Section 3.1, we cut all modes with $|\ell_x| < 450$ from the CMB maps. In this test, we adjust that cut from $|\ell_x| < 450$ to 400 and 500. When more ℓ -space is removed by increasing the $|\ell_x|$ cut to 500, the change in the lensing spectrum and amplitude are consistent with expectations from simulations. On the other hand, including the region between $400 < |\ell_x| < 450$ causes an unexpectedly large shift ($> 2\sigma$) in the lensing amplitude, thus motivating the placement of this cut. Even in this case, however, the change in the amplitude is only 0.4σ with respect to the statistical uncertainty on the lensing spectrum amplitude.
2. **ℓ_{max} cut:** We adjust the maximum value of ℓ from CMB maps that is used in the estimator from $\ell < 3000$ to 2500 and 3500. This corresponds to adjusting the upper bound of the integral in Equation 3.31. We find the data are consistent with the expectation from simulations in this test.
3. **Apodized Mask:** We apodize the sky and point-source mask with a cosine profile on the edges, and recalculate the amplitude and $C_L^{\phi\phi}$. The change in amplitude is consistent with the expectation from simulations.
4. **C-inverse test:** We recalculate the MV spectrum and amplitude using the diagonal approximation to the C-inverse filter (e.g., \mathcal{F}_ℓ^X from Equation 3.33). The covariance of the simulations increases by a factor of four over the nominal covariance (due in part

to the fact that the C-inverse filter effectively apodizes the map, while the diagonal approximation is just an inverse-variance filter with no apodization), but the shift in the lensing amplitude is consistent with the shift of the simulations.

5. **Curl test:** We replace the gradient estimator with a curl estimator that is optimized for curl-like sources [27]. Specifically, we use the curl estimators specified in Table 3 of [91]. We estimate and remove the N0 contribution to the curl estimator as in Equation 3.72; thus the curl test provides a second check of the N0 estimation procedure. A non-zero curl signal would indicate contamination in the nominal gradient reconstruction from non-Gaussian secondary effects or foregrounds [27]. We calculate the curl signal, and find it to be consistent with the expectation from simulations in both the MV estimator ($\Delta A_{\text{MV}} = 0.082 \pm 0.092$, $C_L^{\phi\phi}$ Spectrum PTE = 0.69) and the POL estimator ($\Delta A_{\text{POL}} = 0.055 \pm 0.110$, $C_L^{\phi\phi}$ Spectrum PTE = 0.52).
6. **Scan Direction:** We perform a “jackknife” null test on the telescope scan direction. This test is sensitive to any systematic differences between left-going vs. right-going scans. We calculate null maps by subtracting all left-going scans from all right-going scans. The resulting maps should be free from signal but still contain any systematic difference between left-going and right-going maps. Because this is a null test, we calculate the pass-fail metrics for the jackknife spectrum and amplitude relative to zero (rather than relative to the MV spectrum and amplitude). Formally, this means replacing the baseline spectrum $C_b^{\phi\phi}$ and amplitude A_{MV} in Equation 3.80 with zeros, and using noise-only simulations. We find that the null spectrum and amplitude are consistent with noise.

Finally, we compare the spectra and amplitudes from each of the estimators with those from the MV spectrum. We find that the spectra are mostly consistent. The “TExEB” spectrum amplitude is high by $\sim 2.1\sigma$ relative to the expectation from simulations, while the “EExEE” spectrum amplitude is low by $\sim 2.8\sigma$. All other spectra are consistent to

within 2σ .

3.7 Discussion

In this chapter, we have presented a measurement of the CMB lensing potential ϕ from 100 deg^2 of sky observed in temperature and polarization with SPTpol. Using a quadratic estimator analysis including polarization information, we have constructed a map of the lensing convergence field. Individual Fourier modes in this map are measured with signal-to-noise greater than one in the angular wavenumber or multipole range $100 < L < 250$. This represents the highest signal-to-noise map of the integrated lensing potential made from the CMB to date. The power spectrum of the lensing potential $C_L^{\phi\phi}$ was calculated from these maps. We have verified that this measurement is robust against systematics by performing a suite of systematics and null tests.

We compare this measurement to a fiducial spectrum taken from the PLANCK+LENS+WP+HIGHL best-fit Λ CDM model and find a relative amplitude of $A_{\text{MV}} = 0.92 \pm 0.14 \text{ (Stat.)} \pm 0.08 \text{ (Sys.)}$. This corresponds to a 18% measurement of the amplitude. This measurement rejects the no-lensing hypothesis at 14σ . If instead only polarized estimators are used, we find $A_{\text{POL}} = 0.92 \pm 0.24 \text{ (Stat.)} \pm 0.11 \text{ (Sys.)}$. This is a 29% measurement of the amplitude. This measurement rejects the no-lensing hypothesis using polarization information only at 5.9σ . The MV and POL amplitudes are consistent at 0.47σ and 0.32σ , respectively, with the best-fit Λ CDM cosmology of the PLANCK+LENS+WP+HIGHL dataset. The PTE of the χ^2 relative to this theory spectrum for the MV and POL spectra are 0.49 and 0.10, respectively. The PTEs for all individual estimators are nominal, with a max/min values of 0.96 and 0.16, respectively. Of note, the bandpowers are consistent with the Λ CDM theory prediction even at high- L , where non-linear structure growth or contamination from foregrounds are more relevant.

We also compare the amplitude of our measured lensing spectrum relative to other cosmologies. Within the context of a given cosmological model, the true amplitude of the lensing

spectrum is by definition unity; any statistically significant deviation of the measured value of A_{lens} from unity indicates tension with the assumed cosmological model. Replacing our fiducial lensing spectrum with the lensing spectrum derived from the Λ CDM model that best fits the WMAP9+SPT-SZ dataset (a combination of *WMAP*9 data [54] and temperature power spectrum from [129]), the best-fit amplitude is $A_{\text{MV}}^{\text{WMAP9+SPT}} = 1.05$. This represents a shift of $\sim 13\%$, or $\sim 1\sigma$ (statistical-only) from the best-fit value assuming our fiducial cosmology. The current SPTpol measurement is consistent with the predictions of both cosmologies and cannot distinguish between them.

In comparison with previous quadratic estimator measurements from SPT and ACT, which used roughly six times the sky area ($\sim 600 \text{ deg}^2$), we have measured the lensing potential with similar precision¹⁴: 18% in this measurement, as compared to 19% from a previous SPT measurement [131] and 22% from an ACT measurement [30]. The precision of our measurement, however, is limited by sample-variance of the lenses themselves; as a result, our measurement rules out the no-lensing hypothesis much more significantly, at 14σ in our MV measurement. For comparison, no lensing was ruled out at 6.3σ in [131] (although the sample variance was scaled as a function of A_L in that calculation) and at $> 4.6\sigma$ in [30] (where sample variance was included). The temperature measurement from *Planck* is derived from over 70% of the sky and thus has much lower sample variance. At 25σ it is highly significant, although no modes are measured with a signal-to-noise ratio greater than one [101]. Our measurement is consistent with that from *Planck*; we calculate the MV amplitude relative to the same fiducial cosmology used in [101], and find an amplitude of $A_{\text{MV}}^{\text{Planck-Fiducial}} = 0.90 \pm 0.16$, which is consistent with the measurement from *Planck* of $A_{\text{Planck}} = 0.94 \pm 0.04$. Finally, our polarization-only measurement improves on the sensitivity achieved by POLARBEAR: the SPTpol POL spectrum rules out no-lensing at 5.9σ , as compared to 4.2σ from [104].

Because of the high signal-to-noise of the SPTpol measurement presented here and the

14. The fractional precision is reported relative to the mean of each measurement.

fact that the BICEP2 and KECK Array experiments have observed the same patch of sky, this SPTpol mass map will be powerful for de-lensing primordial BB power spectrum measurements. Additionally, these deep sptpol mass maps will enable significant cross-correlation measurements with other tracers of large-scale structure.

Polarization measurements will continue to improve rapidly. SPTpol will soon start its fourth year of observing a larger 500 deg^2 patch of sky, ACTpol and POLARBEAR observations are continuing, and *Planck* recently released a similar polarized analysis [98]. With these and the next generation of CMB polarization experiments being planned (e.g., SPT3G [9], AdvancedACTpol [20], Simons Array [5]), CMB lensing will become an exceptionally powerful probe of structure evolution in the universe.

CHAPTER 4

CONCLUSION

Since the first detection of the CMB anisotropy by the *COBE* satellite in 1992 [122], measurements of the CMB temperature anisotropy have shaped our understanding of the universe. These measurements now form a foundation on which the current cosmological paradigm is built. Even with the great success of CMB observations, unanswered fundamental questions are still abundant and much remains to be learned from the CMB.

The primary temperature anisotropy of the CMB has now been exquisitely measured. The large angular scale anisotropies have been measured with cosmic-variance-limited precision for multipoles $\ell \lesssim 1500$ by the *Planck* satellite [99], well into the CMB damping tail. Future high-resolution observations will improve measurements of the CMB damping tail and the foreground-dominated high- ℓ spectrum, further constraining extensions to the Λ CDM model and secondary anisotropies such as the SZ effect.

The next frontier of CMB research is studying the wealth of information encoded in CMB polarization. Two particularly interesting phenomena which produce signatures in CMB polarization are cosmic inflation and the physics of neutrinos. Inflation produces gravitational waves which may be visible at large angular scales in the *B*-mode power spectrum. The search for tensor modes from inflation is well underway [10, 67], however, further improvements will require deeper data, cleaning polarized foregrounds, and removing contamination from lensing [11]. The number of neutrino species affects the energy density - and thus the expansion rate - of the universe particularly at early times, while the sum of the masses of the neutrino species affects both the energy density and the growth of structure in the universe (e.g., see [57]).

These topics can be studied by measuring the CMB polarization power spectra. Foregrounds and atmosphere are largely unpolarized, and thus contribute much less power in polarization than temperature. Consequently, the *EE* and *TE* spectra can probe the primary CMB anisotropies to smaller angular scales, thus improving constraints on the Λ CDM

model and its extensions [46]. The BB spectrum probes parity-violating processes, in particular inflationary gravitational waves at large angular scales $\ell \lesssim 150$ and gravitational lensing at smaller angular scales. These measurements are expected to improve rapidly with measurements from experiments including but not limited to SPTpol, ACT, POLARBEAR, the KECK array, and the final data release from *Planck*.

Beyond the power spectrum, measurements of statistical anisotropy due to gravitational lensing (e.g., chapter 3) will continue to be a powerful approach in the future. Gravitational lensing measurements probe the growth and structure of matter over a broad redshift range. The lensing potential power spectrum has already been used to constrain the parameter combination $\sigma_8\Omega_m^{0.25}$ to $\sim 3\%$ [98], while future experiments are expected to provide percent-level constraints on Ω_m [9]. The next generation of CMB experiments will probe Σm_ν at a level comparable to the largest neutrino mass splitting of 0.06 eV. The correlation between luminous matter and the underlying dark matter structure will be studied by cross-correlating CMB lensing derived mass maps with other tracers of large-scale structure (e.g., galaxy density or weak lensing shear maps), thus constraining the bias of these tracers to better than 1%. Finally, the CMB lensing potential can be combined with high-resolution E -mode maps to clean the lensed component of the B -mode spectrum, aiding the search for inflationary gravitational waves.

CMB polarization information is critical to improving measurements of the lensing potential. The ϕ^{EB} estimator is particularly powerful, since the unlensed B -field does not contribute reconstruction noise (i.e., there is no Gaussian $N0$ bias from the unlensed B -modes) [63]. This estimator with the current data is still noisy: $\sigma(A_{EB}) = 0.38$ for SPTpol (see 3.4) and $\sigma(A_{EB}) \sim 1.8$ for *Planck*() (see table 2 in [98]). This will be a powerful measurement in the near future.

To summarize the work of this thesis, we have presented two measurements and cosmological interpretations of the cosmic microwave background. We first measured the CMB temperature power spectrum using data from the SPT. We then used temperature and po-

larization data from SPTpol to map the CMB gravitational lensing potential and measure its power spectrum. These techniques will be used to further improve measurements of the CMB from SPTpol and subsequent experiments.

The era of CMB polarization has arrived.

REFERENCES

- [1] G. E. Addison, J. Dunkley, A. Hajian, M. Viero, J. R. Bond, S. Das, M. J. Devlin, M. Halpern, A. D. Hincks, R. Hlozek, T. A. Marriage, K. Moodley, L. A. Page, E. D. Reese, D. Scott, D. N. Spergel, S. T. Staggs, and E. Wollack. Power-law Template for Infrared Point-source Clustering. *ApJ*, 752:120, June 2012.
- [2] A. Albrecht. Cosmic Curvature from de Sitter Equilibrium Cosmology. *Physical Review Letters*, 107(15):151102, October 2011.
- [3] A. Albrecht and P. J. Steinhardt. Cosmology for grand unified theories with radiatively induced symmetry breaking. *Phys. Rev. Lett.*, 48:1220–1223, 1982.
- [4] L. Anderson, E. Aubourg, S. Bailey, D. Bizyaev, M. Blanton, A. S. Bolton, J. Brinkmann, J. R. Brownstein, A. Burden, A. J. Cuesta, L. N. A. da Costa, K. S. Dawson, R. de Putter, D. J. Eisenstein, J. E. Gunn, H. Guo, J.-C. Hamilton, P. Harding, S. Ho, K. Honscheid, E. Kazin, D. Kirkby, J.-P. Kneib, A. Labatie, C. Loomis, R. H. Lupton, E. Malanushenko, V. Malanushenko, R. Mandelbaum, M. Manera, C. Maraston, C. K. McBride, K. T. Mehta, O. Mena, F. Montesano, D. Muna, R. C. Nichol, S. E. Nuza, M. D. Olmstead, D. Oravetz, N. Padmanabhan, N. Palanque-Delabrouille, K. Pan, J. Parejko, I. Paris, W. J. Percival, P. Petitjean, F. Prada, B. Reid, N. A. Roe, A. J. Ross, N. P. Ross, L. Samushia, A. G. Sanchez, D. J. S. D. P. Schneider, C. G. Scoccola, H.-J. Seo, E. S. Sheldon, A. Simmons, R. A. Skibba, M. A. Strauss, M. E. C. Swanson, D. Thomas, J. L. Tinker, R. Tojeiro, M. Vargas Magana, L. Verde, C. Wagner, D. A. Wake, B. A. Weaver, D. H. Weinberg, M. White, X. Xu, C. Yeche, I. Zehavi, and G.-B. Zhao. The clustering of galaxies in the SDSS-III Baryon Oscillation Spectroscopic Survey: Baryon Acoustic Oscillations in the Data Release 9 Spectroscopic Galaxy Sample. *ArXiv e-prints*, March 2012.
- [5] K. Arnold, N. Stebor, P. A. R. Ade, Y. Akiba, A. E. Anthony, M. Atlas, D. Barron, A. Bender, D. Boettger, J. Borrill, S. Chapman, Y. Chinone, A. Cukierman, M. Dobbs, T. Elleflot, J. Errard, G. Fabbian, C. Feng, A. Gilbert, N. Goeckner-Wald, N. W. Halverson, M. Hasegawa, K. Hattori, M. Hazumi, W. L. Holzapfel, Y. Hori, Y. Inoue, G. C. Jaehnig, A. H. Jaffe, N. Katayama, B. Keating, Z. Kermish, R. Keskitalo, T. Kisner, M. Le Jeune, A. T. Lee, E. M. Leitch, E. Linder, F. Matsuda, T. Matsumura, X. Meng, N. J. Miller, H. Morii, M. J. Myers, M. Navaroli, H. Nishino, T. Okamura, H. Paar, J. Peloton, D. Poletti, C. Raum, G. Rebeiz, C. L. Reichardt, P. L. Richards, C. Ross, K. M. Rotermund, D. E. Schenck, B. D. Sherwin, I. Shirley, M. Sholl, P. Siritanasak, G. Smecher, B. Steinbach, R. Stompor, A. Suzuki, J. Suzuki, S. Takada, S. Takakura, T. Tomaru, B. Wilson, A. Yadav, and O. Zahn. The Simons Array: expanding POLARBEAR to three multi-chroic telescopes. In *Society of Photo-Optical Instrumentation Engineers (SPIE) Conference Series*, volume 9153 of *Society of Photo-Optical Instrumentation Engineers (SPIE) Conference Series*, page 1, August 2014.
- [6] J. E. Austermann, K. A. Aird, J. A. Beall, D. Becker, A. Bender, B. A. Benson, L. E. Bleem, J. Britton, J. E. Carlstrom, C. L. Chang, H. C. Chiang, H.-M. Cho, T. M.

- Crawford, A. T. Crites, A. Datesman, T. de Haan, M. A. Dobbs, E. M. George, N. W. Halverson, N. Harrington, J. W. Henning, G. C. Hilton, G. P. Holder, W. L. Holzapfel, S. Hoover, N. Huang, J. Hubmayr, K. D. Irwin, R. Keisler, J. Kennedy, L. Knox, A. T. Lee, E. Leitch, D. Li, M. Lueker, D. P. Marrone, J. J. McMahon, J. Mehl, S. S. Meyer, T. E. Montroy, T. Natoli, J. P. Nibarger, M. D. Niemack, V. Novosad, S. Padin, C. Pryke, C. L. Reichardt, J. E. Ruhl, B. R. Saliwanchik, J. T. Sayre, K. K. Schaffer, E. Shirokoff, A. A. Stark, K. Story, K. Vanderlinde, J. D. Vieira, G. Wang, R. Williamson, V. Yefremenko, K. W. Yoon, and O. Zahn. SPTpol: an instrument for CMB polarization measurements with the South Pole Telescope. In *Society of Photo-Optical Instrumentation Engineers (SPIE) Conference Series*, volume 8452, September 2012.
- [7] J.̃M. Bardeen, P.̃J. Steinhardt, and M.̃S. Turner. Spontaneous creation of almost scale-free density perturbations in an inflationary universe. *Phys. Rev. D*, 28:679, August 1983.
- [8] D. Baumann, M. G. Jackson, P. Adshead, A. Amblard, A. Ashoorioon, N. Bartolo, R. Bean, M. Beltrán, F. de Bernardis, S. Bird, X. Chen, D. J. H. Chung, L. Colombo, A. Cooray, P. Creminelli, S. Dodelson, J. Dunkley, C. Dvorkin, R. Easther, F. Finelli, R. Flauger, M. P. Hertzberg, K. Jones-Smith, S. Kachru, K. Kadota, J. Khoury, W. H. Kinney, E. Komatsu, L. M. Krauss, J. Lesgourgues, A. Liddle, M. Liguori, E. Lim, A. Linde, S. Matarrese, H. Mathur, L. McAllister, A. Melchiorri, A. Nicolis, L. Pagano, H. V. Peiris, M. Peloso, L. Pogosian, E. Pierpaoli, A. Riotto, U. Seljak, L. Senatore, S. Shandera, E. Silverstein, T. Smith, P. Vaudrevange, L. Verde, B. Wandelt, D. Wands, S. Watson, M. Wyman, A. Yadav, W. Valkenburg, and M. Zaldarriaga. Probing Inflation with CMB Polarization. In S. Dodelson, D. Baumann, A. Cooray, J. Dunkley, A. Fraisse, M. G. Jackson, A. Kogut, L. Krauss, M. Zaldarriaga, and K. Smith, editors, *American Institute of Physics Conference Series*, volume 1141 of *American Institute of Physics Conference Series*, pages 10–120, June 2009.
- [9] B. A. Benson, P. A. R. Ade, Z. Ahmed, S. W. Allen, K. Arnold, J. E. Austermann, A. N. Bender, L. E. Bleem, J. E. Carlstrom, C. L. Chang, H. M. Cho, J. F. Cliche, T. M. Crawford, A. Cukierman, T. de Haan, M. A. Dobbs, D. Dutcher, W. Everett, A. Gilbert, N. W. Halverson, D. Hanson, N. L. Harrington, K. Hattori, J. W. Henning, G. C. Hilton, G. P. Holder, W. L. Holzapfel, K. D. Irwin, R. Keisler, L. Knox, D. Kubik, C. L. Kuo, A. T. Lee, E. M. Leitch, D. Li, M. McDonald, S. S. Meyer, J. Montgomery, M. Myers, T. Natoli, H. Nguyen, V. Novosad, S. Padin, Z. Pan, J. Pearson, C. Reichardt, J. E. Ruhl, B. R. Saliwanchik, G. Simard, G. Smecher, J. T. Sayre, E. Shirokoff, A. A. Stark, K. Story, A. Suzuki, K. L. Thompson, C. Tucker, K. Vanderlinde, J. D. Vieira, A. Vikhlinin, G. Wang, V. Yefremenko, and K. W. Yoon. SPT-3G: a next-generation cosmic microwave background polarization experiment on the South Pole telescope. In *Society of Photo-Optical Instrumentation Engineers (SPIE) Conference Series*, volume 9153 of *Society of Photo-Optical Instrumentation Engineers (SPIE) Conference Series*, page 1, July 2014.

- [10] BICEP2 Collaboration. Detection of B-Mode Polarization at Degree Angular Scales by BICEP2. *Physical Review Letters*, 112(24):241101, June 2014.
- [11] BICEP2/Keck and Planck Collaborations, :, P. A. R. Ade, N. Aghanim, Z. Ahmed, R. W. Aikin, K. D. Alexander, M. Arnaud, J. Aumont, and et al. A Joint Analysis of BICEP2/Keck Array and Planck Data. *ArXiv e-prints*, February 2015.
- [12] C. Blake, E. A. Kazin, F. Beutler, T. M. Davis, D. Parkinson, S. Brough, M. Colless, C. Contreras, W. Couch, S. Croom, D. Croton, M. J. Drinkwater, K. Forster, D. Gilbank, M. Gladders, K. Glazebrook, B. Jelliffe, R. J. Jurek, I.-H. Li, B. Madore, D. C. Martin, K. Pimbblet, G. B. Poole, M. Pracy, R. Sharp, E. Wisnioski, D. Woods, T. K. Wyder, and H. K. C. Yee. The WiggleZ Dark Energy Survey: mapping the distance-redshift relation with baryon acoustic oscillations. *MNRAS*, 418:1707–1724, December 2011.
- [13] A. Blanchard and J. Schneider. Gravitational lensing effect on the fluctuations of the cosmic background radiation. *A&A*, 184:1–6, October 1987.
- [14] L. E. Bleem, B. Stalder, T. de Haan, K. A. Aird, S. W. Allen, D. E. Applegate, M. L. N. Ashby, M. Bautz, M. Bayliss, B. A. Benson, S. Bocquet, M. Brodwin, J. E. Carlstrom, C. L. Chang, I. Chiu, H. M. Cho, A. Clocchiatti, T. M. Crawford, A. T. Crites, S. Desai, J. P. Dietrich, M. A. Dobbs, R. J. Foley, W. R. Forman, E. M. George, M. D. Gladders, A. H. Gonzalez, N. W. Halverson, C. Hennig, H. Hoekstra, G. P. Holder, W. L. Holzapfel, J. D. Hrubes, C. Jones, R. Keisler, L. Knox, A. T. Lee, E. M. Leitch, J. Liu, M. Lueker, D. Luong-Van, A. Mantz, D. P. Marrone, M. McDonald, J. J. McMahon, S. S. Meyer, L. Mocanu, J. J. Mohr, S. S. Murray, S. Padin, C. Pryke, C. L. Reichardt, A. Rest, J. Ruel, J. E. Ruhl, B. R. Saliwanchik, A. Saro, J. T. Sayre, K. K. Schaffer, T. Schrabback, E. Shirokoff, J. Song, H. G. Spieler, S. A. Stanford, Z. Staniszewski, A. A. Stark, K. T. Story, C. W. Stubbs, K. Vanderlinde, J. D. Vieira, A. Vikhlinin, R. Williamson, O. Zahn, and A. Zenteno. Galaxy Clusters Discovered via the Sunyaev-Zel’dovich Effect in the 2500-Square-Degree SPT-SZ Survey. *ApJS*, 216:27, February 2015.
- [15] L. E. Bleem, A. van Engelen, G. P. Holder, K. A. Aird, R. Armstrong, M. L. N. Ashby, M. R. Becker, B. A. Benson, T. Biesiadzinski, M. Brodwin, M. T. Busha, J. E. Carlstrom, C. L. Chang, H. M. Cho, T. M. Crawford, A. T. Crites, T. de Haan, S. Desai, M. A. Dobbs, O. Doré, J. Dudley, J. E. Geach, E. M. George, M. D. Gladders, A. H. Gonzalez, N. W. Halverson, N. Harrington, F. W. High, B. P. Holden, W. L. Holzapfel, S. Hoover, J. D. Hrubes, M. Joy, R. Keisler, L. Knox, A. T. Lee, E. M. Leitch, M. Lueker, D. Luong-Van, D. P. Marrone, J. Martinez-Manso, J. J. McMahon, J. Mehl, S. S. Meyer, J. J. Mohr, T. E. Montroy, T. Natoli, S. Padin, T. Plagge, C. Pryke, C. L. Reichardt, A. Rest, J. E. Ruhl, B. R. Saliwanchik, J. T. Sayre, K. K. Schaffer, L. Shaw, E. Shirokoff, H. G. Spieler, B. Stalder, S. A. Stanford, Z. Staniszewski, A. A. Stark, D. Stern, K. Story, A. Vallinotto, K. Vanderlinde, J. D. Vieira, R. H. Wechsler, R. Williamson, and O. Zahn. A Measurement of the Correlation of Galaxy Surveys with CMB Lensing Convergence Maps from the South Pole Telescope. *ApJ*, 753:L9, June 2012.

- [16] J. R. Bond, G. Efstathiou, and M. Tegmark. Forecasting cosmic parameter errors from microwave background anisotropy experiments. *MNRAS*, 291:L33–L41, November 1997.
- [17] M. L. Brown, P. Ade, J. Bock, M. Bowden, G. Cahill, P. G. Castro, S. Church, T. Culverhouse, R. B. Friedman, K. Ganga, W. K. Gear, S. Gupta, J. Hinderks, J. Kovac, A. E. Lange, E. Leitch, S. J. Melhuish, Y. Memari, J. A. Murphy, A. Orlando, C. O’Sullivan, L. Piccirillo, C. Pryke, N. Rajguru, B. Rusholme, R. Schwarz, A. N. Taylor, K. L. Thompson, A. H. Turner, E. Y. S. Wu, M. Zemcov, and The QUaD collaboration. Improved Measurements of the Temperature and Polarization of the Cosmic Microwave Background from QUaD. *ApJ*, 705:978–999, November 2009.
- [18] M. Bucher, A. S. Goldhaber, and N. Turok. Open universe from inflation. *Phys. Rev. D*, 52:3314–3337, September 1995.
- [19] E. Calabrese, A. Cooray, M. Martinelli, A. Melchiorri, L. Pagano, A. Slosar, and G. F. Smoot. CMB lensing constraints on dark energy and modified gravity scenarios. *Phys. Rev. D*, 80(10):103516, November 2009.
- [20] E. Calabrese, R. Hlozek, N. Battaglia, J. R. Bond, F. de Bernardis, M. J. Devlin, A. Hajian, S. Henderson, J. C. Hil, A. Kosowsky, T. Louis, J. McMahon, K. Moodley, L. Newburgh, M. D. Niemack, L. A. Page, B. Partridge, N. Sehgal, J. L. Sievers, D. N. Spergel, S. T. Staggs, E. R. Switzer, H. Trac, and E. J. Wollack. Precision epoch of reionization studies with next-generation CMB experiments. *J. of Cosm. & Astropart. Phys.*, 8:10, August 2014.
- [21] E. Calabrese, A. Slosar, A. Melchiorri, G. F. Smoot, and O. Zahn. Cosmic microwave weak lensing data as a test for the dark universe. *Phys. Rev. D*, 77(12):123531–+, June 2008.
- [22] J. E. Carlstrom, P. A. R. Ade, K. A. Aird, B. A. Benson, L. E. Bleem, S. Busetti, C. L. Chang, E. Chauvin, H.-M. Cho, T. M. Crawford, A. T. Crites, M. A. Dobbs, N. W. Halverson, S. Heimsath, W. L. Holzapfel, J. D. Hrubes, M. Joy, R. Keisler, T. M. Lanting, A. T. Lee, E. M. Leitch, J. Leong, W. Lu, M. Lueker, D. Luongvan, J. J. McMahon, J. Mehl, S. S. Meyer, J. J. Mohr, T. E. Montroy, S. Padin, T. Plagge, C. Pryke, J. E. Ruhl, K. K. Schaffer, D. Schwan, E. Shirokoff, H. G. Spieler, Z. Staniszewski, A. A. Stark, C. Tucker, K. Vanderlinde, J. D. Vieira, and R. Williamson. The 10 Meter South Pole Telescope. *PASP*, 123:568–581, May 2011.
- [23] H. C. Chiang, P. A. R. Ade, D. Barkats, J. O. Battle, E. M. Bierman, J. J. Bock, C. D. Dowell, L. Duband, E. F. Hivon, W. L. Holzapfel, V. V. Hristov, W. C. Jones, B. G. Keating, J. M. Kovac, C. L. Kuo, A. E. Lange, E. M. Leitch, P. V. Mason, T. Matsumura, H. T. Nguyen, N. Ponthieu, C. Pryke, S. Richter, G. Rocha, C. Sheehy, Y. D. Takahashi, J. E. Tolan, and K. W. Yoon. Measurement of Cosmic Microwave Background Polarization Power Spectra from Two Years of BICEP Data. *ApJ*, 711:1123–1140, March 2010.

- [24] N. Christensen, R. Meyer, L. Knox, and B. Luey. Bayesian methods for cosmological parameter estimation from cosmic microwave background measurements. *Classical and Quantum Gravity*, 18:2677–2688, July 2001.
- [25] S. Cole and G. Efstathiou. Gravitational lensing of fluctuations in the microwave background radiation. *MNRAS*, 239:195–200, July 1989.
- [26] S. Coleman and E. Weinberg. Radiative Corrections as the Origin of Spontaneous Symmetry Breaking. *Phys. Rev. D*, 7:1888–1910, March 1973.
- [27] A. Cooray, M. Kamionkowski, and R. R. Caldwell. Cosmic shear of the microwave background: The curl diagnostic. *Phys. Rev. D*, 71(12):123527–+, June 2005.
- [28] E. J. Copeland, E. W. Kolb, A. R. Liddle, and J. E. Lidsey. Observing the inflation potential. *Physical Review Letters*, 71:219–222, July 1993.
- [29] A. T. Crites, J. W. Henning, P. A. R. Ade, K. A. Aird, J. E. Austermann, J. A. Beall, A. N. Bender, B. A. Benson, L. E. Bleem, J. E. Carstrom, C. L. Chang, H. C. Chiang, H. Cho, R. Citron, T. M. Crawford, T. De Haan, M. A. Dobbs, W. Everett, J. Gallicchio, J. Gao, E. M. George, A. Gilbert, N. W. Halverson, D. Hanson, N. Harrington, G. C. Hilton, G. P. Holder, W. L. Holzapfel, S. Hoover, Z. Hou, J. D. Hrubes, N. Huang, J. Hubmayr, K. D. Irwin, R. Keisler, L. Knox, A. T. Lee, E. M. Leitch, D. Li, C. Liang, D. Luong-Van, J. J. McMahon, J. Mehl, S. S. Meyer, L. Mocuano, T. E. Montroy, T. Natoli, J. P. Nibarger, V. Novosad, S. Padin, C. Pryke, C. L. Reichardt, J. E. Ruhl, B. R. Saliwanchik, J. T. Sayre, K. K. Schaffer, G. Smecher, A. A. Stark, K. T. Story, C. Tucker, K. Vanderlinde, J. D. Vieira, G. Wang, N. Whitehorn, V. Yefremenko, and O. Zahn. Measurements of E-Mode Polarization and Temperature-E-Mode Correlation in the Cosmic Microwave Background from 100 Square Degrees of SPTpol Data. *ArXiv e-prints*, November 2014.
- [30] S. Das, T. Louis, M. R. Nolte, G. E. Addison, E. S. Battistelli, J. R. Bond, E. Calabrese, D. Crichton, M. J. Devlin, S. Dicker, J. Dunkley, R. Dünner, J. W. Fowler, M. Gralla, A. Hajian, M. Halpern, M. Hasselfield, M. Hilton, A. D. Hincks, R. Hlozek, K. M. Huffenberger, J. P. Hughes, K. D. Irwin, A. Kosowsky, R. H. Lupton, T. A. Marriage, D. Marsden, F. Menanteau, K. Moodley, M. D. Niemack, L. A. Page, B. Partridge, E. D. Reese, B. L. Schmitt, N. Sehgal, B. D. Sherwin, J. L. Sievers, D. N. Spergel, S. T. Staggs, D. S. Swetz, E. R. Switzer, R. Thornton, H. Trac, and E. Wollack. The Atacama Cosmology Telescope: temperature and gravitational lensing power spectrum measurements from three seasons of data. *J. of Cosm. & Astropart. Phys.*, 4:14, April 2014.
- [31] S. Das, T. A. Marriage, P. A. R. Ade, P. Aguirre, M. Amiri, J. W. Appel, L. F. Barrientos, E. S. Battistelli, J. R. Bond, B. Brown, B. Burger, J. Chervenak, M. J. Devlin, S. R. Dicker, W. Bertrand Doriese, J. Dunkley, R. Dünner, T. Essinger-Hileman, R. P. Fisher, J. W. Fowler, A. Hajian, M. Halpern, M. Hasselfield, C. Hernández-Monteagudo, G. C. Hilton, M. Hilton, A. D. Hincks, R. Hlozek, K. M. Huffenberger, D. H. Hughes, J. P. Hughes, L. Infante, K. D. Irwin, J. Baptiste Juin, M. Kaul,

- J. Klein, A. Kosowsky, J. M. Lau, M. Limon, Y.-T. Lin, R. H. Lupton, D. Marsden, K. Martocci, P. Mauskopf, F. Menanteau, K. Moodley, H. Moseley, C. B. Netterfield, M. D. Niemack, M. R. Nolta, L. A. Page, L. Parker, B. Partridge, B. Reid, N. Sehgal, B. D. Sherwin, J. Sievers, D. N. Spergel, S. T. Staggs, D. S. Swetz, E. R. Switzer, R. Thornton, H. Trac, C. Tucker, R. Warne, E. Wollack, and Y. Zhao. The Atacama Cosmology Telescope: A Measurement of the Cosmic Microwave Background Power Spectrum at 148 and 218 GHz from the 2008 Southern Survey. *ApJ*, 729:62–+, March 2011.
- [32] S. Das, B. D. Sherwin, P. Aguirre, J. W. Appel, J. R. Bond, C. S. Carvalho, M. J. Devlin, J. Dunkley, R. Dünner, T. Essinger-Hileman, J. W. Fowler, A. Hajian, M. Halpern, M. Hasselfield, A. D. Hincks, R. Hlozek, K. M. Huffenberger, J. P. Hughes, K. D. Irwin, J. Klein, A. Kosowsky, R. H. Lupton, T. A. Marriage, D. Marsden, F. Menanteau, K. Moodley, M. D. Niemack, M. R. Nolta, L. A. Page, L. Parker, E. D. Reese, B. L. Schmitt, N. Sehgal, J. Sievers, D. N. Spergel, S. T. Staggs, D. S. Swetz, E. R. Switzer, R. Thornton, K. Visnjic, and E. Wollack. Detection of the Power Spectrum of Cosmic Microwave Background Lensing by the Atacama Cosmology Telescope. *Physical Review Letters*, 107(2):021301–+, July 2011.
- [33] T. de Haan, G. Smecher, and M. Dobbs. Improved performance of TES bolometers using digital feedback. In *Society of Photo-Optical Instrumentation Engineers (SPIE) Conference Series*, volume 8452 of *Society of Photo-Optical Instrumentation Engineers (SPIE) Conference Series*, September 2012.
- [34] R. de Putter, O. Zahn, and E. V. Linder. CMB lensing constraints on neutrinos and dark energy. *Phys. Rev. D*, 79(6):065033–+, March 2009.
- [35] G. De Zotti, M. Massardi, M. Negrello, and J. Wall. Radio and millimeter continuum surveys and their astrophysical implications. *A&A Rev.*, 18:1–65, February 2010.
- [36] M. Dobbs, E. Bissonnette, and H. Spieler. Digital Frequency Domain Multiplexer for Millimeter-Wavelength Telescopes. *IEEE Transactions on Nuclear Science*, 55:21–26, 2008.
- [37] S. Dodelson, W. H. Kinney, and E. W. Kolb. Cosmic microwave background measurements can discriminate among inflation models. *Phys. Rev. D*, 56:3207–3215, September 1997.
- [38] S. Dodelson and L. Knox. Dark Energy and the Cosmic Microwave Background Radiation. *Physical Review Letters*, 84:3523–3526, April 2000.
- [39] J. Dunkley, R. Hlozek, J. Sievers, V. Acquaviva, P. A. R. Ade, P. Aguirre, M. Amiri, J. W. Appel, L. F. Barrientos, E. S. Battistelli, J. R. Bond, B. Brown, B. Burger, J. Chervenak, S. Das, M. J. Devlin, S. R. Dicker, W. Bertrand Doriese, R. Dünner, T. Essinger-Hileman, R. P. Fisher, J. W. Fowler, A. Hajian, M. Halpern, M. Hasselfield, C. Hernández-Monteagudo, G. C. Hilton, M. Hilton, A. D. Hincks, K. M. Huffenberger, D. H. Hughes, J. P. Hughes, L. Infante, K. D. Irwin, J. B. Juin, M. Kaul,

- J. Klein, A. Kosowsky, J. M. Lau, M. Limon, Y.-T. Lin, R. H. Lupton, T. A. Marriage, D. Marsden, P. Mauskopf, F. Menanteau, K. Moodley, H. Moseley, C. B. Netterfield, M. D. Niemack, M. R. Nolta, L. A. Page, L. Parker, B. Partridge, B. Reid, N. Sehgal, B. Sherwin, D. N. Spergel, S. T. Staggs, D. S. Swetz, E. R. Switzer, R. Thornton, H. Trac, C. Tucker, R. Warne, E. Wollack, and Y. Zhao. The Atacama Cosmology Telescope: Cosmological Parameters from the 2008 Power Spectrum. *ApJ*, 739:52–+, September 2011.
- [40] R. Dünner, M. Hasselfield, T. A. Marriage, J. Sievers, V. Acquaviva, G. E. Addison, P. A. R. Ade, P. Aguirre, M. Amiri, J. W. Appel, L. F. Barrientos, E. S. Battistelli, J. R. Bond, B. Brown, B. Burger, E. Calabrese, J. Chervenak, S. Das, M. J. Devlin, S. R. Dicker, W. Bertrand Doriese, J. Dunkley, T. Essinger-Hileman, R. P. Fisher, M. B. Gralla, J. W. Fowler, A. Hajian, M. Halpern, C. Hernández-Monteagudo, G. C. Hilton, M. Hilton, A. D. Hincks, R. Hlozek, K. M. Huffenberger, D. H. Hughes, J. P. Hughes, L. Infante, K. D. Irwin, J. Baptiste Juin, M. Kaul, J. Klein, A. Kosowsky, J. M. Lau, M. Limon, Y.-T. Lin, T. Louis, R. H. Lupton, D. Marsden, K. Martocci, P. Mauskopf, F. Menanteau, K. Moodley, H. Moseley, C. B. Netterfield, M. D. Niemack, M. R. Nolta, L. A. Page, L. Parker, B. Partridge, H. Quintana, B. Reid, N. Sehgal, B. D. Sherwin, D. N. Spergel, S. T. Staggs, D. S. Swetz, E. R. Switzer, R. Thornton, H. Trac, C. Tucker, R. Warne, G. Wilson, E. Wollack, and Y. Zhao. The Atacama Cosmology Telescope: Data Characterization and Mapmaking. *ApJ*, 762:10, January 2013.
- [41] W. A. Fendt and B. D. Wandelt. Computing High Accuracy Power Spectra with Pico. *ArXiv:0712.0194*, December 2007.
- [42] W. A. Fendt and B. D. Wandelt. Pico: Parameters for the Impatient Cosmologist. *ApJ*, 654:2–11, January 2007.
- [43] D. P. Finkbeiner, M. Davis, and D. J. Schlegel. Extrapolation of galactic dust emission at 100 microns to cosmic microwave background radiation frequencies using firas. *ApJ*, 524:867–886, October 1999.
- [44] J. W. Fowler, V. Acquaviva, P. A. R. Ade, P. Aguirre, M. Amiri, J. W. Appel, L. F. Barrientos, E. S. Battistelli, J. R. Bond, B. Brown, B. Burger, J. Chervenak, S. Das, M. J. Devlin, S. R. Dicker, W. B. Doriese, J. Dunkley, R. Dünner, T. Essinger-Hileman, R. P. Fisher, A. Hajian, M. Halpern, M. Hasselfield, C. Hernández-Monteagudo, G. C. Hilton, M. Hilton, A. D. Hincks, R. Hlozek, K. M. Huffenberger, D. H. Hughes, J. P. Hughes, L. Infante, K. D. Irwin, R. Jimenez, J. B. Juin, M. Kaul, J. Klein, A. Kosowsky, J. M. Lau, M. Limon, Y.-T. Lin, R. H. Lupton, T. A. Marriage, D. Marsden, K. Martocci, P. Mauskopf, F. Menanteau, K. Moodley, H. Moseley, C. B. Netterfield, M. D. Niemack, M. R. Nolta, L. A. Page, L. Parker, B. Partridge, H. Quintana, B. Reid, N. Sehgal, J. Sievers, D. N. Spergel, S. T. Staggs, D. S. Swetz, E. R. Switzer, R. Thornton, H. Trac, C. Tucker, L. Verde, R. Warne, G. Wilson, E. Wollack, and Y. Zhao. The Atacama Cosmology Telescope: A Measurement of the 600 μ ell μ 8000 Cosmic Microwave Background Power Spectrum at 148 GHz. *ApJ*, 722:1148–1161, October 2010.

- [45] R. B. Friedman, P. Ade, J. Bock, M. Bowden, M. L. Brown, G. Cahill, P. G. Castro, S. Church, T. Culverhouse, K. Ganga, W. K. Gear, S. Gupta, J. Hinderks, J. Kovac, A. E. Lange, E. Leitch, S. J. Melhuish, Y. Memari, J. A. Murphy, A. Orlando, C. O’Sullivan, L. Piccirillo, C. Pryke, N. Rajguru, B. Rusholme, R. Schwarz, A. N. Taylor, K. L. Thompson, A. H. Turner, E. Y. S. Wu, M. Zemcov, and QUaD collaboration. Small Angular Scale Measurements of the Cosmic Microwave Background Temperature Power Spectrum From QUaD. *ApJ Lett.*, 700:L187–L191, August 2009.
- [46] S. Galli, K. Benabed, F. Bouchet, J.-F. Cardoso, F. Elsner, E. Hivon, A. Mangilli, S. Prunet, and B. Wandelt. CMB polarization can constrain cosmology better than CMB temperature. *Phys. Rev. D*, 90(6):063504, September 2014.
- [47] E. M. George, P. Ade, K. A. Aird, J. E. Austermann, J. A. Beall, D. Becker, A. Bender, B. A. Benson, L. E. Bleem, J. Britton, J. E. Carlstrom, C. L. Chang, H. C. Chiang, H.-M. Cho, T. M. Crawford, A. T. Crites, A. Datesman, T. de Haan, M. A. Dobbs, W. Everett, A. Ewall-Wice, N. W. Halverson, N. Harrington, J. W. Henning, G. C. Hilton, W. L. Holzapfel, S. Hoover, N. Huang, J. Hubmayr, K. D. Irwin, M. Karfunkle, R. Keisler, J. Kennedy, A. T. Lee, E. Leitch, D. Li, M. Lueker, D. P. Marrone, J. J. McMahon, J. Mehl, S. S. Meyer, J. Montgomery, T. E. Montroy, J. Nagy, T. Natoli, J. P. Nibarger, M. D. Niemack, V. Novosad, S. Padin, C. Pryke, C. L. Reichardt, J. E. Ruhl, B. R. Saliwanchik, J. T. Sayre, K. K. Schaffer, E. Shirokoff, K. Story, C. Tucker, K. Vanderlinde, J. D. Vieira, G. Wang, R. Williamson, V. Yefremenko, K. W. Yoon, and E. Young. Performance and on-sky optical characterization of the SPTpol instrument. In *Society of Photo-Optical Instrumentation Engineers (SPIE) Conference Series*, volume 8452, September 2012.
- [48] E. M. George, C. L. Reichardt, K. A. Aird, B. A. Benson, L. E. Bleem, J. E. Carlstrom, C. L. Chang, H. Cho, T. M. Crawford, A. T. Crites, T. de Haan, M. A. Dobbs, J. Dudley, N. W. Halverson, N. L. Harrington, G. P. Holder, W. L. Holzapfel, Z. Hou, J. D. Hrubes, R. Keisler, L. Knox, A. T. Lee, E. M. Leitch, M. Lueker, D. Luong-Van, J. J. McMahon, J. Mehl, S. S. Meyer, M. Millea, L. M. Mocanu, J. J. Mohr, T. E. Montroy, S. Padin, T. Plagge, C. Pryke, J. E. Ruhl, K. K. Schaffer, L. Shaw, E. Shirokoff, H. G. Spieler, Z. Staniszewski, A. A. Stark, K. T. Story, A. van Engelen, K. Vanderlinde, J. D. Vieira, R. Williamson, and O. Zahn. A measurement of secondary cosmic microwave background anisotropies from the 2500-square-degree SPT-SZ survey. *ArXiv e-prints*, August 2014.
- [49] K. M. Górski, E. Hivon, A. J. Banday, B. D. Wandelt, F. K. Hansen, M. Reinecke, and M. Bartelmann. HEALPix: A Framework for High-Resolution Discretization and Fast Analysis of Data Distributed on the Sphere. *ApJ*, 622:759–771, April 2005.
- [50] A. H. Guth. Inflationary universe: A possible solution to the horizon and flatness problems. *Phys. Rev. D*, 23:347–356, January 1981.
- [51] A. H. Guth and S. Pi. Fluctuations in the new inflationary universe. *Physical Review Letters*, 49:1110–1113, October 1982.

- [52] D. Hanson et al. Detection of B-mode Polarization in the Cosmic Microwave Background with Data from the South Pole Telescope. *Phys.Rev.Lett.*, 111(14):141301, 2013.
- [53] S. W. Hawking. *Phys. Lett. B*, 115:295, 1982.
- [54] G. Hinshaw, D. Larson, E. Komatsu, D. N. Spergel, C. L. Bennett, J. Dunkley, M. R. Nolta, M. Halpern, R. S. Hill, N. Odegard, L. Page, K. M. Smith, J. L. Weiland, B. Gold, N. Jarosik, A. Kogut, M. Limon, S. S. Meyer, G. S. Tucker, E. Wollack, and E. L. Wright. Nine-year Wilkinson Microwave Anisotropy Probe (WMAP) Observations: Cosmological Parameter Results. *ApJS*, 208:19, October 2013.
- [55] C. M. Hirata, S. Ho, N. Padmanabhan, U. Seljak, and N. A. Bahcall. Correlation of CMB with large-scale structure. II. Weak lensing. *Phys. Rev. D*, 78(4):043520–+, August 2008.
- [56] E. Hivon, K. M. Górski, C. B. Netterfield, B. P. Crill, S. Prunet, and F. Hansen. MASTER of the Cosmic Microwave Background Anisotropy Power Spectrum: A Fast Method for Statistical Analysis of Large and Complex Cosmic Microwave Background Data Sets. *ApJ*, 567:2–17, March 2002.
- [57] Z. Hou, C. L. Reichardt, K. T. Story, B. Follin, R. Keisler, K. A. Aird, B. A. Benson, L. E. Bleem, J. E. Carlstrom, C. L. Chang, H.-M. Cho, T. M. Crawford, A. T. Crites, T. de Haan, R. de Putter, M. A. Dobbs, S. Dodelson, J. Dudley, E. M. George, N. W. Halverson, G. P. Holder, W. L. Holzapfel, S. Hoover, J. D. Hrubes, M. Joy, L. Knox, A. T. Lee, E. M. Leitch, M. Lueker, D. Luong-Van, J. J. McMahon, J. Mehl, S. S. Meyer, M. Millea, J. J. Mohr, T. E. Montroy, S. Padin, T. Plagge, C. Pryke, J. E. Ruhl, J. T. Sayre, K. K. Schaffer, L. Shaw, E. Shirokoff, H. G. Spieler, Z. Staniszewski, A. A. Stark, A. van Engelen, K. Vanderlinde, J. D. Vieira, R. Williamson, and O. Zahn. Constraints on Cosmology from the Cosmic Microwave Background Power Spectrum of the 2500 deg² SPT-SZ Survey. *ApJ*, 782:74, February 2014.
- [58] W. Hu. Mapping the Dark Matter through the Cosmic Microwave Background Damping Tail. *ApJ Lett.*, 557:L79–L83, August 2001.
- [59] W. Hu. CMB temperature and polarization anisotropy fundamentals. *Annals of Physics*, 303:203–225, January 2003.
- [60] W. Hu and S. Dodelson. Cosmic Microwave Background Anisotropies. *ARA&A*, 40:171–216, 2002.
- [61] W. Hu and N. Sugiyama. Anisotropies in the cosmic microwave background: an analytic approach. *ApJ*, 444:489–506, 1995.
- [62] W. Hu and M. White. A CMB polarization primer. *New Astronomy*, 2:323–344, 1997. astro-ph/9706147.
- [63] Wayne Hu and Takemi Okamoto. Mass reconstruction with cmb polarization. *Astrophys.J.*, 574:566–574, 2002.

- [64] S. Kachru, R. Kallosh, A. Linde, J. Maldacena, L. McAllister, and S. P. Trivedi. Towards inflation in string theory. *J. of Cosm. & Astropart. Phys.*, 10:13, October 2003.
- [65] N. Kaiser. Small-angle anisotropy of the microwave background radiation in the adiabatic theory. *MNRAS*, 202:1169–1180, March 1983.
- [66] M. Kamionkowski, A. Kosowsky, and A. Stebbins. Statistics of Cosmic Microwave Background Polarization. *Phys. Rev. D*, 55:7368–7388, June 1997.
- [67] Keck Array and BICEP2 Collaborations, P. A. R. Ade, Z. Ahmed, R. W. Aikin, K. D. Alexander, D. Barkats, S. J. Benton, C. A. Bischoff, J. J. Bock, J. A. Brevik, I. Buder, E. Bullock, V. Buza, J. Connors, B. P. Crill, C. D. Dowell, C. Dvorkin, L. Duband, J. P. Filippini, S. Fliescher, S. R. Golwala, M. Halpern, M. Hasselfield, S. R. Hildebrandt, G. C. Hilton, V. V. Hristov, H. Hui, K. D. Irwin, K. S. Karkare, J. P. Kaufman, B. G. Keating, S. Kefeli, S. A. Kernasovskiy, J. M. Kovac, C. L. Kuo, E. M. Leitch, M. Lueker, P. Mason, K. G. Megerian, C. B. Netterfield, H. T. Nguyen, R. O’Brien, R. W. Ogburn, IV, A. Orlando, C. Pryke, C. D. Reintsema, S. Richter, R. Schwarz, C. D. Sheehy, Z. K. Staniszewski, R. V. Sudiwala, G. P. Teply, K. L. Thompson, J. E. Tolan, A. D. Turner, A. G. Vieregg, A. C. Weber, J. Willmert, C. L. Wong, and K. W. Yoon. BICEP2 / Keck Array V: Measurements of B-mode Polarization at Degree Angular Scales and 150 GHz by the Keck Array. *ArXiv e-prints*, February 2015.
- [68] R. Keisler, S. Hoover, N. Harrington, J. W. Henning, P. A. R. Ade, K. A. Aird, J. E. Austermann, J. A. Beall, A. N. Bender, B. A. Benson, L. E. Bleem, J. E. Carlstrom, C. L. Chang, H. C. Chiang, H. Cho, R. Citron, T. M. Crawford, A. T. Crites, T. de Haan, M. A. Dobbs, W. Everett, J. Gallicchio, J. Gao, E. M. George, A. Gilbert, N. W. Halverson, D. Hanson, G. C. Hilton, G. P. Holder, W. L. Holzapfel, Z. Hou, J. D. Hrubes, N. Huang, J. Hubmayr, K. D. Irwin, L. Knox, A. T. Lee, E. M. Leitch, D. Li, D. Luong-Van, D. P. Marrone, J. J. McMahon, J. Mehl, S. S. Meyer, L. Mocanu, T. Natoli, J. P. Nibarger, V. Novosad, S. Padin, C. Pryke, C. L. Reichardt, J. E. Ruhl, B. R. Saliwanchik, J. T. Sayre, K. K. Schaffer, E. Shirokoff, G. Smecher, A. A. Stark, K. T. Story, C. Tucker, K. Vanderlinde, J. D. Vieira, G. Wang, N. Whitehorn, V. Yefremenko, and O. Zahn. Measurements of Sub-degree B-mode Polarization in the Cosmic Microwave Background from 100 Square Degrees of SPTpol Data. *ArXiv e-prints*, March 2015.
- [69] R. Keisler, C. L. Reichardt, K. A. Aird, B. A. Benson, L. E. Bleem, J. E. Carlstrom, C. L. Chang, H. M. Cho, T. M. Crawford, A. T. Crites, T. de Haan, M. A. Dobbs, J. Dudley, E. M. George, N. W. Halverson, G. P. Holder, W. L. Holzapfel, S. Hoover, Z. Hou, J. D. Hrubes, M. Joy, L. Knox, A. T. Lee, E. M. Leitch, M. Lueker, D. Luong-Van, J. J. McMahon, J. Mehl, S. S. Meyer, M. Millea, J. J. Mohr, T. E. Montroy, T. Natoli, S. Padin, T. Plagge, C. Pryke, J. E. Ruhl, K. K. Schaffer, L. Shaw, E. Shirokoff, H. G. Spieler, Z. Staniszewski, A. A. Stark, K. Story, A. van Engelen, K. Vanderlinde, J. D. Vieira, R. Williamson, and O. Zahn. A Measurement of the Damping Tail of the Cosmic Microwave Background Power Spectrum with the South Pole Telescope. *ApJ*, 743:28, December 2011.

- [70] M. Kesden, A. Cooray, and M. Kamionkowski. Lensing reconstruction with CMB temperature and polarization. *Phys. Rev. D*, 67(12):123507–+, June 2003.
- [71] W. H. Kinney. The energy scale of inflation: is the hunt for the primordial B-mode a waste of time? In S. Hanany and K. A. Olive, editors, *the proceedings of the workshop on “The Cosmic Microwave Background and its Polarization,” New Astronomy Reviews*. Elsevier, 2003. astro-ph/0307005.
- [72] W. H. Kinney, E. W. Kolb, A. Melchiorri, and A. Riotto. Latest inflation model constraints from cosmic microwave background measurements: Addendum. *Phys. Rev. D*, 78(8):087302, October 2008.
- [73] L. Knox. Precision measurement of the mean curvature. *Phys. Rev. D*, 73(2):023503, January 2006.
- [74] L. Knox and M. S. Turner. Detectability of tensor perturbations through anisotropy of the cosmic background radiation. *Physical Review Letters*, 73:3347–3350, December 1994.
- [75] E. Komatsu, J. Dunkley, M. R. Nolta, C. L. Bennett, B. Gold, G. Hinshaw, N. Jarosik, D. Larson, M. Limon, L. Page, D. N. Spergel, M. Halpern, R. S. Hill, A. Kogut, S. S. Meyer, G. S. Tucker, J. L. Weiland, E. Wollack, and E. L. Wright. Five-Year Wilkinson Microwave Anisotropy Probe Observations: Cosmological Interpretation. *ApJS*, 180:330–376, February 2009.
- [76] E. Komatsu, K. M. Smith, J. Dunkley, C. L. Bennett, B. Gold, G. Hinshaw, N. Jarosik, D. Larson, M. R. Nolta, L. Page, D. N. Spergel, M. Halpern, R. S. Hill, A. Kogut, M. Limon, S. S. Meyer, N. Odegard, G. S. Tucker, J. L. Weiland, E. Wollack, and E. L. Wright. Seven-year Wilkinson Microwave Anisotropy Probe (WMAP) Observations: Cosmological Interpretation. *ApJS*, 192:18–+, February 2011.
- [77] D. Larson, J. Dunkley, G. Hinshaw, E. Komatsu, M. R. Nolta, C. L. Bennett, B. Gold, M. Halpern, R. S. Hill, N. Jarosik, A. Kogut, M. Limon, S. S. Meyer, N. Odegard, L. Page, K. M. Smith, D. N. Spergel, G. S. Tucker, J. L. Weiland, E. Wollack, and E. L. Wright. Seven-year Wilkinson Microwave Anisotropy Probe (WMAP) Observations: Power Spectra and WMAP-derived Parameters. *ApJS*, 192:16–+, February 2011.
- [78] J. Lesgourgues and S. Pastor. Massive neutrinos and cosmology. *Phys. Rep.*, 429:307–379, July 2006.
- [79] A. Lewis. Lensed CMB simulation and parameter estimation. *Phys. Rev. D*, 71(8):083008–+, April 2005.
- [80] A. Lewis and S. Bridle. Cosmological parameters from CMB and other data: A Monte Carlo approach. *Phys. Rev. D*, 66(10):103511–+, November 2002.
- [81] A. Lewis and A. Challinor. Weak gravitational lensing of the CMB. *Phys. Rep.*, 429:1–65, June 2006.

- [82] A. Lewis, A. Challinor, and D. Hanson. The shape of the CMB lensing bispectrum. *J. of Cosm. & Astropart. Phys.*, 3:18, March 2011.
- [83] Antony Lewis, Anthony Challinor, and Anthony Lasenby. Efficient computation of CMB anisotropies in closed FRW models. *Astrophys. J.*, 538:473–476, 2000.
- [84] A. R. Liddle and S. M. Leach. How long before the end of inflation were observable perturbations produced? *Phys. Rev. D*, 68(10):103503, November 2003.
- [85] A. D. Linde. A new inflationary universe scenario: A possible solution of the horizon, flatness, homogeneity, isotropy and primordial monopole problems. *Phys. Lett.*, B108:389–393, 1982.
- [86] M. Lueker, C. L. Reichardt, K. K. Schaffer, O. Zahn, P. A. R. Ade, K. A. Aird, B. A. Benson, L. E. Bleem, J. E. Carlstrom, C. L. Chang, H.-M. Cho, T. M. Crawford, A. T. Crites, T. de Haan, M. A. Dobbs, E. M. George, N. R. Hall, N. W. Halverson, G. P. Holder, W. L. Holzapfel, J. D. Hrubes, M. Joy, R. Keisler, L. Knox, A. T. Lee, E. M. Leitch, J. J. McMahon, J. Mehl, S. S. Meyer, J. J. Mohr, T. E. Montroy, S. Padin, T. Plagge, C. Pryke, J. E. Ruhl, L. Shaw, E. Shirokoff, H. G. Spieler, B. Stalder, Z. Staniszewski, A. A. Stark, K. Vanderlinde, J. D. Vieira, and R. Williamson. Measurements of Secondary Cosmic Microwave Background Anisotropies with the South Pole Telescope. *ApJ*, 719:1045–1066, August 2010.
- [87] T. A. Marriage, J. Baptiste Juin, Y.-T. Lin, D. Marsden, M. R. Nolta, B. Partridge, P. A. R. Ade, P. Aguirre, M. Amiri, J. W. Appel, L. F. Barrientos, E. S. Battistelli, J. R. Bond, B. Brown, B. Burger, J. Chervenak, S. Das, M. J. Devlin, S. R. Dicker, W. Bertrand Doriese, J. Dunkley, R. Dünner, T. Essinger-Hileman, R. P. Fisher, J. W. Fowler, A. Hajian, M. Halpern, M. Hasselfield, C. Hernández-Monteagudo, G. C. Hilton, M. Hilton, A. D. Hincks, R. Hlozek, K. M. Huffenberger, D. Handel Hughes, J. P. Hughes, L. Infante, K. D. Irwin, M. Kaul, J. Klein, A. Kosowsky, J. M. Lau, M. Limon, R. H. Lupton, K. Martocci, P. Mauskopf, F. Menanteau, K. Moodley, H. Moseley, C. B. Netterfield, M. D. Niemack, L. A. Page, L. Parker, H. Quintana, B. Reid, N. Sehgal, B. D. Sherwin, J. Sievers, D. N. Spergel, S. T. Staggs, D. S. Swetz, E. R. Switzer, R. Thornton, H. Trac, C. Tucker, R. Warne, G. Wilson, E. Wollack, and Y. Zhao. The Atacama Cosmology Telescope: Extragalactic Sources at 148 GHz in the 2008 Survey. *ApJ*, 731:100–+, April 2011.
- [88] L. M. Mocanu, T. M. Crawford, J. D. Vieira, K. A. Aird, M. Aravena, J. E. Austermann, B. A. Benson, M. Béthermin, L. E. Bleem, M. Bothwell, J. E. Carlstrom, C. L. Chang, S. Chapman, H.-M. Cho, A. T. Crites, T. de Haan, M. A. Dobbs, W. B. Everett, E. M. George, N. W. Halverson, N. Harrington, Y. Hezaveh, G. P. Holder, W. L. Holzapfel, S. Hoover, J. D. Hrubes, R. Keisler, L. Knox, A. T. Lee, E. M. Leitch, M. Lueker, D. Luong-Van, D. P. Marrone, J. J. McMahon, J. Mehl, S. S. Meyer, J. J. Mohr, T. E. Montroy, T. Natoli, S. Padin, T. Plagge, C. Pryke, A. Rest, C. L. Reichardt, J. E. Ruhl, J. T. Sayre, K. K. Schaffer, E. Shirokoff, H. G. Spieler, J. S. Spilker, B. Stalder, Z. Staniszewski, A. A. Stark, K. T. Story, E. R. Switzer,

- K. Vanderlinde, and R. Williamson. Extragalactic Millimeter-wave Point-source Catalog, Number Counts and Statistics from 771 deg² of the SPT-SZ Survey. *ApJ*, 779:61, December 2013.
- [89] V. F. Mukhanov and G. V. Chibisov. Quantum fluctuations and a nonsingular universe. *Soviet Journal of Experimental and Theoretical Physics Letters*, 33:532, May 1981.
- [90] T. Namikawa, D. Hanson, and R. Takahashi. Bias-hardened CMB lensing. *MNRAS*, 431:609–620, May 2013.
- [91] T. Namikawa, D. Yamauchi, and A. Taruya. Full-sky lensing reconstruction of gradient and curl modes from CMB maps. *J. of Cosm. & Astropart. Phys.*, 1:7, January 2012.
- [92] S. J. Osborne, D. Hanson, and O. Doré. Extragalactic foreground contamination in temperature-based CMB lens reconstruction. *J. of Cosm. & Astropart. Phys.*, 3:24, March 2014.
- [93] S. Padin, Z. Staniszewski, R. Keisler, M. Joy, A. A. Stark, P. A. R. Ade, K. A. Aird, B. A. Benson, L. E. Bleem, J. E. Carlstrom, C. L. Chang, T. M. Crawford, A. T. Crites, M. A. Dobbs, N. W. Halverson, S. Heimsath, R. E. Hills, W. L. Holzapfel, C. Lawrie, A. T. Lee, E. M. Leitch, J. Leong, W. Lu, M. Lueker, J. J. McMahon, S. S. Meyer, J. J. Mohr, T. E. Montroy, T. Plagge, C. Pryke, J. E. Ruhl, K. K. Schaffer, E. Shirokoff, H. G. Spieler, and J. D. Vieira. South pole telescope optics. *Appl. Opt.*, 47(24):4418–4428, 2008.
- [94] N. Padmanabhan, X. Xu, D. J. Eisenstein, R. Scalzo, A. J. Cuesta, K. T. Mehta, and E. Kazin. A 2% Distance to $z=0.35$ by Reconstructing Baryon Acoustic Oscillations - I : Methods and Application to the Sloan Digital Sky Survey. *ArXiv e-prints*, January 2012.
- [95] Z. Pan, L. Knox, and M. White. Dependence of the cosmic microwave background lensing power spectrum on the matter density. *MNRAS*, 445:2941–2945, December 2014.
- [96] Planck Collaboration, P. A. R. Ade, N. Aghanim, M. Arnaud, M. Ashdown, J. Aumont, C. Baccigalupi, A. J. Banday, R. B. Barreiro, J. G. Bartlett, and et al. Planck 2015 results. XI. CMB power spectra, likelihood, and consistency of cosmological parameters. *in prep.*, 2015.
- [97] Planck Collaboration, P. A. R. Ade, N. Aghanim, M. Arnaud, M. Ashdown, J. Aumont, C. Baccigalupi, A. J. Banday, R. B. Barreiro, J. G. Bartlett, and et al. Planck 2015 results. XIII. Cosmological parameters. *ArXiv e-prints*, February 2015.
- [98] Planck Collaboration, P. A. R. Ade, N. Aghanim, M. Arnaud, M. Ashdown, J. Aumont, C. Baccigalupi, A. J. Banday, R. B. Barreiro, J. G. Bartlett, and et al. Planck 2015 results. XV. Gravitational lensing. *ArXiv e-prints*, February 2015.
- [99] Planck Collaboration XV. Planck 2013 results. XV. CMB power spectra and likelihood. *A&A*, March 2014.

- [100] Planck Collaboration XVI. Planck 2013 results. XVI. Cosmological parameters. *A&A*, March 2014.
- [101] Planck Collaboration XVII. Planck 2013 results. XVII. Gravitational lensing by large-scale structure. *A&A*, 2013.
- [102] POLARBEAR Collaboration. A Measurement of the Cosmic Microwave Background B-mode Polarization Power Spectrum at Sub-degree Scales with POLARBEAR. *ApJ*, 794:171, October 2014.
- [103] POLARBEAR Collaboration. Evidence for Gravitational Lensing of the Cosmic Microwave Background Polarization from Cross-Correlation with the Cosmic Infrared Background. *Physical Review Letters*, 112(13):131302, April 2014.
- [104] POLARBEAR Collaboration. Measurement of the Cosmic Microwave Background Polarization Lensing Power Spectrum with the POLARBEAR experiment. *Phys.Rev.Lett.*, 113:021301, 2014.
- [105] C. L. Reichardt, P. A. R. Ade, J. J. Bock, J. R. Bond, J. A. Brevik, C. R. Contaldi, M. D. Daub, J. T. Dempsey, J. H. Goldstein, W. L. Holzapfel, C. L. Kuo, A. E. Lange, M. Lueker, M. Newcomb, J. B. Peterson, J. Ruhl, M. C. Runyan, and Z. Staniszewski. High-Resolution CMB Power Spectrum from the Complete ACBAR Data Set. *ApJ*, 694:1200–1219, April 2009.
- [106] C. L. Reichardt, L. Shaw, O. Zahn, K. A. Aird, B. A. Benson, L. E. Bleem, J. E. Carlstrom, C. L. Chang, H. M. Cho, T. M. Crawford, A. T. Crites, T. de Haan, M. A. Dobbs, J. Dudley, E. M. George, N. W. Halverson, G. P. Holder, W. L. Holzapfel, S. Hoover, Z. Hou, J. D. Hrubes, M. Joy, R. Keisler, L. Knox, A. T. Lee, E. M. Leitch, M. Lueker, D. Luong-Van, J. J. McMahon, J. Mehl, S. S. Meyer, M. Millea, J. J. Mohr, T. E. Montroy, T. Natoli, S. Padin, T. Plagge, C. Pryke, J. E. Ruhl, K. K. Schaffer, E. Shirokoff, H. G. Spieler, Z. Staniszewski, A. A. Stark, K. Story, A. van Engelen, K. Vanderlinde, J. D. Vieira, and R. Williamson. A measurement of secondary cosmic microwave background anisotropies with two years of South Pole Telescope observations. *ApJ*, 755:70, November 2012.
- [107] C. L. Reichardt, B. Stalder, L. E. Bleem, T. E. Montroy, K. A. Aird, K. Anderson, R. Armstrong, M. L. N. Ashby, M. Bautz, M. Bayliss, G. Bazin, B. A. Benson, M. Brodwin, J. E. Carlstrom, C. L. Chang, H. M. Cho, A. Clocchiatti, T. M. Crawford, A. T. Crites, T. de Haan, S. Desai, M. A. Dobbs, J. P. Dudley, R. J. Foley, W. R. Forman, E. M. George, M. D. Gladders, A. H. Gonzalez, N. W. Halverson, N. L. Harrington, F. W. High, G. P. Holder, W. L. Holzapfel, S. Hoover, J. D. Hrubes, C. Jones, M. Joy, R. Keisler, L. Knox, A. T. Lee, E. M. Leitch, J. Liu, M. Lueker, D. Luong-Van, A. Mantz, D. P. Marrone, M. McDonald, J. J. McMahon, J. Mehl, S. S. Meyer, L. Mocanu, J. J. Mohr, S. S. Murray, T. Natoli, S. Padin, T. Plagge, C. Pryke, A. Rest, J. Ruel, J. E. Ruhl, B. R. Saliwanchik, A. Saro, J. T. Sayre, K. K. Schaffer, L. Shaw, E. Shirokoff, J. Song, H. G. Spieler, Z. Staniszewski, A. A. Stark, K. Story, C. W. Stubbs, R. Šuhada, A. van Engelen, K. Vanderlinde, J. D. Vieira,

- A. Vikhlinin, R. Williamson, O. Zahn, and A. Zenteno. Galaxy Clusters Discovered via the Sunyaev-Zel'dovich Effect in the First 720 Square Degrees of the South Pole Telescope Survey. *ApJ*, 763:127, February 2013.
- [108] A. G. Riess, L. Macri, S. Casertano, H. Lampeitl, H. C. Ferguson, A. V. Filippenko, S. W. Jha, W. Li, and R. Chornock. A 3% Solution: Determination of the Hubble Constant with the Hubble Space Telescope and Wide Field Camera 3. *ApJ*, 730:119–+, April 2011.
- [109] E. Rozo, R. H. Wechsler, E. S. Rykoff, J. T. Annis, M. R. Becker, A. E. Evrard, J. A. Frieman, S. M. Hansen, J. Hao, D. E. Johnston, B. P. Koester, T. A. McKay, E. S. Sheldon, and D. H. Weinberg. Cosmological Constraints from the Sloan Digital Sky Survey maxBCG Cluster Catalog. *ApJ*, 708:645–660, January 2010.
- [110] A. G. Sánchez, C. G. Scóccola, A. J. Ross, W. Percival, M. Manera, F. Montesano, X. Mazzalay, A. J. Cuesta, D. J. Eisenstein, E. Kazin, C. K. McBride, K. Mehta, A. D. Montero-Dorta, N. Padmanabhan, F. Prada, J. A. Rubiño-Martín, R. Tojeiro, X. Xu, M. V. Magaña, E. Aubourg, N. A. Bahcall, S. Bailey, D. Bizyaev, A. S. Bolton, H. Brewington, J. Brinkmann, J. R. Brownstein, J. R. Gott, J. C. Hamilton, S. Ho, K. Honscheid, A. Labatie, E. Malanushenko, V. Malanushenko, C. Maraston, D. Muna, R. C. Nichol, D. Oravetz, K. Pan, N. P. Ross, N. A. Roe, B. A. Reid, D. J. Schlegel, A. Shelden, D. P. Schneider, A. Simmons, R. Skibba, S. Snedden, D. Thomas, J. Tinker, D. A. Wake, B. A. Weaver, D. H. Weinberg, M. White, I. Zehavi, and G. Zhao. The clustering of galaxies in the SDSS-III Baryon Oscillation Spectroscopic Survey: cosmological implications of the large-scale two-point correlation function. *MNRAS*, 425:415–437, September 2012.
- [111] K. K. Schaffer, T. M. Crawford, K. A. Aird, B. A. Benson, L. E. Bleem, J. E. Carlstrom, C. L. Chang, H. M. Cho, A. T. Crites, T. de Haan, M. A. Dobbs, E. M. George, N. W. Halverson, G. P. Holder, W. L. Holzapfel, S. Hoover, J. D. Hrubes, M. Joy, R. Keisler, L. Knox, A. T. Lee, E. M. Leitch, M. Lueker, D. Luong-Van, J. J. McMahon, J. Mehl, S. S. Meyer, J. J. Mohr, T. E. Montroy, S. Padin, T. Plagge, C. Pryke, C. L. Reichardt, J. E. Ruhl, E. Shirokoff, H. G. Spieler, B. Stalder, Z. Staniszewski, A. A. Stark, K. Story, K. Vanderlinde, J. D. Vieira, and R. Williamson. The First Public Release of South Pole Telescope Data: Maps of a 95 deg² Field from 2008 Observations. *ApJ*, 743:90, December 2011.
- [112] D. J. Schlegel, D. P. Finkbeiner, and M. Davis. Maps of Dust Infrared Emission for Use in Estimation of Reddening and Cosmic Microwave Background Radiation Foregrounds. *ApJ*, 500:525–+, June 1998.
- [113] U. Seljak. Gravitational Lensing Effect on Cosmic Microwave Background Anisotropies: A Power Spectrum Approach. *ApJ*, 463:1–+, May 1996.
- [114] U. Seljak and M. Zaldarriaga. Signature of Gravity Waves in the Polarization of the Microwave Background. *Physical Review Letters*, 78:2054–2057, March 1997.

- [115] U. Seljak and M. Zaldarriaga. Measuring Dark Matter Power Spectrum from Cosmic Microwave Background. *Physical Review Letters*, 82:2636–2639, March 1999.
- [116] L. D. Shaw, D. Nagai, S. Bhattacharya, and E. T. Lau. Impact of Cluster Physics on the Sunyaev-Zel’dovich Power Spectrum. *ApJ*, 725:1452–1465, December 2010.
- [117] B. D. Sherwin, S. Das, A. Hajian, G. Addison, J. R. Bond, D. Crichton, M. J. Devlin, J. Dunkley, M. B. Gralla, M. Halpern, J. C. Hill, A. D. Hincks, J. P. Hughes, K. Huffenberger, R. Hlozek, A. Kosowsky, T. Louis, T. A. Marriage, D. Marsden, F. Menanteau, K. Moodley, M. D. Niemack, L. A. Page, E. D. Reese, N. Sehgal, J. Sievers, C. Sifón, D. N. Spergel, S. T. Staggs, E. R. Switzer, and E. Wollack. The Atacama Cosmology Telescope: Cross-correlation of cosmic microwave background lensing and quasars. *Phys. Rev. D*, 86(8):083006, October 2012.
- [118] B. D. Sherwin, J. Dunkley, S. Das, J. W. Appel, J. R. Bond, C. Sofia Carvalho, M. J. Devlin, R. Dunner, T. Essinger-Hileman, J. W. Fowler, A. Hajian, M. Halpern, M. Hasselfield, A. D. Hincks, R. Hlozek, J. P. Hughes, K. D. Irwin, J. Klein, A. Kosowsky, T. A. Marriage, D. Marsden, K. Moodley, F. Menanteau, M. D. Niemack, M. R. Nolta, L. A. Page, L. Parker, E. D. Reese, B. L. Schmitt, N. Sehgal, J. Sievers, D. N. Spergel, S. T. Staggs, D. S. Swetz, E. R. Switzer, R. Thornton, K. Visnjic, and E. Wollack. The Atacama Cosmology Telescope: Evidence for Dark Energy from the CMB Alone. *ArXiv e-prints*, May 2011.
- [119] E. Shirokoff, C. L. Reichardt, L. Shaw, M. Millea, P. A. R. Ade, K. A. Aird, B. A. Benson, L. E. Bleem, J. E. Carlstrom, C. L. Chang, H. M. Cho, T. M. Crawford, A. T. Crites, T. de Haan, M. A. Dobbs, J. Dudley, E. M. George, N. W. Halverson, G. P. Holder, W. L. Holzapfel, J. D. Hrubes, M. Joy, R. Keisler, L. Knox, A. T. Lee, E. M. Leitch, M. Lueker, D. Luong-Van, J. J. McMahon, J. Mehl, S. S. Meyer, J. J. Mohr, T. E. Montroy, S. Padin, T. Plagge, C. Pryke, J. E. Ruhl, K. K. Schaffer, H. G. Spieler, Z. Staniszewski, A. A. Stark, K. Story, K. Vanderlinde, J. D. Vieira, R. Williamson, and O. Zahn. Improved Constraints on Cosmic Microwave Background Secondary Anisotropies from the Complete 2008 South Pole Telescope Data. *ApJ*, 736:61–+, July 2011.
- [120] J. Silk. Cosmic black-body radiation and galaxy formation. *ApJ*, 151:459, 1968.
- [121] K. M. Smith, O. Zahn, and O. Doré. Detection of gravitational lensing in the cosmic microwave background. *Phys. Rev. D*, 76(4):043510–+, August 2007.
- [122] G. F. Smoot et al. Structure in the COBE Differential Microwave Radiometer First-Year Maps. *ApJ*, 396:L1–L5, 1992.
- [123] John P. Snyder. *Map projections—a working manual*. U.S. Geological Survey, Washington, 1987.
- [124] Z. Staniszewski, P. A. R. Ade, K. A. Aird, B. A. Benson, L. E. Bleem, J. E. Carlstrom, C. L. Chang, H.-M. Cho, T. M. Crawford, A. T. Crites, T. de Haan, M. A. Dobbs, N. W. Halverson, G. P. Holder, W. L. Holzapfel, J. D. Hrubes, M. Joy, R. Keisler, T. M.

- Lanting, A. T. Lee, E. M. Leitch, A. Loehr, M. Lueker, J. J. McMahon, J. Mehl, S. S. Meyer, J. J. Mohr, T. E. Montroy, C.-C. Ngeow, S. Padin, T. Plagge, C. Pryke, C. L. Reichardt, J. E. Ruhl, K. K. Schaffer, L. Shaw, E. Shirokoff, H. G. Spieler, B. Stalder, A. A. Stark, K. Vanderlinde, J. D. Vieira, O. Zahn, and A. Zenteno. Galaxy Clusters Discovered with a Sunyaev-Zel'dovich Effect Survey. *ApJ*, 701:32–41, August 2009.
- [125] A. A. Starobinsky. Dynamics of phase transition in the new inflationary universe scenario and generation of perturbations. *Phys. Lett.*, B117:175–178, 1982.
- [126] K. Story, K. A. Aird, K. Andersson, R. Armstrong, G. Bazin, B. A. Benson, L. E. Bleem, M. Bonamente, M. Brodwin, J. E. Carlstrom, C. L. Chang, A. Clocchiatti, T. M. Crawford, A. T. Crites, T. de Haan, S. Desai, M. A. Dobbs, J. P. Dudley, R. J. Foley, E. M. George, M. D. Gladders, A. H. Gonzalez, N. W. Halverson, F. W. High, G. P. Holder, W. L. Holzapfel, S. Hoover, J. D. Hrubes, M. Joy, R. Keisler, L. Knox, A. T. Lee, E. M. Leitch, M. Lueker, D. Luong-Van, D. P. Marrone, J. J. McMahon, J. Mehl, S. S. Meyer, J. J. Mohr, T. E. Montroy, S. Padin, T. Plagge, C. Pryke, C. L. Reichardt, A. Rest, J. Ruel, J. E. Ruhl, B. R. Saliwanchik, A. Saro, K. K. Schaffer, L. Shaw, E. Shirokoff, J. Song, H. G. Spieler, B. Stalder, Z. Staniszewski, A. A. Stark, C. W. Stubbs, K. Vanderlinde, J. D. Vieira, R. Williamson, and A. Zenteno. South Pole Telescope Detections of the Previously Unconfirmed Planck Early Sunyaev-Zel'dovich Clusters in the Southern Hemisphere. *ApJ Lett.*, 735:L36+, July 2011.
- [127] K. Story, E. Leitch, P. Ade, K. A. Aird, J. E. Austermann, J. A. Beall, D. Becker, A. N. Bender, B. A. Benson, L. E. Bleem, J. Britton, J. E. Carlstrom, C. L. Chang, H. C. Chiang, H.-M. Cho, T. M. Crawford, A. T. Crites, A. Datsman, T. de Haan, M. A. Dobbs, W. Everett, A. Ewall-Wice, E. M. George, N. W. Halverson, N. Harrington, J. W. Henning, G. C. Hilton, W. L. Holzapfel, S. Hoover, N. Huang, J. Hubmayr, K. D. Irwin, M. Karfinkle, R. Keisler, J. Kennedy, A. T. Lee, D. Li, M. Lueker, D. P. Marrone, J. J. McMahon, J. Mehl, S. S. Meyer, J. Montgomery, T. E. Montroy, J. Nagy, T. Natoli, J. P. Nibarger, M. D. Niemack, V. Novosad, S. Padin, C. Pryke, C. L. Reichardt, J. E. Ruhl, B. R. Saliwanchik, J. T. Sayre, K. K. Schaffer, E. Shirokoff, G. Smecher, B. Stalder, C. Tucker, K. Vanderlinde, J. D. Vieira, G. Wang, R. Williamson, V. Yefremenko, K. W. Yoon, and E. Young. South Pole Telescope software systems: control, monitoring, and data acquisition. In *Society of Photo-Optical Instrumentation Engineers (SPIE) Conference Series*, volume 8451 of *Society of Photo-Optical Instrumentation Engineers (SPIE) Conference Series*, September 2012.
- [128] K. T. Story, D. Hanson, P. A. R. Ade, K. A. Aird, J. E. Austermann, J. A. Beall, A. N. Bender, B. A. Benson, L. E. Bleem, J. E. Carlstrom, C. L. Chang, H. C. Chiang, H. Cho, R. Citron, T. M. Crawford, A. T. Crites, T. de Haan, M. A. Dobbs, W. Everett, J. Gallicchio, J. Gao, E. M. George, A. Gilbert, N. W. Halverson, N. Harrington, J. W. Henning, G. C. Hilton, G. P. Holder, W. L. Holzapfel, S. Hoover, Z. Hou, J. D. Hrubes, N. Huang, J. Hubmayr, K. D. Irwin, R. Keisler, L. Knox, A. T. Lee, E. M. Leitch, D. Li, C. Liang, D. Luong-Van, J. J. McMahon, J. Mehl, S. S. Meyer, L. Mocanu, T. E. Montroy, T. Natoli, J. P. Nibarger, V. Novosad, S. Padin, C. Pryke, C. L. Reichardt, J. E. Ruhl, B. R. Saliwanchik, J. T. Sayre, K. K. Schaffer, G. Smecher, A. A. Stark,

- C. Tucker, K. Vanderlinde, J. D. Vieira, G. Wang, N. Whitehorn, V. Yefremenko, and O. Zahn. A Measurement of the Cosmic Microwave Background Gravitational Lensing Potential from 100 Square Degrees of SPTpol Data. *ArXiv e-prints*, December 2014.
- [129] K. T. Story, C. L. Reichardt, Z. Hou, R. Keisler, K. A. Aird, B. A. Benson, L. E. Bleem, J. E. Carlstrom, C. L. Chang, H.-M. Cho, T. M. Crawford, A. T. Crites, T. de Haan, M. A. Dobbs, J. Dudley, B. Follin, E. M. George, N. W. Halverson, G. P. Holder, W. L. Holzapfel, S. Hoover, J. D. Hrubes, M. Joy, L. Knox, A. T. Lee, E. M. Leitch, M. Lueker, D. Luong-Van, J. J. McMahon, J. Mehl, S. S. Meyer, M. Millea, J. J. Mohr, T. E. Montroy, S. Padin, T. Plagge, C. Pryke, J. E. Ruhl, J. T. Sayre, K. K. Schaffer, L. Shaw, E. Shirokoff, H. G. Spieler, Z. Staniszewski, A. A. Stark, A. van Engelen, K. Vanderlinde, J. D. Vieira, R. Williamson, and O. Zahn. A Measurement of the Cosmic Microwave Background Damping Tail from the 2500-Square-Degree SPT-SZ Survey. *ApJ*, 779:86, December 2013.
- [130] A. van Engelen, S. Bhattacharya, N. Sehgal, G. P. Holder, O. Zahn, and D. Nagai. CMB Lensing Power Spectrum Biases from Galaxies and Clusters Using High-angular Resolution Temperature Maps. *ApJ*, 786:13, May 2014.
- [131] A. van Engelen, R. Keisler, O. Zahn, K. A. Aird, B. A. Benson, L. E. Bleem, J. E. Carlstrom, C. L. Chang, H. M. Cho, T. M. Crawford, A. T. Crites, T. de Haan, M. A. Dobbs, J. Dudley, E. M. George, N. W. Halverson, G. P. Holder, W. L. Holzapfel, S. Hoover, Z. Hou, J. D. Hrubes, M. Joy, L. Knox, A. T. Lee, E. M. Leitch, M. Lueker, D. Luong-Van, J. J. McMahon, J. Mehl, S. S. Meyer, M. Millea, J. J. Mohr, T. E. Montroy, T. Natoli, S. Padin, T. Plagge, C. Pryke, C. L. Reichardt, J. E. Ruhl, J. T. Sayre, K. K. Schaffer, L. Shaw, E. Shirokoff, H. G. Spieler, Z. Staniszewski, A. A. Stark, K. Story, K. Vanderlinde, J. D. Vieira, and R. Williamson. A Measurement of Gravitational Lensing of the Microwave Background Using South Pole Telescope Data. *ApJ*, 756:142, September 2012.
- [132] A. van Engelen, B. D. Sherwin, N. Sehgal, G. E. Addison, R. Allison, N. Battaglia, F. de Bernardis, E. Calabrese, K. Coughlin, D. Crichton, J. R. Bond, R. Datta, R. Dunner, J. Dunkley, E. Grace, M. Gralla, A. Hajian, M. Hasselfield, S. Henderson, J. C. Hill, M. Hilton, A. D. Hincks, R. Hlozek, K. M. Huffenberger, J. P. Hughes, B. Koopman, A. Kosowsky, T. Louis, M. Lungu, M. Madhavacheril, L. Maurin, J. McMahon, K. Moodley, C. Munson, S. Naess, F. Nati, L. Newburgh, M. D. Niemack, M. Nolta, L. A. Page, B. Partridge, C. Pappas, B. L. Schmitt, J. L. Sievers, S. Simon, D. N. Spergel, S. T. Staggs, E. R. Switzer, J. T. Ward, and E. J. Wollack. The Atacama Cosmology Telescope: Lensing of CMB Temperature and Polarization Derived from Cosmic Infrared Background Cross-Correlation. *ArXiv e-prints*, December 2014.
- [133] K. Vanderlinde, T. M. Crawford, T. de Haan, J. P. Dudley, L. Shaw, P. A. R. Ade, K. A. Aird, B. A. Benson, L. E. Bleem, M. Brodwin, J. E. Carlstrom, C. L. Chang, A. T. Crites, S. Desai, M. A. Dobbs, R. J. Foley, E. M. George, M. D. Gladders, N. R. Hall, N. W. Halverson, F. W. High, G. P. Holder, W. L. Holzapfel, J. D. Hrubes, M. Joy, R. Keisler, L. Knox, A. T. Lee, E. M. Leitch, A. Loehr, M. Lueker, D. P.

- Marrone, J. J. McMahon, J. Mehl, S. S. Meyer, J. J. Mohr, T. E. Montroy, C.-C. Ngeow, S. Padin, T. Plagge, C. Pryke, C. L. Reichardt, A. Rest, J. Ruel, J. E. Ruhl, K. K. Schaffer, E. Shirokoff, J. Song, H. G. Spieler, B. Stalder, Z. Staniszewski, A. A. Stark, C. W. Stubbs, A. van Engelen, J. D. Vieira, R. Williamson, Y. Yang, O. Zahn, and A. Zenteno. Galaxy Clusters Selected with the Sunyaev-Zel'dovich Effect from 2008 South Pole Telescope Observations. *ApJ*, 722:1180–1196, October 2010.
- [134] J. D. Vieira, T. M. Crawford, E. R. Switzer, P. A. R. Ade, K. A. Aird, M. L. N. Ashby, B. A. Benson, L. E. Bleem, M. Brodwin, J. E. Carlstrom, C. L. Chang, H.-M. Cho, A. T. Crites, T. de Haan, M. A. Dobbs, W. Everett, E. M. George, M. Gladders, N. R. Hall, N. W. Halverson, F. W. High, G. P. Holder, W. L. Holzapfel, J. D. Hrubes, M. Joy, R. Keisler, L. Knox, A. T. Lee, E. M. Leitch, M. Lueker, D. P. Marrone, V. McIntyre, J. J. McMahon, J. Mehl, S. S. Meyer, J. J. Mohr, T. E. Montroy, S. Padin, T. Plagge, C. Pryke, C. L. Reichardt, J. E. Ruhl, K. K. Schaffer, L. Shaw, E. Shirokoff, H. G. Spieler, B. Stalder, Z. Staniszewski, A. A. Stark, K. Vanderlinde, W. Walsh, R. Williamson, Y. Yang, O. Zahn, and A. Zenteno. Extragalactic Millimeter-wave Sources in South Pole Telescope Survey Data: Source Counts, Catalog, and Statistics for an 87 Square-degree Field. *ApJ*, 719:763–783, August 2010.
- [135] A. Vikhlinin, A. V. Kravtsov, R. A. Burenin, H. Ebeling, W. R. Forman, A. Hornstrup, C. Jones, S. S. Murray, D. Nagai, H. Quintana, and A. Voevodkin. Chandra Cluster Cosmology Project III: Cosmological Parameter Constraints. *ApJ*, 692:1060–1074, February 2009.
- [136] S.D.M. White, J.F. Navarro, A.E. Evrard, and C.S. Frenk. The baryon content of galaxy clusters: A challenge to cosmological orthodoxy. *Nature*, 366:429, 1993.
- [137] R. Williamson, B. A. Benson, F. W. High, K. Vanderlinde, P. A. R. Ade, K. A. Aird, K. Andersson, R. Armstrong, M. L. N. Ashby, M. Bautz, G. Bazin, E. Bertin, L. E. Bleem, M. Bonamente, M. Brodwin, J. E. Carlstrom, C. L. Chang, S. C. Chapman, A. Clocchiatti, T. M. Crawford, A. T. Crites, T. de Haan, S. Desai, M. A. Dobbs, J. P. Dudley, G. G. Fazio, R. J. Foley, W. R. Forman, G. Garmire, E. M. George, M. D. Gladders, A. H. Gonzalez, N. W. Halverson, G. P. Holder, W. L. Holzapfel, S. Hoover, J. D. Hrubes, C. Jones, M. Joy, R. Keisler, L. Knox, A. T. Lee, E. M. Leitch, M. Lueker, D. Luong-Van, D. P. Marrone, J. J. McMahon, J. Mehl, S. S. Meyer, J. J. Mohr, T. E. Montroy, S. S. Murray, S. Padin, T. Plagge, C. Pryke, C. L. Reichardt, A. Rest, J. Ruel, J. E. Ruhl, B. R. Saliwanchik, A. Saro, K. K. Schaffer, L. Shaw, E. Shirokoff, J. Song, H. G. Spieler, B. Stalder, S. A. Stanford, Z. Staniszewski, A. A. Stark, K. Story, C. W. Stubbs, J. D. Vieira, A. Vikhlinin, and A. Zenteno. A Sunyaev-Zel'dovich-selected Sample of the Most Massive Galaxy Clusters in the 2500 deg² South Pole Telescope Survey. *ApJ*, 738:139–+, September 2011.
- [138] O. Zahn, C. L. Reichardt, L. Shaw, A. Lidz, K. A. Aird, B. A. Benson, L. E. Bleem, J. E. Carlstrom, C. L. Chang, H. M. Cho, T. M. Crawford, A. T. Crites, T. de Haan, M. A. Dobbs, O. Doré, J. Dudley, E. M. George, N. W. Halverson, G. P. Holder,

- W. L. Holzapfel, S. Hoover, Z. Hou, J. D. Hrubes, M. Joy, R. Keisler, L. Knox, A. T. Lee, E. M. Leitch, M. Lueker, D. Luong-Van, J. J. McMahon, J. Mehl, S. S. Meyer, M. Millea, J. J. Mohr, T. E. Montroy, T. Natoli, S. Padin, T. Plagge, C. Pryke, J. E. Ruhl, K. K. Schaffer, E. Shirokoff, H. G. Spieler, Z. Staniszewski, A. A. Stark, K. Story, A. van Engelen, K. Vanderlinde, J. D. Vieira, and R. Williamson. Cosmic Microwave Background Constraints on the Duration and Timing of Reionization from the South Pole Telescope. *ApJ*, 756:65, September 2012.
- [139] M. ;. Zaldarriaga and D. D. Harari. Analytic approach to the polarization of the cosmic microwave background in flat and open universes. *Phys. Rev. D*, 52:3276–3287, September 1995.
- [140] M. Zaldarriaga and U. Seljak. Gravitational lensing effect on cosmic microwave background polarization. *Phys. Rev. D*, 58:23003 (6 pages), July 1998.
- [141] M. Zaldarriaga, D. N. Spergel, and U. Seljak. Microwave Background Constraints on Cosmological Parameters. *ApJ*, 488:1+, October 1997.